Newcastle University
Faculty of Science, Agriculture and Engineering
School of Engineering

Spaceborne InSAR for Dam Stability

Yasir Al-Husseinawi

Thesis submitted for the degree of
Doctor of Philosophy

April 2019

Abstract

This study evaluates the feasibility of the use of satellite radar for dam deformation monitoring. Spaceborne Interferometric Synthetic Aperture Radar (InSAR) has long been used to monitor geohazards, including earthquakes, landslides, and volcanos. However, few studies have recently investigated its feasibility for localised deformation monitoring such as of earth dams. Here two case studies are presented of the monitoring of dams in Iraq.

Mosul dam is one of the most dangerous dams in the world. Previous studies have reported that over a million human lives would be potentially at risk should dam failure occur. Therefore, investigation of its health using precise and continuous observations is crucial. This was achieved with two independent geodetic datasets from levelling and InSAR, and the results show continuous vertical displacements on the dam crest due to the dissolution of foundations. Vertical displacement rate estimates from levelling and InSAR for the period 2003-2010 are in good agreement, with a correlation of 0.93 and an RMSE of ± 1.7 mm. For the period 2014-2017, the correlation is 0.95 and the RMSE is ± 0.9 mm. The movement of the dam was evaluated using settlement index which is not referring to critical instability of the dam. However, the spatial and temporal displacement anomalies emphasize that a careful monitoring and remedial work should continue. The continuous displacement in the dam foundation could loosen the compaction of the embankment and result in internal erosion.

In a separate study, Darbandikhan dam was monitored using a global positioning system (GPS), levelling, and Sentinel-1 data to evaluate its stability after the 2017 Mw 7.3 Sarpol-e Zahab earthquake. The large gradient of the dam's displacements on its crest hindered the estimation of co-seismic displacements using medium-resolution SAR data. However, Sentinel-1 images were sufficient to examine the dam's stability before and after the earthquake. The results show that the dam was stable between October 2014 and November 2017, but after the earthquake continuous subsidence on the dam crest occurred between November 2017 and March 2018.

For the first time the stability of the Mosul and Darbandikhan dams has been assessed using an integration of InSAR and in-situ observations. Different types of deformations were recognized, which helped in interpreting the dam's deformation mechanisms.

DECLARATION

I confirm that this is my own work and the use of all material from other sources has

been properly and fully acknowledged.

Yasir Al-Husseinawi

The text of Section 3.2 and Chapter 5 is, in part, a reformatted version of material appearing in: Al-Husseinawi, Y., Li, Z., Clarke, P. and Edwards, S. (2018) 'Evaluation of the Stability of the Darbandikhan Dam after the 12 November 2017 Mw 7.3 Sarpol-e Zahab (Iran–Iraq Border) Earthquake', *Remote Sensing*, 10(9), 1426, doi: 10.3390/rs10091426. The dissertation author was the primary researcher and author, whilst the co-authors listed in this publication directed and supervised the research which forms the basis for these sections (Copyright by MDPI - Remote Sensing).

CIRTIFICATE OF APPROVAL

I confirm that, to the best of my knowledge, this thesis is from the student's own work and efforts, and all other sources of information used have been acknowledged. This thesis has been submitted with my approval for the PhD degree.

Professor Zhenhong Li

Professor Peter Clarke

Dr Stuart Edwards

Acknowledgment

Firstly, I would like to express my sincere gratitude to my supervisors, Professor Zhenhong Li, Professor Peter Clarke and Dr Stuart Edwards, for their continuous support of my PhD and their patience and recommendations to keep my research on track. They have provided me with extensive personal and professional guidance and taught me a great deal about both scientific research and life in general. Also, I am very much thankful to Professor Roberto Tomás for his recommendations and kind support at various stages of my PhD.

This research would not have been possible without the support from my sponsor, the Ministry of Higher Education (MOHE) and the State Commission of Surveys (SCOS) in Iraq in terms of financial assistance and providing data.

I would also like to thank Dr Ciprian Spatar, Dr Paola Crippa, Dr Elias Berra, Dr Maria Peppa, Dr Magda Smigaj and Mr Martin Robertson for sharing their experience and for support during my study.

In addition, I would like to thank my colleagues for support, advice and discussion: Keren Dai, Chen Yu, Julia Stockamp, Zheng Wang, Jiajun Chen, Polpreecha Chidburee, Miles Clement, Ahmed Elsherif, Ben Grayson, Marine Roger, Lesley Davidson, Surassawadee Phoompanich, Lyndsey Graham, Katarina Vardic and Grant Tregonning.

Last but not least, I would like to thank my family: my parents and my wife, my brothers and sister, for supporting me spiritually throughout the writing and for their support in difficult times. Also, I would like to thank my three wonderful children, Ammar, Ahmed and Sajad, who provide unending inspiration.

Table of Contents

List of Tables

List of Figures

List of Abbreviations

ALOS	Advanced Land Observing Satellite
AoI	Area of Interest
APS	Atmospheric Phase Screen
ASAR	Advanced Synthetic Aperture Radar
BM	Benchmark
BW	Bandwidth
CPT	Coherent Pixel Technique
CSK	COSMO-SkyMed
DEM	Digital Elevation Model
DInSAR	Differential Interferometric Synthetic Aperture Radar
DNS	Downstream
DORIS	Doppler Orbitography and Radio-positioning Integrated by Satellite
DS	Distributed Scatterers
ECMWF	European Centre for Medium-Range Weather Forecasts
ERS	European Remote Sensing
FM	Frequency Modulation
GACOS	Generic Atmospheric Correction Online Service
GBSAR	Ground Based SAR
GEOSAR	Geosynchronous Earth Orbit Synthetic Aperture Radar
GNSS	Global Navigation Satellite System
GPS	Global Positioning System
HST	Hydrostatic Seasonal Time
HTT	Hydrostatic Temperature Time
ICOLD	International Commission on Large Dams
ITRF	International Terrestrial Reference Frame
IWS	Interferometric Wide Swath
LOS	Line-of-Sight
LUT	Look Up Table
MCF	Minimum Cost Flow
MDG	Maximum Detectable Gradient
MMI	Modified Mercalli Intensity
MOWR	Ministry of Water Resources
NASA	National Aeronautics and Space Admission
PRF	Pulse Repetition Frequency
PSI	Permanent Scatterers Interferometry
RAR	Real Aperture Radar
RDC	Range-Doppler Coordinates
RMSE	Root mean square error
RSC	Radar Cross Section
SAR	Synthetic Aperture Radar
SBAS	Small BAseline Subset
SCS	State Commission of Surveying

S_I	Settlement Index
SLC	Single Look Complex
SNR	Signal-to-Noise Ratio
SP	Spotlight
SRTM	Shuttle Radar Topography Mission
ST	StripMap
SVD	Singular Value Decomposition
TLV	Temporary Linear Velocity
TOPS	Terrain Observation with Progressive Scans
TS+AEM	Time Series + Atmospheric Estimation Model
TSX	TerraSAR-X
UPS	Upstream
USGS	U.S. Geological Survey
UTC	Coordinated Universal Time

Chapter 1. Introduction

1.1 Preamble

Water dams are important elements of a country's infrastructure, which is used to provide water for irrigation, domestic use, the manufacturing sector, power generation, and flood protection. However, dam failures can be catastrophic, resulting in loss of life and damage to property. Therefore, periodic investigation and monitoring during and after construction is crucial. Conventional monitoring approaches are becoming less widely used since they require intensive computational and field work in addition to the high cost and time consumed in carrying out the investigation (Biedermann 1997). This leads to less frequent monitoring of dams during their operational lives. The success achieved by utilizing imaging radar in monitoring large-scale geophysical deformations such as volcanos, earthquakes, mining systems, and landslides has motivated research into the use of imaging radar for infrastructure deformation monitoring. This thesis investigates the feasibility of using Interferometric Synthetic Aperture Radar (InSAR) for the monitoring of embankment dams, and the stability of two embankment dams in Iraq (Mosul and Darbandikhan) is evaluated.

The Mosul dam is the largest dam in Iraq and has been classified as one of the most dangerous dams in the world (Al-Ansari *et al.*, 2015). It was built over gypsum rocks that are soluble at high water pressure. Since the dam was built in the 1980s, its foundations have been grouted to fill the voids that may occur because of rock dissolution. However, the grouting work was paused after August 2014 due to political conflicts at the dam site. This led to a serious concern about the dam safety. Annunziato *et al.* (2016) showed that about six million people would be affected by the collapse of the dam and more than one million of these would be at risk of flooding under 2 m of water. In this thesis, multi-temporal Synthetic Aperture Radar (SAR) datasets and levelling data are used to evaluate the stability of the dam between 2003 and 2017.

The second case study in this thesis concerns the Darbandikhan dam. This is also an embankment dam (rockfill) that was built in the 1950s in the north-east of Iraq. This dam was badly damaged by the large Sarpol-e Zahab earthquake which occurred in November 2017. Global Positioning System (GPS), levelling and Sentinel-1A/B data are integrated to estimate the dam's movement before and after the earthquake. The location of the Mosul and Darbandikhan dams are shown in Figure 1.1.

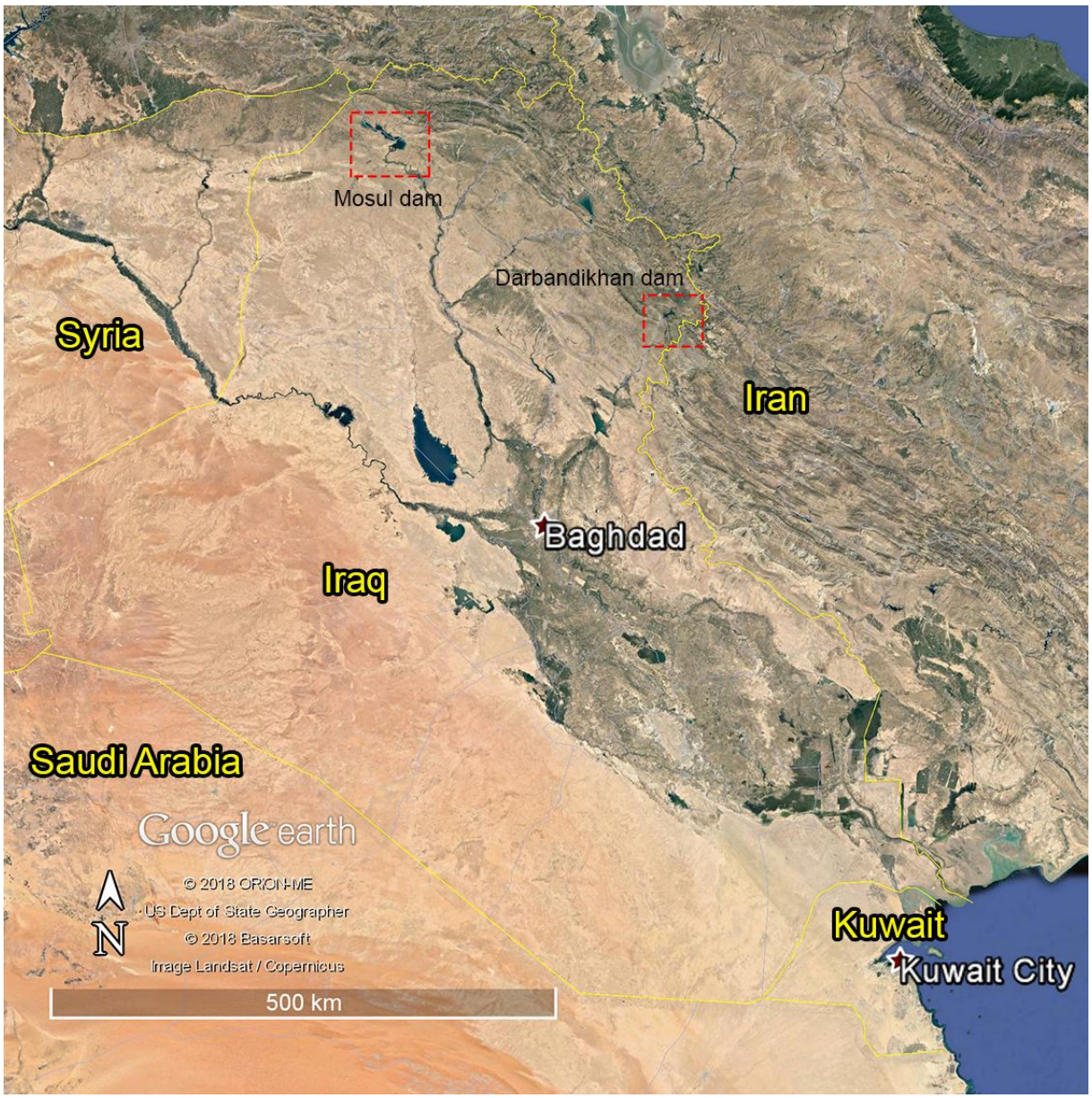

Figure 1.1. Study areas. Note that the Mosul and Darbandikhan dam sites are indicated with dashed red boxes.

1.2 Embankment dams

Dams can be classified into four types (US Army Corps of Engineers, 2002): 1) arc dams have a concrete arc structure facing toward the water to increase the resistance force; 2) buttress dams are also concrete or masonry dams with supporting triangular walls built on the downstream side to prevent the dam from being moved by the hydraulic pressure; 3) gravity dams are also made from concrete, but gravity is the main force that keeps the dam stable; and 4) embankment dams are constructed from natural materials which mainly include compacted soil (earthfill) and/or rocks (rockfill). The last one is the most common type (Johnston *et al.*, 1990; U.S. Department of the Interior, 2012). In this section, only embankment dams are described since both of the dams studied in this thesis are of this type. The design specifications

and materials used in the construction of these types are presented below. The brief introduction of the design and specification of each dam is crucial to understand the mechanisms of deformation of their embankments.

1.2.1 Earthfill dams

Depending on the design and construction material used, earthfill dams are divided into three types (U.S. Department of the Interior, 2012):

- **Diaphragm dam**: This is constructed from sand, gravel or rocks with impermeable material placed on the upstream slope or in the centre of the dam (diaphragm) to prevent water from penetrating the dam body. The diaphragm is constructed from asphaltic, reinforced concrete, metal or compacted earthfill.

- **Homogeneous embankment**: A homogeneous dam is composed of one type of impermeable material. The upstream and downstream slopes must be smooth to avoid sloughing when the reservoir is rapidly drawn down. This type of dam has witnessed improvements to prevent water seepage in the downstream slope when the water level is maintained for a long time. A permeable material is placed within the dam section to control the seepage. This material works as a drainage feature allowing for water seepage without causing internal erosion.

- **Zoned earthfill:** This type of dam is the most common compared to other earthfill types (U.S. Department of the Interior, 2012). It is composed of an impermeable central core protected by transition zones in the upstream slope, and drains and filters in the downstream slope (Hunter and Fell, 2003). Additionally, an external strong surface, or shell can be placed between the slope and the core (U.S. Department of the Interior, 2012). The shell consists of gravel, rocks, cobbles or random fill. This type of earthfill takes advantage of different materials placed in various zones to take the benefits of the properties of different materials. The transition zones protect the core from cracking and from erosion when a rapid drawdown is needed. Filters prevent sediments washing out from the central core and the penetration of water through any potential crack or pipe. The central zone consists of silts, sandy silts, clays, sandy clays, gravel clays or combinations of these materials. In seismic regions, the design of the filters and drains must take into consideration the potential occurrence of cracks, and thus their thickness should be appropriate. The Mosul dam which is studied in this thesis is of this type.

1.2.2 Rockfill dams

A rockfill dam is preferable when the dam is constructed in a mountainous region where a sufficient amount of rocks is available. This type can overcome various construction problems such as difficulties in obtaining concrete, construction during wet weather or when the dam is expected to be removed in the future. Further advantageous factors include ability to conduct grouting even during construction, and resistance to seepage and uplift pressure. Rockfill dams are mainly constructed from rocks and an impermeable membrane while the foundations are constructed from earth, reinforced concrete or asphaltic concrete. There are three types of rockfill dams: central core, sloping core and upstream membrane. The first two types are collectively called internal membrane dams and they have advantages over the upstream membrane type because they are protected from external damage and weathering, a short grouting curtain, which is rows of holes used for grouting, is required, and the core can be grouted from the crest. Also, this type is preferable in poor foundation conditions, and extensive experience is not needed as with the upstream membrane type. In contrast, the upstream membrane dam is protected by an impermeable layer of concrete, steel or asphalt on the upstream slope. The advantages of this type include easier inspection and remedial works, the membrane can be constructed during or after dam construction, and the foundation can be grouted from the surface without affecting critical zones in the core. Also, large portions of the dam will be protected against water seepage, and the downstream slope can remain protected and inaccessible to water (U.S. Department of the Interior, 2012). The Darbandikhan dam, which is studied in Chapter 5 of this thesis, is a central core rockfill dam.

This thesis focusses on embankment dams since it is the most common dam type (Gutiérrez *et al.*, 2003; British Dam Society, 2017). Dams are subject to internal and/or external types of deformation which are principally caused by environmental problems, construction faults, the geological setting or fluctuation in the water contained in the reservoir. Serious problems in the foundations or the main body of the dam can develop rapidly, posing potential hazards to downstream residential areas in terms of mortality risks and property loss and damage (US Army Corps of Engineers, 2002). Thus, the choice of a suitable monitoring technique or the integration of various techniques to assess the risk of failure rapidly is important.

1.3 InSAR dam monitoring

More recent attention has focused on employing InSAR for localised deformation monitoring. In contrast to large-scale monitoring applications, monitoring earthfill dams using InSAR depends on the structure's orientation, the number of SAR imagery, and the temporal and spatial

resolution of the images, as well as the processing procedure and parameters used. To date only a limited number of previous studies have examined the potential of InSAR for embankment dam monitoring (Wu *et al.*, 2010; Honda *et al.*, 2012; Voege *et al.*, 2012; Wang and Perissin, 2012; Lazecky *et al.*, 2013; Tomás *et al.*, 2013; Di Martire *et al.*, 2014; Milillo *et al.*, 2016b; Zhou *et al.*, 2016; Emadali *et al.*, 2017; Raventós and Marcos, 2017). These studies focus on embankment and concrete dams. Others have focused on examine the stability of slopes of dam's reservoir rather than the dam itself, while few studies focus on horizontal rather than vertical displacement. The majority of these previous studies validated their results using deformation models or data on fluctuation in the water level of the dam reservoir. Limited studies have compared InSAR results with those from conventional monitoring techniques such as levelling, total stations and GPS (Honda *et al.*, 2012; Voege *et al.*, 2012; Tomás *et al.*, 2013; Di Martire *et al.*, 2014; Zhou *et al.*, 2016; Emadali *et al.*, 2017). The most significant of these studies are critically summurised below.

An early example of research using InSAR for infrastructure deformation monitoring includes a study by Blom *et al.* (1999) who attempted to examine deformation at Lost Hills in California and the Aswan dam in Egypt. Although their study showed a very significant movement at Lost Hill, it did not reveal any movement in the Aswan dam. In terms of monitoring the stability of the dam's reservoir slopes and correlation of stability with the reservoir water level, Arjona *et al.* (2010) analysed two tracks of ERS and Envisat images, collected between 1992 and 2008 to monitor the areas surrounding the Itois and Yesa reservoirs in Spain. The Coherent Pixel Technique (CPT) (Mora *et al.*, 2003; Blanco-Sánchez *et al.*, 2008) was used to derive the time series and mean linear velocity of the displacement. The validation of results was based on an analytical model relating water load to estimated displacement. The results showed a vertical movement of -8 cm during 12 years at Itios reservoir and -12 cm during 15 years at the Yesa dam. However, the low coherence of the deformation map hindered the ability to investigate the stability of the dam site (Arjona *et al.*, 2010). The authors concluded that there was a good agreement between the theoretical analysis and the InSAR results. Another study conducted by Michoud *et al.* (2016) on the stability of the Argentina National Road 7. The study used 47 Envisat Advanced Synthetic Aperture Radar (ASAR) data acquired between 2005 and 2010, with 27 ascending images covering the period between January 2005 and February 2010 and 20 descending images collected between September 2007 and January 2010. There were significant gaps in the acquisitions between 2006 and 2009. Although the study focused on the inspection of a highway, the results also showed the instability of the slopes of the Potrerillos reservoir whose lies along the road. The Small BAseline Subset (SBAS) DInSAR technique

was utilized using Norut GSAR software (Larsen *et al.*, 2005). The study was initially conducted on a regional scale where no clear displacement signal was detected. Then only localized areas were processed, with different processing parameters used including the perpendicular and temporal baselines and coherence thresholds. The quality of the produced interferograms was inspected manually and only those with limited atmospheric effects were selected. The ascending data showed two unstable areas with velocities of -8 mm/year and up to -20 mm/year in the LOS direction. No significant movement over these areas was observed during 2007-2008 because only one acquisition was available during this period. Similarly, the descending data exhibited no significant movement over these areas because the direction of the platform movement was almost perpendicular to the line-of sight (LOS). However, the study focused on the stability of the main road, and there were gaps in data acquisitions, and also since the topography of the area was complex, the detection of displacement on the path of the road was difficult. Furthermore, two main landslides were detected on the boundary of the Potrerillos dam reservoir with a cumulative displacement of more than 25 mm between 2005 and 2010. It was shown that the change of the displacement rate is correlated with the variation in the water level in the reservoir. The study recommended the utilization of regular data acquisitions and a high-resolution digital elevation model (DEM) to achieve a good accuracy in the measurement of displacement.

The reservoir slopes of a dam located on Ebro River in Spain were inspected by Raventós and Marcos (2017) using 27 ascending and 29 descending images from Envisat ASAR spanning the period between 2003 and 2010 and 45 ascending images from Sentinel-1 spanning the period from 2015 to 2016. The permanent scatterers interferometry (PSI) (Ferretti *et al.*, 2000) and Quasi-InSAR (QPS) (Perissin and Ferretti, 2007) techniques were used to carry out time series analysis. It was shown that different parts of the reservoir exhibited different velocities, which decelerated between 2015 and 2016.

Grenerczy and Wegmüller (2011) investigated the stability of an embankment dam of a waste reservoir in Ajka, Hungary, before its collapse on 4 October 2010. Thirty-five descending Envisat images collected between 2003 and 2008 were used to apply a linear regression to the wrapped PSI phases to separate short-wavelength atmospheric residuals. The standard deviation of the linear regression was employed to assess the quality of the estimation. The vertical displacement was derived by projecting the LOS displacements to the vertical using imaging geometry and the incidence angle, assuming that no horizontal movement was present. The collapsed part of the embankment showed a displacement of 1.2 cm/year between March 2003

and August 2008. The study discussed the possible causes of failure, where the displacement of the embankment was quite clear even years before the event.

Wang *et al.* (2011) conducted a study at the Three Gorges dam in China using 40 Envisat images collected between August 2003 and April 2008. The construction of the dam was completed in 2003 and thus it was not completely represented in the SRTM DEM. Thus an integration of PSI (Ferretti *et al.*, 2000) and Quasi-InSAR (QPS) (Perissin and Ferretti, 2007) was performed to estimate the elevation and the displacement of the dam and the surrounding region. Initially the elevation of the area was estimated by QPS followed by PSI processing to find the cumulative displacements. The results showed that the dam was stable but that some parts of the surrounding area were moving at a rate of 10 mm/year along the LOS direction. The authors reported that the differences in the water level between the upstream and downstream sides of the dam were correlated with the magnitude of displacement. The Three Gorges dam was also investigated by Wang and Perissin (2012) using 60 COSMO-SkyMed (CSK) StripMap acquisitions from both the ascending and descending directions to examine the stability of the dam and its surrounding area. The PSI technique was employed using the SARPROZ software (Perissin *et al.*, 2011). Although high resolution images were used, the data covered only six months which is not sufficient to detect seasonal nonlinear movements (Wang and Perissin, 2012). As found by Wang *et al.* (2011), the deformation on the left river bank was obvious in both the ascending and descending datasets but the velocity was faster than the previous estimate.

Milillo *et al.* (2016b) integrated five tracks with 198 images from TerraSAR-X (TSX), COSMO-SkyMed and ALOS covering the period between 2006 and 2015 to investigate the instability of the arc-gravity Pertusillo dam in Italy. The study focused mainly on the horizontal movement of the dam. Since it is arc-shaped, the sensitivity of InSAR to movement can vary for different parts of the dam. The study discussed the sensitivity of each dataset to the radial movement of the dam. Two temperature and hydrological models were used to validate the estimated horizontal displacements of the dam. Data from different platforms and acquisition tracks were used to cover the temporal gaps present in the individual tracks. The ALOS data did not show any movement over the dam because of the small numbers of images (13). Two deterministic models, Hydrostatic Seasonal Time (HST) and Hydrostatic Temperature Time (HTT) were employed to interpret horizontal oscillations in the movement of the dam crown. The results showed good agreement between the deterministic models and displacement magnitude with $R^2 = 0.92$ and 0.89 for HTT and HST respectively.

Embankment dams have been also examined using a variety of radar data in terms of spatial resolution, temporal resolution and length of coverage. Lazecky *et al.* (2013) used 62 images from TerraSAR-X and 11 images from TanDEM-X collected between October 2008 and June 2012 to monitor the Plover Cove dam in Hong Kong. This is an embankment dam built on the arm of the ocean to separate a reservoir from the ocean for the purpose of fresh water storage. Thus, both sides of the embankment are surrounded by water. Therefore, the study focused on crest movement only. The PS-InSAR timeseries analysis was carried out using SARPROZ software (Perissin *et al.*, 2011) considering the separation of different displacement-induced components, including settlement, water level and temperature effects. The study showed a linear displacement of 4 mm/year in the whole dam body plus nonlinear movement in the range of 2-10 mm correlating with the variations in the water level in the reservoir. The effect of air temperature variation was also investigated, and the results showed that a variation of 22˚C in temperature could lead to a movement of 4 mm at any point in the dam. Additionally the dam crest on the reservoir side was subsiding at a rate of 1-2 mm/year faster than on the ocean side (Lazecký *et al.*, 2015). These results supported the explanation given by Hunter and Fell (2003) that the variation in the water level on the upstream side of the dam may lead to faster subsidence associated with the reductions in the water level which results in the strain on the upstream slope of the dam being reduced.

A study carried out by Voege *et al.* (2012) on the Svartevann dam in south west Norway used 76 ascending and 59 descending images from the European Remote Sensing (ERS-1 and -2) satellites, spanning the period 1992-2000. The study utilised the SBAS time series algorithm using GSAR software (Larsen *et al.*, 2005) to estimate the mean linear velocity and the displacement time series for the dam. The results showed that the dam movement decelerated from 25 cm/year between 1976 and 1980 to only 3 mm/year between 1992 and 2000. The velocity during the period 1976-1980 was estimated from terrestrial surveying, four years after the dam's construction was completed.

Some authors have validated their results with in-situ measurements. Di Martire *et al.* (2014) investigated the deformation of the Conza dam in Italy by using CPT-DInSAR (Mora *et al.*, 2003). Fifty-one ascending Envisat images collected between 2002-2010 and processed with the SUBSOFT (CPT) software (Mora *et al.*, 2003; Blanco-Sánchez *et al.*, 2008) were used in the study. First the correlation of the settlement with the water level was discussed. The temporal and spatial baseline thresholds were 210 days and 250 m respectively. The results from InSAR were compared to measurements from six ground extensometer sensors and root mean square error (RMS) between the two techniques was found, with $\sigma = 0.45$ cm. The study

concluded that the behaver of the dam was normal given the absence of heterogeneities in dam movements. Tomás *et al.* (2013) performed a comprehensive study of La Pedrera dam in Spain using a collection of InSAR and conventional approaches. Levelling data collected in the gallery for five epochs between 1975 and 1980 were used for the validation of the results and to interpret the dam's behaviour. The levelling observations showed a settlement in the gallery of more than 1 m between 1975 and 1980. The authors carried out a new levelling during 2011 for only 14 new benchmarks in the middle part of the gallery. This new epoch showed a settlement of 47 cm between 1980 and 2011. However, the authors argued that the major part of this settlement occurred few years after 1980 due to consolidation. ERS, Envisat and TerraSAR-X data was used to monitor the dam's surface for the period between 1995 and 2010. Time series analysis was carried out using CPT DInSAR in two steps. Initially the linear deformation was determined by fitting a model to the coherence pixels while the nonlinear movement was estimated using spatio-temporal filtering employing a spatial filter of 800 m and temporal filter of one year. The study was conducted with three different processing chains, taking different collections of datasets each time. Firstly, ERS-1, ERS-2 and Envisat images between August 1995 and May 2010 were used. Secondly, ERS-2 and Envisat data between June 2008 and May 2010 were used. In the third processing chain, data from TerraSAR-X collected between July 2008 and June 2010 were utilised. The images were multi-looked to generate images with a pixel size of 60×60 m for ERS and Envisat and 10×10 m for TerraSAR-X. A DEM with a spatial resolution of 25 m was used in the CPT processing for all datasets. The analysis focused on the investigation of the crest and the stability inspection of the gallery. The results showed settlement of 13 cm between 1995 and 2010 and of 2 cm between 2008 and 2010, which was much less than the gallery settlements. It was expected that most of the gallery settlement occurred during a few years after 1980 (before the availability of InSAR observations) and therefore it differed from settlement of the crest.

Zhou *et al.* (2016) used 21 ALOS PALSAR images spanning the period from 28 February 2007 to 11 March 2011 to monitor the Shuibuya dam in China, which is the highest rockfill dam in the world with a height of 233 m. The SBAS time series analysis showed a settlement rate of the dam crest of 10 cm/year (downwards) located at the dam centre. The study also used levelling data for eleven points on the dam's downstream slope collected between June 2006 and January 2014, while the dam was constructed between September 2001 and July 2008. The levelling data indicated a rapid settlement occurring during the first filling of the dam reservoir which continued with a slower velocity thereafter. The correlation between levelling data and InSAR velocity was found to be 0.93 with an RMSE of 1.75 cm/year.

Emadali *et al.* (2017) exploited high resolution spotlight SAR images from TSX collected between March 2014 and February 2015 to determine the rate of deformation at the Masjed-Soleyman dam in Iran. The InSAR time series analysis was performed using the SBAS time series (Berardino *et al.*, 2002) with the StaMPS software (Hooper, 2008). A comparison between GPS and SBAS velocities showed a correlation of 0.97 for all points on the dam surface, 0.95 for points on the crest and 0.99 for points on the downstream slope. The study found an obvious difference between the InSAR and terrestrial observation velocities in the transition region between the downstream and the crest, which reached 30 mm/year. The high gradient of displacement and the foreshortening factor in this area can be the reason of this difference (Emadali *et al.*, 2017).

Milillo et al. (2016a) investigated the instability of Mosul dam using Envisat data for the period 2004-2010 and Sentinel-1 and COSMO-SkyMed data for the period 2014-2016. Horizontal and vertical movements were estimated using the imaging geometry and taking the average from ascending and descending datasets. The volume of dissolution was estimated using the Markov chain Monte Carlo technique and compared to the volume of the injected materials during 2004-2012. The results showed that the continuous grouting between 2004 and 2010 kept the volume dissolution rate constant whereas it increased during 2014-2016 when the grouting work ceased.

1.4 Terrestrial dam monitoring techniques

Several terrestrial monitoring techniques have been used for investigations of dam instability (Sousa *et al.*, 2014). GPS, photogrammetry, tiltmeters, laser scanning, levelling, theodolites, electronic distance measurement and total stations are among the common instruments which are used for in situ dam monitoring (US Army Corps of Engineers, 2002). In terms of the conventional techniques, Taşçi (2008) discussed the monitoring of the Altynkaya dam in Turkey using static GPS technique. The geodetic network of this dam consists of 6 reference points and 11 monitoring pillars. The network was observed four times over two years to investigate the correlation between water level and magnitude of deformation. Because of the limited accuracy of the vertical component of the GPS, the investigation was performed on horizontal movement only. The study demonstrated a correlation between the water level in the reservoir and the magnitude of deformation. It was shown that the monitoring pillars tended to move towards the upstream direction when the water level is decreasing and towards the downstream when the water level is rising. Kalkan *et al.* (2016) compared three geodetic monitoring techniques to monitor the stability of the Ataturk dam in Turkey: precise levelling, trigonometry and GPS. Thirty-two reference points were used to monitor 200 target points

installed on the dam surface. The monitoring was carried out between May 2006 and November 2012. The work discussed the monitoring techniques used and the geodetic system in Turkey. The main three levelling lines on the dam crest were observed monthly, whereas the GPS and trigonometry observations were performed every 6 months between 2006 and 2008 and yearly thereafter. Three lines on the dam's crest, which are named upstream, centre and downstream, were observed using the three geodetic methods. The RMS difference between GPS and differential levelling results was within 2.2 cm, while that between the trigonometric and differential levelling is 1.6 cm and GPS to trigonometric RMS is 1.6 cm. The study showed greater settlement in the upstream centreline of the crest than in the downstream line.

The techniques used for dam monitoring can be selected according to the type of deformation and involved its temporal and spatial pattern. For example, GPS is effective for monitoring lateral movement; however, its performance for vertical movement can be limited. In addition, monitoring slow dam movement in a long-term timescale may not be easy. Traditional terrestrial monitoring instruments like total stations, levelling and laser scanners, are the most common approaches used in detecting dam instability. However, these can be uneconomical, time-consuming and require professional field experience. InSAR can potentially overcome these negative factors.

1.5 Problem statement and thesis layout

Several factors may threaten the stability and safety of dams. For example, karstification, water pressure, erosion, overtopping, water saturation and hydraulic gradients can impact on dam's stability (Johnston *et al.*, 1990). Thus, long-term and short-term investigations of dams are crucial. The early detection of signs of dam failure may help to allow remedial work to be carried out before the dam's collapse. Conventional monitoring methods, particularly for very large dams, are becoming less attractive due to the extensive effort and computational work needed. As described in Section 1.3, recently InSAR has been used as an alternative technique for dam monitoring. Compared with the other techniques, radar imaging systems work in all weather conditions and 24 hours a day. InSAR has been used to study large-scale geophysical events, but its applications to dam monitoring can be affected by some factors which will be discussed in this thesis. Using InSAR to investigate the stability of infrastructure can involve a trade-off. On the one hand, processing SAR data for a small-scale area is preferable as this reduce processing time. On the other hand, detecting a complex pattern of movement in a local area is not an easy task, especially when the target has complex structural details in the lateral and vertical directions.

The overall aim of this thesis is to assess the feasibility of the use of InSAR for monitoring embankment dam deformation. Datasets from four platforms, namely Envisat, COSMO-SkyMed, TerraSAR-X and Sentinel-1 are used. Integration with levelling data is carried out to monitor deformation on the Mosul dam in northern Iraq and with GPS and levelling data for the Darbandikhan dam in NE Iraq. There have been a limited number of historical studies investigating the feasibility of the use of InSAR for dam monitoring.

This thesis attempts to answer the following research questions:

1. To what extent can InSAR be used to monitor an earthfill dam's deformation? How can vertical and horizontal displacement be determined using two or more SAR tracks? How accurate is the use of InSAR to measure dam deformation?

2. How has the deformation of the Mosul dam developed over the dam surface and foundation? Is there any heterogeneity in the foundation displacements?

3. How has the Mosul dam behaved before and after the suspension of grouting work in August 2014?

4. How can different components of dam displacement be distinguished in order to determine the critical ones?

5. How can terrestrial observations be integrated with SAR data to monitor rapid displacements in earthfill dams? How has the Darbandikhan dam behaved after the 7.3Mw Sarpol-e Zahab earthquake?

This was achieved in terms of the following objectives:

1. To evaluate the stability of the Mosul dam using levelling and Envisat, TerraSAR-X, COSMO-SkyMed and Sentinel-1 data between 2003 and 2017.

2. To assess the agreement between the results from InSAR and levelling techniques concerning displacements of the Mosul dam between 2003 and 2017 using 87 monitoring benchmarks on the dam's surface and 150 benchmarks on the foundation.

3. To evaluate the behaviour of the Darbandikhan dam after the 7.3 M_w Sarpole Zahab earthquake using GPS, levelling and Sentinel-1 A/B data.

This thesis is structured as follows. Chapter 1 presents the background, aims and objectives of this PhD study. Chapter 2 introduces the principles of Synthetic Aperture Radar (SAR) and

Interferometric SAR (InSAR), as well as the major error sources of InSAR. Chapter 3 describes the water system and dams in Iraq, focusing on the main embankment dams studied in this thesis and their problematic geological settings. Chapter 4 investigates the stability of the Mosul dam using InSAR and conventional techniques. The level of agreement between the results using conventional geodetic techniques and InSAR is also presented. Chapter 5 investigates the stability of the Darbandikhan dam after the 12 November 2017 7.3 Mw Sarpol-e Zahab earthquake on the Iraq-Iran boarder using GPS, levelling and Sentinel-1 data. Chapter 6 summarises the PhD study and discusses future work to use spaceborne InSAR for dam monitoring.

Chapter 2. Principles of InSAR

2.1 Introduction

Synthetic aperture radar (SAR) is a microwave imaging technique based on the principles of the conventional radar (radio detection and ranging). Radar operates by transmitting short pulses of microwave energy into space and recording the signal backscattered from any objects encountered along the propagation path (Levanon, 1988). The returned echoes can be utilized to collect information about the target, such as its size, location, and velocity. Imaging radar operates according to a similar principle, having the ability to distinguish between individual objects. The capability to separate objects, or the imaging resolution, is partly dependent on the length of radar antenna. Given certain engineering and mathematical manoeuvres, an antenna with a suitable length can be synthesized to achieve an acceptable spatial resolution, and this is why it is known as Synthetic aperture radar (SAR) (Wiley, 1965). One further difference between the conventional radar and SAR systems is that the latter can be registered as a two-dimensional matrix of complex numbers. These complex numbers can be utilized to derive valuable information about the earth surface.

InSAR can be defined as the process of using multiple SAR images to determine small changes in elevation, at the level of centimetres or even higher accuracy, over a large area (Gabriel *et al.*, 1989). InSAR dates back to the 1970s (Zisk, 1972; Bills and Ferrari, 1977; Gabriel *et al.*, 1989) and the first spaceborne SAR mission, SEASAT, was launched in 1978 to estimate ocean wave heights (Jordan, 1980). With increasing numbers of spaceborne radar missions, InSAR has developed rapidly over the last two decades. Imaging specifications in term of spatial and temporal resolution have improved significantly, which has led to wider applications of InSAR. InSAR applications have developed especially since 1991 when the European Space Agency's ERS-1 was launched, followed by ERS-2 in 1995. The spaceborne InSAR has been successfully applied for topography mapping (Zebker *et al.*, 1992; Ferretti *et al.*, 1997b; Farr *et al.*, 2007; Krieger *et al.*, 2007; Liao *et al.*, 2007; Wegmüller *et al.*, 2009; Neelmeijer *et al.*, 2017), subsidence estimation (Gabriel *et al.*, 1989; Massonnet *et al.*, 1994; Motagh *et al.*, 2008; Motagh *et al.*, 2017), volcano monitoring (Rosen *et al.*, 1996; Beauducel *et al.*, 2000; Remy *et al.*, 2003; Spaans and Hooper, 2016), earthquake deformation (Gabriel *et al.*, 1989; Massonnet *et al.*, 1994; Motagh *et al.*, 2010; Avallone *et al.*, 2017; Polcari *et al.*, 2017; Ganas *et al.*, 2018), and lanslides assessment (Ferretti *et al.*, 2005; Bozzano *et al.*, 2011; Motagh *et al.*, 2013; Singleton *et al.*, 2014; Tomás *et al.*, 2014; Dai *et al.*, 2016; Darvishi *et al.*, 2018).

This chapter focuses on the main aspects of spaceborne imaging radar. Initially, a brief introduction to the history of InSAR and its main applications is given. The principles of the synthetic aperture radar are discussed in section 2.2, followed by the principles of InSAR and sources of errors in section 2.3. The InSAR time series is discussed in section 2.4.

2.2 Synthetic Aperture Radar (SAR)

Imaging radar is a complex topic, but the general idea is not complicated. The operation starts with the transmission of a series of electromagnetic pulses with a specific pulse repetition frequency (PRF), and the amplitude and phase of the transmitted signal are known. Typical values of PRF range between 1 and 10 KHz (Bamler and Hartl, 1998). The backscattered echoes from targets on the ground represent successfully recorded echoes. If the transmitted signal is considered to be a function of time p(t), the signal returned by a target located *x* metres away from the platform antenna can be represented as follows (Ferretti, 2014):

$$s_r(t) = A\cos[2\pi f_0(t-\tau)] = A\cos\left[2\pi f_0 t - \frac{2\pi}{\lambda}2x\right] = A\cos[2\pi f_0 t - \phi] \quad (2.1)$$

where $\tau = 2x/c$ refers to the two-way travel time of the backscattered signal, c is the speed of light, φ is the phase shift between the transmitted and received signals, λ and f_0 are the wavelength and frequency of the radar signal respectively, and A is the attenuation factor since the backscattered amplitude is much smaller than that of the transmitted signal.

Figure 2.1 shows how the returned signal phase is related to the distance between the sensor and the target. If the acquisition is repeated for the same area, the differences in the phase measurements can be converted into a displacement map of the targets and this is the basic concept of InSAR which is described in greater details in section 2.3.

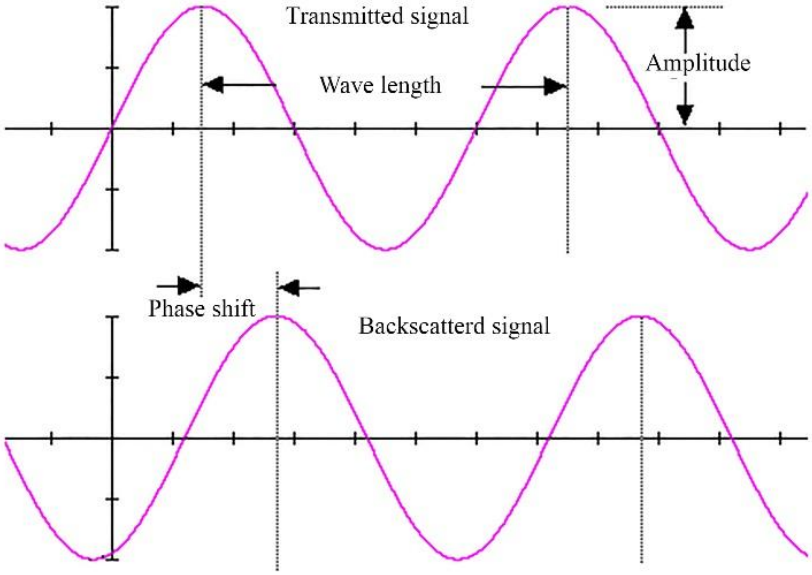

Figure 2.1. Phase shift between transmitted and backscattered signals (Ferretti *et al.*, 2007)

2.2.1 SAR image formation

SAR refers to the operation of the mathematical synthesis of a long radar antenna, exploiting the motion of the platform in the along-track direction, to achieve acceptable azimuth resolution (Wiley, 1965). The length of the synthesized antenna is proportional to the time of illumination of the surface objects. After a few steps of demodulation, sampling and conversion from analogue to digital form, the returned signal is converted into a matrix of complex numbers. Demodulation is carried out by applying two processing channels, I and Q which are illustrated in Figure 2.2 (Ferretti, 2014). Each channel involves two steps of demodulation and filtering. In channel I the signal is multiplied by the original carrier and then passed to a low-pass filter to remove the high-frequency part as follows (Ferretti, 2014):

$$s_r(t).\,2\cos[2\pi f_0 t] \Rightarrow A\cos[2\pi f_0(t-\tau)].\,2\cos[2\pi f_0 t] \\ = A\cos[2\pi f_0\tau] + A\cos[4\pi f_0 t - 2\pi f_0\tau] \tag{2.2}$$

where f_0 and λ are the carrier signal frequency and its wavelength respectively and τ is the time difference between the times of transmission and reception.

In equation (2.2), the final term is merely double the frequency of the carrier and this can be removed by the low-pass filter as follows (Ferretti, 2014).

$$s_r(t).\,2\cos[2\pi f_0 t] \Rightarrow A\,cos[2\pi f_0\tau] = A\,cos\left(\frac{4\pi}{\lambda}x\right) = A\cos(\phi) = i(t) \tag{2.3}$$

In channel Q, the signal is multiplied by the carrier with a 90˚ phase shift and a low-pass filter is similarly applied to yield (Ferretti, 2014):

$$s_r(t).\,2\sin[2\pi f_0 t] \Rightarrow A\,sin[2\pi f_0 \tau] = A\sin\left(\frac{4\pi}{\lambda}x\right) = A\sin(\phi) = q(t) \qquad (2.4)$$

where i(t) and q(t) are the two main components of the raw data recorded by the sensor used to generate the SAR image. In the following sections, several extra steps are discussed by which these two components can be converted into another form of information before the formation of the complex image. In this discussion, it is assumed that the transmitted and received signals are identical in frequency f_0, and only the amplitude and phase vary. Thus, it will be easier to represent the backscattered signal as a complex number *z*:

$$z = Ae^{j\phi}\,, j = \sqrt{-1} \qquad (2.5)$$

This complex number contain information about the amplitude and phase of the backscattered signal. The typical wavelengths used in SAR imaging systems range between 1 and 100 cm, corresponding to the Ka to P bands. In contrast to optical imaging systems, SAR is applicable in all weather conditions due to its ability to propagate through clouds and rainwater drops and to operate in both the day and at night (Richards, 2009).

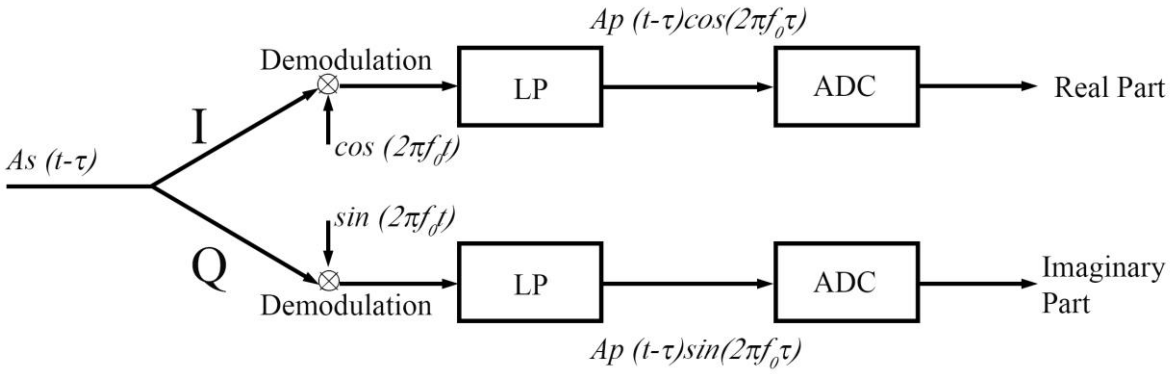

Figure 2.2. Demodulation of the SAR signal by two channels I and Q adopted from (Ferretti, 2014)

2.2.2 Image range resolution

Generally, several objects may contribute to backscattered echoes. The time delay between the transmission and reception of the signal is a function of the distance between the sensor and the object on the ground. The ability to distinguish between two objects in the range direction depends on the pulse duration. In other words, no two objects can be distinguished from one another unless their distance is greater than the 2-way travel distance of the pulse duration T_p (Reigber, 2001):

$$\Delta r \geq \frac{c}{2} T_p \tag{2.6}$$

where Δr is the smallest distance between the two objects to be separated from each other on the image scene and c denotes the speed of light. For example, if T_p is 100 μs, the range resolution is Δr≈15 km (Ferretti, 2014). It is clear from equation (2.6) that a high range resolution requires a very short pulse duration. But with a short pulse, the backscattered energy can be undetectable because its magnitude is 10^{-11} less than the transmitted signal (Hanssen, 2001). Thus, the returned signal needs to be amplified to a magnitude comparable to that of the transmitted signal, otherwise the returned signal cannot be distinguished from the background noise. This problem has been resolved by using the frequency modulation (FM) of the transmitted pulse, in so-called chirp compression. Here rather than sending a short rectangular pulse, the signal is modulated to a chirp of frequencies with a specific bandwidth (BW). The received signal is autocorrelated with the original replica of the chirp to derive a sinc function, such as sin(x)/x (Oppenheim *et al.*, 1983). The sinc function is a rectangular spectrum having an amplitude larger than zero only within the chirp bandwidth. This process is called range compression and can improve the range resolution to the sub-meter level. The range resolution after the range compression turns to (Ferretti, 2014):

$$\Delta r \geq \frac{C}{2BW} \tag{2.7}$$

where BW is the chirp bandwidth. If equation (2.7) is applied to the previous example taking the maximum range bandwidth of 100 MHz, the range resolution can be improved to Δr≈1.5m (Reigber, 2001; Ferretti, 2014). From equation (2.7) it can be seen that the range resolution is independent of slant distance.

Before storing the echoes, the signal needs to be converted into a digital form. This can be achieved by sampling the signal with a sampling frequency f_s. The sampling frequency rate determines the pixel size of the SAR image, but the spatial resolution is controlled by the BW. In other words, it is not possible to increase the range resolution by increasing the range sampling rate. After applying range compression, the returned signal can be written as (Ferretti, 2014):

$$s(n) = \sum A_i \frac{\sin[\pi BW \left(\frac{n}{f_s} - \tau_i\right)]}{\pi BW (\frac{n}{f_s} - \tau_i)} e^{j\varphi_i} . e^{j2\pi f_0 \tau_i} \tag{2.8}$$

where *n* represents the number of scatterers within a single cell.

From equation (2.8), it is obvious that the backscattered values for a specific range cell are the summation of the contributions from several backscattering elements within the resolution cell. This means the amplitude of a single image cell has a Rayleigh distribution (Hanssen, 2001). Thus, scattering objects with high reflectivity may dominate the amplitude and the recorded phase for this range. Furthermore, if these scatterers are strong enough, they may impact even upon objects located tens of metres apart from the resolution cell, because the sinc function is not limited to a specific range distance. This effect is called sinc sidelobes (Gatelli *et al.*, 1994a).

2.2.3 Azimuth compression and resolution

In all SAR systems, microwave energy is transmitted by an antenna having a length (l_a) and width (d_a). To avoid receiving echoes from points at the same distance from the antenna, the antenna is directed toward the right or left direction. However, some new systems have been designed to transmit at both sides, but not at the same time. COSMO-SkyMed is one example of such a system. The antenna is inclined to the nadir with a specific angle called the incidence angle, while the direction of the line-of-sight (LOS) is known as the slant range. To avoid the effect of the relative motion between the radar antenna and the Earth's surface during the Earth's rotation, the antenna is squinted from the azimuth direction at a small angle (for example ±2 degrees for COSMO-SkyMed and ±0.9 degrees for Sentinel-1). The beam width dimensions in the cross-track and along-track directions (β_r, β_a) can be respectively approximated as:

$$\beta r \approx \lambda R/da \tag{2.9}$$

$$\beta a \approx \lambda R/la \tag{2.10}$$

where R refers to the slant distance and d_a and l_a are the antenna width and length respectively. Antennas with small dimensions transmit wide beams, which leads to less focused footprints. For example, a radar antenna with a length of 15m onboard a platform having a slant range of 800 km gives an azimuth resolution of 3km (Reigber, 2001). This problem was solved by Wiley (1965) who exploited the repetition of target acquisitions while the platform moves along its orbit. This led to the synthesise of a long aperture that can reach up to a few kilometres. The length of the synthetic aperture equals the length of the flight distance from which a target can be illuminated. This is the basic idea of synthetic aperture radar (Wiley, 1965). Figure 2.3 shows the formation of a synthetic aperture, considering only one dimension of the antenna for simplicity (Richards, 2009).

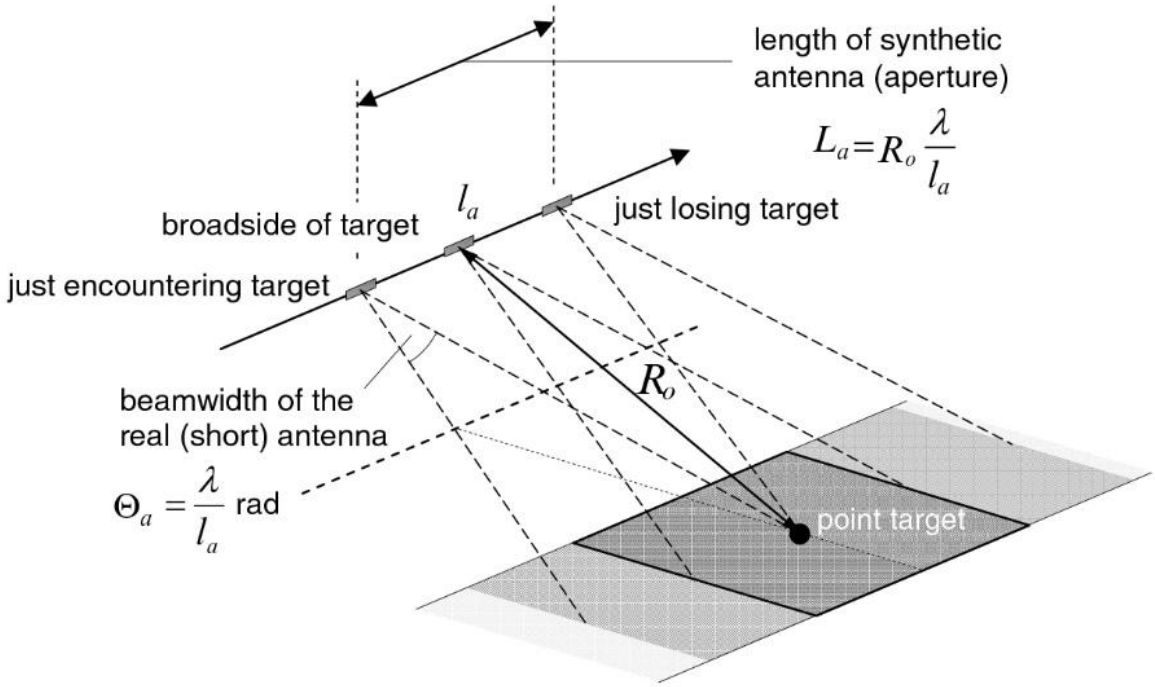

Figure 2.3. The concept of SAR, employing the motion of the platform to synthesize a long antenna. The antenna footprint is illustrated as a rectangle for simplicity (Richards, 2009).

Adopting this theory can improve the azimuth resolution from $R_a=R\lambda/L$ in the real aperture radar (RAR) to $R_a=l_a/2$ in the synthetic aperture radar (SAR). Taking ERS as an example, this can improve the azimuth resolution from 4.8 km to 5m (Ferretti, 2014).

2.2.4 SAR image focusing

An object on the ground is illuminated with several bursts while the aperture scans the Earth's surface in the along-track direction. In other words, any single point will be observed from different azimuth coordinates, resulting in a parabolic range trajectory (Figure 2.4). The range and phase of one scatterer are not identical to those from other scatterers. Thus, for each scatterer, the range and phase from all observations are combined coherently to obtain a complex signal. This process is known as azimuth focusing. In general, there are two categories of image focusing are described in the literature in either the wave-number and range-doppler (Bamler, 1992). For the purpose of the present discussion, we focus on the second of these as it is the focusing algorithm adopted in GAMMA. Knowing the imaging geometry of the radar, the echoes from all scatterers within each resolution cell can be determined. Then the different contributions are integrated by applying a matched filter. The final output of azimuth focusing is a complex SAR image, represented as a matrix of complex numbers. Each resolution cell has a pair of range and azimuth coordinates. The complex numbers contain the amplitude information which refers to the backscattered energy, and the phase which partially refers to the sensor-target distance.

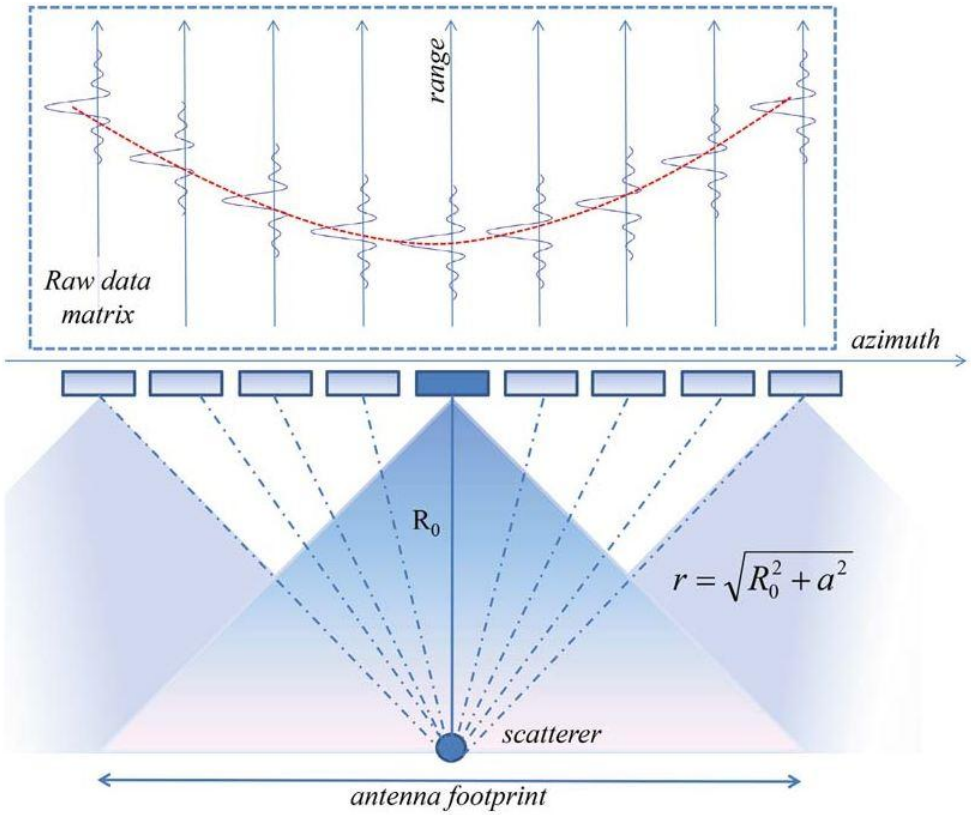

Figure 2.4. Variation in range and azimuth coordinates for point-wise scatterers (Ferretti, 2014).

Another essential step in SAR image formation is the radiometric calibration (Gelautz *et al.*, 1998). Intensity is correlated with the cell size and thus this correlation needs to be adjusted by normalization. The normalized value is known as sigma naught σ° (Wegmüller and Werner, 2011). This step is essential to retrieve the radar cross section (RSC) of the target. The RSC can be defined as the cross-section of an optimal reflecting sphere that would reflect the same amount of energy from the target. The higher the RCS of a target, the larger the amount of energy it scatters back to the radar.

2.2.5 Multi-looking

The coherent combination of different backscatters within the resolution cell causes a speckle noise in the SAR scene due to the Ryleigh distribution of the amplitude of the scattering objects (Bamler and Hartl, 1998). This noise can be significantly reduced by averaging the squared amplitude (the intensity) of several adjacent pixels. This process is known as multi-looking (Li *et al.*, 1983). The higher the multi-looking factor, the more the speckle noise can be reduced, but at the cost of spatial resolution. Multi-looking reduces the variance of the intensity by $N_r \times N_{az}$ (Ferretti *et al.*, 2007) where N_r and N_z are the multi look factor in the range and azimuth directions respectively.

2.2.6 Geometric distortion

Radar imagery are distorted geometrically according to the imaging geometry and the terrain topography. Pixels in the near range cover slightly smaller ground areas than those in the far range because of the side-looking view. Therefore, the resolution of the image along the radar's line of sight varies. In spaceborne radar, this distortion can be easily corrected using the sine of the local incidence angle (Richards, 2009). More problematic type distortion occurs when the topography of the illuminated area is complicated, and the incidence angle varies locally.

Earth-fill dams often have two slopes with opposite orientations of 180˚ (Figure 2.5). To better understand the feasibility of using InSAR for dam deformation monitoring, it is necessary to discuss the relationship between imaging geometry and dam orientation. In section 2.2.2 it is shown that the position of the scatterer along the cross-track line depends on the time that the signal takes to return to the sensor. Thus, the returned signal can be considered as the projection of the terrain surface onto the LOS vector. Figure 2.5 shows how the incidence angle varies according to the slope of the dam surface. In other words, slopes having orientations facing the sensor look brighter than those directed away from the sensor because the foreshortening increases the radar intensity. The cell size in the ground range direction is a function of the angle between the local vertical (the line perpendicular to the local terrain) and the LOS vector (β). For the sake of simplicity, the azimuth of the LOS in Figure 2.5 is assumed to be perpendicular to the dam's main axis. For points on the dam crest, the spatial resolution can be represented as (Richards, 2009)

$$r_g = \frac{c\tau}{2sin\theta} \tag{2.11}$$

where τ is the pulse duration. In contrast, on the left slope shown in Figure 2.5, the local incidence angle becomes ψ=β-θ.

$$r_g = \frac{c\tau}{2sin\psi} \tag{2.12}$$

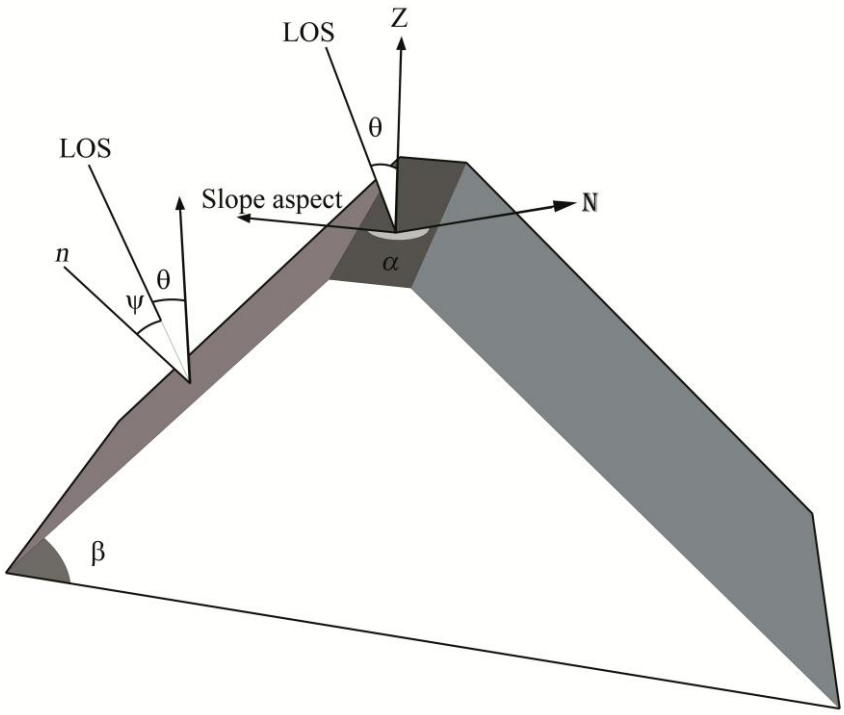

Figure 2.5. Geometry of radar imaging on an earth-fill dam. The local incidence angle depends on the slope of the dam surface.

Furthermore, the local incidence angle of the slope surface may increase or decreases depending on the surface orientation and slope with respect to the LOS and, as a result, the compression, (so-called foreshortening) factor varies across the SAR image. Figure 2.6 shows the effect of foreshortening on two Envisat images from ascending and descending passes acquired over the Mosul dam. Further discussion of the effect of foreshortening on the embankment dam can be found in Chapter 5 and 6. It is obvious that the dam slope on the downstream side is slightly wider in the descending image than it is in the ascending image due to differences in the foreshortening effect.

Another type of distortion can happen when the signal from the top of the terrain reaches the radar before the echoes backscattered from the lower terrain. This distortion is known as layover and it can flip features upside down on the SAR image. However, this effect depends mainly on the slope of the dam for a given radar satellite. Nonetheless, if one side of the dam is affected by layover, it is very likely that images from the reverse pass (ascending or descending) will not be similarly affected, and hence one of the two passes may be reliable for an interferometry application. More discussion of the geometrical distortion of images acquired over dams is presented in Chapter 6.

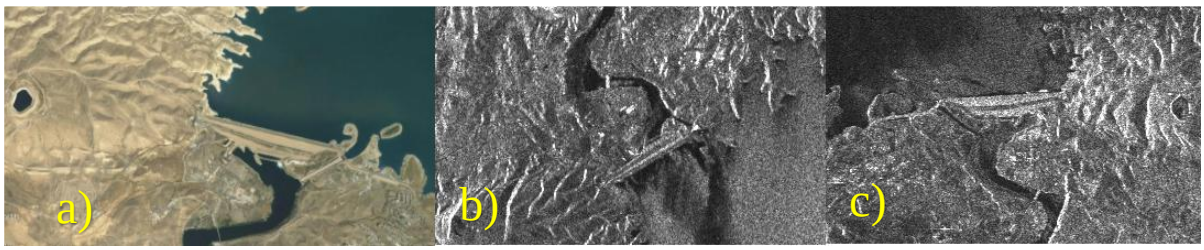

Figure 2.6. Foreshortening effect on Envisat images acquired over the Mosul dam: (a) Satellite image from Google earth; (b) Envisat ASAR image from ascending track 42; and (c) Envisat ASAR image from descending track 135.

The pass direction and the geometrical baseline are important factors in selecting SAR images for monitoring applications. To a lesser extent, the incidence angle can also play an important role in selecting SAR data. To avoid geometrical distortion in InSAR applications, the choice of direction of pass and incidence angle have to minimize, if not eliminate, the geometrical deformation (Ferretti *et al.*, 2007). The considerations of using InSAR for dam deformation monitoring are discussed in Chapter 6.

2.3 SAR interferometry

Although SAR images represent a valuable source of information about surface backscattering properties, Interferometric SAR (InSAR) is able to provide additional information by exploring phase observations. The two main interferometric applications are the topographic mapping and deformation monitoring. For the latter, InSAR has been widely used to investigate landslides, earthquakes, surface subsidence due to oil and water withdrawal, volcanic eruptions, glacier flow and land mass monitoring (Gabriel *et al.*, 1989; Wright *et al.*, 2004a; Cigna *et al.*, 2014; Singleton *et al.*, 2014; Dai *et al.*, 2015; Chen *et al.*, 2016; Dai *et al.*, 2016; Darvishi *et al.*, 2018). Additionally InSAR has been used successfully in topography mapping (Graham, 1974; Gabriel *et al.*, 1989; Zebker *et al.*, 1992; Ferretti *et al.*, 1997b; Wegmüller *et al.*, 2009; Rossi and Gernhardt, 2013; Baade and Schmullius, 2016; Neelmeijer *et al.*, 2017). Furthermore, InSAR has been integrated with independent datasets such as GPS and levelling for the validation and/or mitigation of noise (Williams *et al.*, 1998; Li, 2005b; Li *et al.*, 2006c; Gourmelen *et al.*, 2010; Hammond *et al.*, 2010; El-Gharbawi and Tamura, 2014; Yu *et al.*, 2018a). In all InSAR applications, the basic idea is to estimate the variation in phase from two SAR images of the same area acquired from two different positions at the same time or different times. The distance between acquisition locations is called the geometrical baseline and its perpendicular component to the LOS is known as the perpendicular baseline. The Interferogram is determined by differencing the phase of the two acquisitions. More precisely, it can be generated by multiplying the first complex number from the first acquisition by the conjugate of the second

one. Further details of the interferometric applications can be found elsewhere (Li and Goldstein, 1990; Rodriguez and Martin, 1992; Rocca *et al.*, 1997; Massonnet and Feigl, 1998b; Franceschetti and Lanari, 1999; Bürgmann *et al.*, 2000; Gens and Van Genderen, 2007; Ferretti *et al.*, 2011). The first application for surface movement monitoring was performed by Gabriel *et al.* (1989) who used SEASAT images to estimate the inflation and subsidence of the ground as a consequence of water absorption.

2.3.1 Interferometric phase

A SAR image is a matrix of complex numbers which can be used to determine the reflection intensity, amplitude and phase for each pixel. The interferometric phase of a pixel from two SAR images consists of five components: flat earth, topography, deformation, atmospheric delay and noise. Equation (2.13) shows these components, and the geometry of the interferometry is depicted in Figure 2.7. The differential phase between any two points, *P* and P_0 in the interferogram is determined as follows (Ferretti *et al.*, 2007):

$$\Delta\emptyset(P, P_0) = \frac{4\pi}{\lambda}\frac{B_n}{R_{m0}}\frac{\Delta r}{tan\theta} + \frac{4\pi}{\lambda}\frac{B_n}{R_{m0}}\frac{h}{sin\theta} + \frac{4\pi}{\lambda}d + \alpha + n \qquad (2.13)$$

where B_n is the perpendicular baseline, R_{m0} is the range distance between the target and the antenna in the first acquisition, Δr is the variation in antenna-target range due to the change in acquisition positions, h is the relative height between point P_0 and P_1, θ is the radar beam incidence angle, α is the atmospheric delay, n is the noise from multiple sources but mainly decorrelation and sensor thermal variation, and d is the deformation in P projected onto the LOS. The interferometric phase (Δφ) may compromise further components related to changes in the target's physical properties, although this component can be cancelled out when the properties of backscatters remain identical between the two acquisitions. In equation (2.13), the first component is known as the flat earth which results from a change in the acquisition position and it is so named because it would be the only component that could be seen if the earth was completely flat with no topography or curvature. The second component is the contribution of the topography which arises from the variations in the height of the terrain while the third component is the displacements contribution. The first and second parameters can be eliminated using precise baseline measurements and a suitable elevation model. Any uncertainty in the baseline and the elevation model could introduce phase residues in $\Delta\emptyset$. Separating these residues from each other, or at least from variation in atmospheric delay and noise is not an easy task. The residual of the phase from the DEM error is highly correlated with the length of perpendicular baseline. The elimination of the atmospheric delay is discussed below in section

2.3.5. Removing the flat earth, topography and atmospheric components theoretically leaves the interferometric phase which is only related to the terrain deformation.

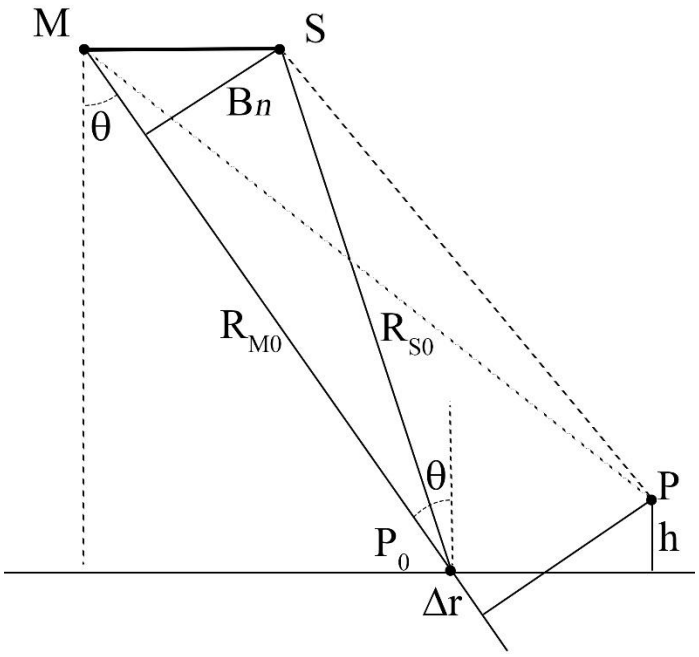

Figure 2.7. The geometry of SAR interferometry (Lu and Dzurisin, 2014)

The phase is also modulus ($-\pi, \pi$) and the ambiguous integer number of wavelengths should be estimated. Depending on the perpendicular baseline, sensitivity of the phase variation to the local topography is much less than the sensitivity to the change in the topography (Lu and Dzurisin, 2014). In other words, interferometric pairs with long baseline are more sensitive to the topography mapping. However, the length of the perpendicular baseline is a trade-off because it may lead to the loss of the interferometric signal due to the geometrical and volume decorrelation when its length is comparable to that of the critical baseline which is discussed in section 2.3.2.

The height range which corresponds to a full phase cycle is known as the height of ambiguity. Its value can be computed as follows (Massonnet and Feigl, 1998a):

$$\Delta h_{2\pi} = \frac{\lambda}{2}\frac{R_{m0} sin\theta}{B_n} \tag{2.14}$$

where R_{m0} is the range distance between the target and the antenna in the master image, λ is the wavelength of the SAR system, θ is the viewing incidence angle and B_n is the perpendicular baseline. If the variation in the local terrain is less than the height of ambiguity, an unwrapping step is unnecessary (Usai and Klees, 1999).

In repeat-pass InSAR, topography mapping can be more challenging due to variations in atmospheric delay (Goldstein, 1995; Zebker *et al.*, 1997; Li *et al.*, 2005). Meanwhiles in the single-pass, the atmospheric delay can be cancelled out because it is almost identical in two acquisitions. In the repeat-pass systems, baseline uncertainties may propagate into large errors in terrain height. Thus, a refinement of baseline can be achieved by exploiting a low-resolution DEM. Similar to their challenging effect in deformation mapping, the decorrelation and thermal noise introduce random phase error and ultimately prevent the estimation of terrain height.

The Shuttle Radar Topography Mission (SRTM) was an 11-day mission launched by the National Aeronautics and Space Admission (NASA) to achieve global DEM coverage (Farr *et al.*, 2007). The shuttle was equipped with C- and X-band synthetic radar. In addition to the transmit/receive antennae for each system, tow receiver antennae of C- and X-band are fixed with a 60 metres mast allowing for single pass interferometry for both systems. The shuttle orbited at an altitude of 223 km and with incidence angle between 30 and 60 degrees in order to achieve a swath coverage of 50 km for the X-band and 255 km for the C-band. This achieved an approximate ground resolution of 30 m (Ferretti *et al.*, 1997a).

The TanDEM-X mission introduced unprecedented accuracy in global InSAR DEM accuracy (Krieger *et al.*, 2007). The mission consisted of a twin of X-band constellation which was employed to generate global DEM coverage with an accuracy higher than that of the SRTM DEM. This was achieved by controlling the twin platforms to work synchronously in a single-pass mode and with a typical baseline of 200-500 m. The synchronization of the acquisitions resulted in highly mitigated atmospheric artefacts. The TanDEM-X mission achieved a global-scale coverage with a relative resolution of 2 m and an absolute resolution of 10 m (Krieger *et al.*, 2007).

In this study, both SRTM and TanDEM-X DEMs are used in the interferometry processing. The SRTM is used as an auxiliary DEM to refine the TanDEM-X DEM generated from a pair of TerraSAR-X and TanDEM-X images acquired in 2012.

Several noise sources can impact an InSAR observations, including atmospheric effects, temporal and geometric decorrelation, unwrapping errors and sensor temperature. Figure 2.8 shows the workflow of InSAR for deformation mapping, starting with two acquisitions acquired at two different times. The main steps include co-registration, interferometry, differential interferometry, coherence estimation, phase unwrapping and geocoding. Each of these steps is discussed further in the following sections.

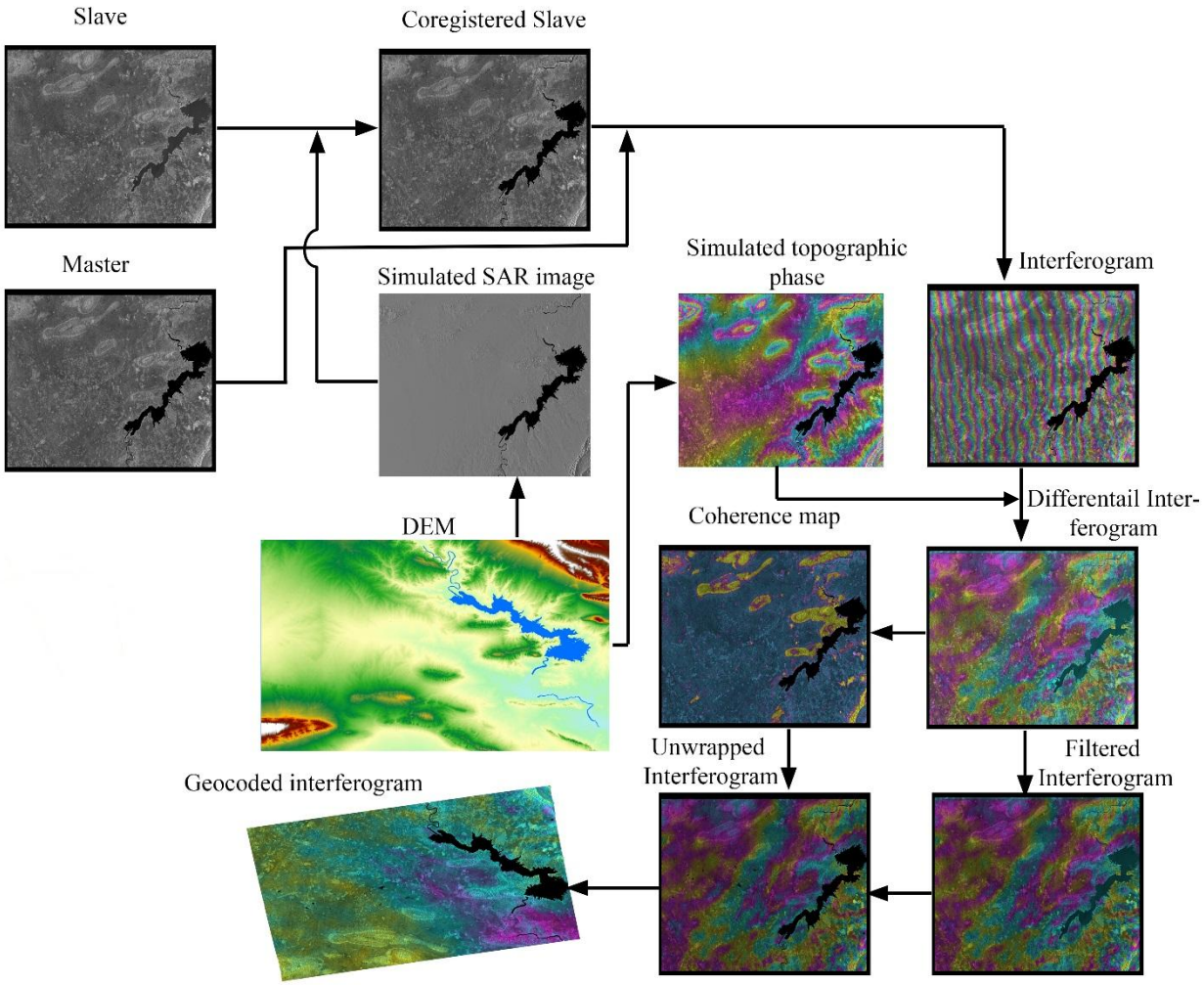

Figure 2.8. The workflow of InSAR processing.

2.3.2 Interferogram coherence

Phase noise can be expressed by means of local coherence. This is an estimation based on the cross-correlation coefficient of the complex values of two acquisitions extracted using a kernel window of a few pixels in size. Two types of phase decorrelation can be present in an interferogram (Ferretti *et al.*, 2007; Ferretti, 2014): geometrical and temporal decorrelation. Geometrical decorrelation is directly related to the length of the baseline. Given that the phase of a single resolution cell is the association of multiple scatterers within this cell, changes in the relative positions of these scatterers result in changes in phase contributions of each scatterer. Consequently, the interferometric phase is decorrelated (Zebker *et al.*, 1992). The backscattered signal is dominated by echoes from scatterers having similar dimensions to the radar wavelength. Thus short wavelength systems are exposed to high decorrelation effects because small scatterers are more likely move with respect to each other than are the larger scatterers (Hooper *et al.*, 2012). Substantial differences in viewing angle reduce the coherence of the interferogram because they lead to shifts in the reflected spectra between two SAR acquisitions (Prati *et al.*, 1994). If the shift in the spectra is smaller than the bandwidth, then the two

acquisitions should have a common range of frequencies known as the common bandwidth. Thus, there will be a threshold of the difference in the viewing angles for which the reflected spectra from the two SAR acquisitions are completely uncorrelated, where no common band is found. In such a case, the perpendicular baseline is called the critical baseline which can be computed as follows (Richards, 2009):

$$B_{nCrit} = \frac{\lambda R_0}{2 r_g cos\theta} \tag{2.15}$$

where r_g is the range resolution. On the other hand, a lack of coherence can arise due to the low signal-to-noise ratio (SNR). The SNR is related to the similarity in the reflectance of the scatterers during the two acquisition and it can be defined as the ratio of the power of the common band signal to the difference in power of the two signals (Patri and Rocca, 1992). In general, a high signal to noise ratio (SNR) is essential to achieve suitable coherence.

The value of coherence can be estimated as follows (Patri and Rocca, 1992):

$$\gamma = \frac{E[Z_1 Z_2^*]}{\sqrt{E[|Z_1|^2]E[|Z_2|^2]}} \tag{2.16}$$

where E[.] is the expectation value and * is the conjugate of the complex value.

Furthermore, the SNR can be expressed as a function of coherence (Prati *et al.*, 1994):

$$SNR = \frac{|\gamma|}{1 - |\gamma|} \tag{2.17}$$

The value of coherence of an interferogram can range between zero and one. It is zero when the two signals are entirely uncorrelated, and one when the signals are fully correlated (with zero noise) (Zebker *et al.*, 1992; Prati *et al.*, 1994).

2.3.3 Image Co-registration

Image co-registration is vital for SAR interferometry. It refers to aligning the master and slave images in such a way that each pixel in the slave image corresponds to its counterpart in the master image. Different acquisition geometry leads to non-aligned images. Consequently, the size of the images in terms of the numbers of pixels in the azimuth and cross-track directions is not identical. Co-registration is carried out in coarse and fine co-registration steps (Hanssen, 2001). Coarse co-registration finds the offsets in both the azimuth and range directions. This can be achieved by using visual inspection, orbital information, the intensity of the images and/or the phase statistics (Gabriel and Goldstein, 1988; Bamler and Hartl, 1998; Small, 1998;

Scheiber and Moreira, 2000). The accuracy of coarse co-registration can reach a few pixels. In order to achieve sub-pixel accuracy, the fine co-registration is carried out by fitting a polynomial model to the master and slave images. To determine the polynomial coefficient which refers to the shift, rotation and skew between the master and slave images. Figure 2.9 shows the geometrical distortion between a pair of SAR images. Co-registration should account for all types of distortion namely range and azimuth shift and skew and rotation. It can be conducted as follows (Ferretti *et al.*, 2007):

$$x_s = a.{x_m}^2 + b.x_m + c.y_m + d \qquad (2.18)$$

$$y_s = e.{x_m}^2 + f.x_m + g.y_m + h \qquad 2.19)$$

where x_s , y_s , x_m ,y_m are the slant range and azimuth coordinates in pixels in the slave and master images respectively, and a-h are the polynomial coefficient.

The polynomial coefficients can be determined by subsetting the images for a few patches and finding the shift in the azimuth and range directions for each patch. Then the model in equation (2.18) can be applied for each patch using the least squares approach to calculate the polynomial parameters. The patch size should be compatible with the image size. The amplitude cross-correlation and/or fringe contrast can be used to match the patches and to find the common pixels between the slave and master images. For areas with high variation in topography, the fringe dependent-method may result in low accuracy due to the high phase gradient. The amplitude-dependent method is the most commonly used approach, but it may need a high SNR and, consequently, a large patch window is needed. The last step in the co-registration process is to resample the slave image to the radar coordinate system of the master image by using the polynomial equations in (2.18).

For a conventional StripMap, an accuracy of 0.1 pixels can be sufficient to produce an interferogram of high quality. Lower levels of co-registration accuracy increase the phase standard deviation and hence considerably decrease the interferogram coherence (Scheiber and Moreira, 2000).

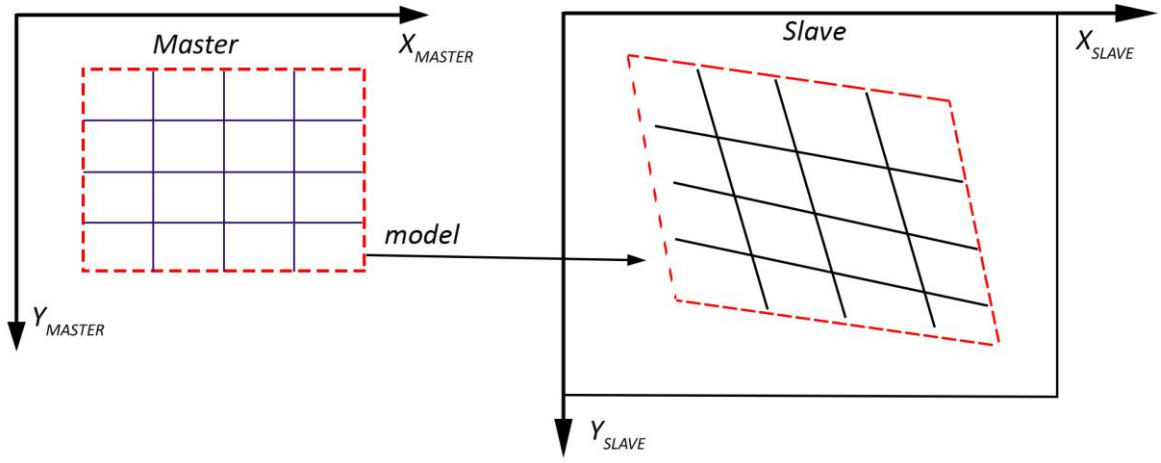

Figure 2.9 Image co-registration. The process should account for range and azimuth shift and skewing and rotation (Ferretti et al., 2007).

In Sentinel-1 TOPS mode, the antenna squinted significantly in the along-track direction (De Zan and Guarnieri, 2006) to achieve wide coverage of three sub-swathes with several bursts in each. The overlap between adjacent bursts is 7-8% of the burst size. If co-registration accuracy is not quite sufficient, the difference in Doppler frequency between the adjacent bursts introduces a phase ramp in both the cross-track and along-track directions (Scheiber and Moreira, 2000). Although the accuracy of intensity cross-correlation can reach 0.05 pixels (Li and Goldstein, 1990), its performance for the co-registration of TOPS mode images for Sentinel-1 is not satisfactory. Therefore, a phase jump is clearly introduced in the overlap area between the adjacent bursts and specifically in the azimuth direction. To mitigate this phase jump, an extra step is required to enhance the polynomial coefficient by exploiting the phase statistics in the area where the bursts overlap (Scheiber and Moreira, 2000). Spectral diversity is applied to achieve an accuracy better than 0.005 pixels in the azimuth direction when coherence is sufficient (Wegmüller *et al.*, 2015).

2.3.4 Interferogram filtering and phase unwrapping

One of the limitations of imaging radar is the phase ambiguity of SAR images. More precisely, the measured phase is modulus (wrapped) to $(-\pi, \pi)$, and consequently the differential phase in the interferogram reveals only a fraction of the real phase difference between the two acquisitions. The ambiguous integer number of cycles should be added to the modulus phase to estimate the real phase difference. The process of adding the integer number of cycles is known as the unwrapping process. The decorrelation of the interferometric phase discussed in 2.3.2 can be the main reason for unwrapping errors and may result in significant error in the deformation estimation and/or topography mapping. Thus, mitigating the noise level prior to unwrapping is crucial. This can be achieved using two approaches. The first involves the band

pass filtering of the SAR images before the interferogram formation (Gatelli *et al.*, 1994a), and the second filters the interferograms in the spatial domain. Interferometric filtering can improve the quality of the interferograms significantly, and it is essential to generate a good quality unwrapped interferogram. Adaptive filtering mitigates the noise level depending on the amplitude dispersion and phase rate. However, this type of filtration can reduce the spatial resolution. One of most effective filtering algorithms was developed by Goldstein and Werner (1998) and there have been some attempts to improve this algorithm (Baran *et al.*, 2003; Li *et al.*, 2008). In a different approach, Deledalle *et al.* (2011) proposed non-local filtering based on pixel similarity to preserve the resolution of the filtered interferogram.

As mentioned above, phase unwrapping is the process of recovering the full number of wavelengths for each pixel in the interferogram (Ghiglia and Pritt, 1998). The high gradient interferometric fringes in the complex topography regions need to be removed before the unwrapping. Some unwrapping algorithms such as 2D unwrapping algorithms, work on each interferogram individually (Goldstein *et al.*, 1988; Costantini, 1998; Zebker and Lu, 1998; Chen and Zebker, 2000; Chen and Zebker, 2001; Sowter, 2003; Loffeld *et al.*, 2008), while others work on the 3D domain utilizing multiple interferograms (Huntley, 2001; Cusack and Papadakis, 2002; Salfity *et al.*, 2006; Hooper and Zebker, 2007).

The performance of filtering and unwrapping algorithms depends on the level of noise, the fringe rate and the physical properties of the area of interest. Thus, experimenting with different filtering and unwrapping parameters can optimize the unwrapping results.

2.3.5 Geocoding

Geocoding refers to the transformation between Range-Doppler Coordinates (RDC) and the conventional coordinates such as WGS84 (φ, λ, H), where φ, and λ are the latitude and longitude respectively and H is the ellipsoidal height (Hanssen, 2001). Geocoding can be achieved by determining the mathematical relationship between the two systems. Once the relationship between the two systems is known, a transformation from map to radar coordinate systems or vice versa is straightforward. To determine the mathematical relationship, a several steps need to be followed (Richards, 2007; Wegmüller and Werner, 2011). Knowing the geometry of the SAR system, for each pixel in the DEM map, the position of the platform and acquisition time can be computed. The look vector for each pixel which is the vector from the pixel pointing to the platform antenna, is used to determine the pixel's azimuth and slant range in the radar coordinate system. This process is repeated for each pixel in the DEM to generate a look-up table (LUT) for all pixels in the DEM file. In GAMMA, the LUT is a matrix of complex

numbers with a size equal to that of the DEM file. The real and imaginary parts of each element are the radar coordinates of the corresponding pixel in the master SAR image. The LUT can then be used to transform between map and radar coordinate systems. Additionally, it can be used to simulate a SAR image using an elevation model. The simulated SAR image can be used in refining the LUT and in co-registration process as discussed in section 2.3.3. The uncertainty in the platform positions produces errors in the LUT. Therefore, an extra step to refine the LUT may be needed. The refinement process is performed using the following steps (Wegmüller and Werner, 2011):

- The primary LUT is used to simulate the SAR image from the DEM.
- Cross-correlation between the original SAR image and the simulated one determines the offsets over several patches.
- The offsets are employed to estimate a polynomial model utilising least squares approach.

If the standard deviation of the polynomial coefficient is below a threshold value, the quality of the LUT can be deemed sufficient and suitable to transform between radar and map coordinates. If the quality of the polynomial fitting is lower than required, the above three steps can be iterated. This procedure can also be used in the co-registration process that is discussed in section 2.3.3.

2.3.6 Atmospheric effects

Although InSAR is becoming an effective tool for geophysical applications and topography mapping, the effect of atmosphere is still the most challenging contamination component of the interferometric phase. SAR images acquired at two different times, separated by more than one-day are exposed to variation in signal delay (Hanssen, 2001). The major part of this delay arises from the lower layers of the atmosphere (the troposphere) while the impact of the ionosphere is a wavelength-dependent and it can affect the long wavelengths systems such as L-band (Goldstein, 1995). The variation in water vapour content during the two passes leads to changes in the refraction index of the medium which the signal propagates through (Doin *et al.*, 2009). A variation of 20% in humidity between two-pass acquisitions results in an a atmospheric error of 10-14 cm in the deformation measurements and error of 80 to 290 m in the DEM derived using an unfavourable geometrical baseline (Zebker *et al.*, 1997). The impact of the troposphere is spatially correlated but it can be random if the time between the two acquisitions is greater than one day (Hanssen, 2001).

The tropospheric effect can be divided into two components: dry and wet. The upper part of the troposphere consists mostly of dry gases. The vertical variations of the air temperature and

pressure on this part cause the first order of the delay. Thus, this delay can vary vertically depending on topography. The other part comes from the random variation in the water vapour content in both the horizontal and vertical directions (Doin *et al.*, 2009). Another classification of tropospheric effects has been introduced by Hanssen (2001) who divided the tropospheric delay into the stratified and the turbulent according to the patterns of gas distribution in the medium. However, the two classifications may overlap given that the stratified component may involve mostly dry gases and only partially water vapour. Whereas the major part of the water vapour can be within the turbulence component. Several studies have been conducted on tropospheric effects (Massonnet and Feigl, 1995; Rosen *et al.*, 1996; Zebker *et al.*, 1997; Fujiwara *et al.*, 1998; Emardson, 2003).

Several approaches have been used to mitigate, if not remove, atmospheric effects on repeat-pass InSAR. Correction procedures can be divided according to the technique and data types used in estimating the correction models. In general, the mitigation of tropospheric effects can be achieved using a statistical approach (Massonnet and Feigl, 1995; Ferretti *et al.*, 2001; Crosetto, 2002; Li, 2003) or by using an external data source (Li, 2005a; Li *et al.*, 2006a; Li *et al.*, 2006b; Onn and Zebker, 2006; Yu *et al.*, 2017; Yu *et al.*, 2018a). One of the outstanding atmospheric correction tools is the Generic Atmospheric Correction Online Service (GACOS) (Yu *et al.*, 2017) which can separate stratified and turbulent atmospheric effect utilizing the Iterative Tropospheric Decomposition (ITD) model. In general, external data sources and statistical approaches each have advantages and drawbacks depending on the size of the area involved, the topography and the region. According to Hanssen (1998), images acquired in the daytime are more strongly affected by atmospheric heterogeneities.

2.4 InSAR time series analysis

One of the main limitations of InSAR is phase decorrelation, which mainly depends on the scattering properties of ground objects (Zebker and Villasenor, 1992). Other sources of decorrelation have been discussed in Section 2.3.2. One of the solutions to address the effect of decorrelation is the use of time series analysis. In general, two broad categories of InSAR time series are reported in the literature. 1) permanent scatterers (PS) (Ferretti *et al.*, 2001; Ferretti *et al.*, 2005) and 2) small baseline subsets (SBAS) (Berardino *et al.*, 2002; Mora *et al.*, 2002; Li *et al.*, 2009). However, both categories are based on finding a set of coherent pixels which exhibit good coherence for a period spanned by the SAR acquisitions. PS requires persistent scatterers within the resolution cell that dominate the backscattered signal in the entire set of acquisitions (Ferretti *et al.*, 2001; Hooper *et al.*, 2007). In the PS approach, N interferograms can be generated from N+1 acquisition using a single master for all the acquisitions. PS

scatterers have low amplitude dispersion which refers to the ratio between the standard deviation of the amplitude difference and the mean amplitude. However, the existence of such scatterers in the vegetated or temporally decorrelated areas is rare. Hooper *et al.* (2004) presented a new approach to select PS pixels depending on phase characteristics, which can select pixels with low amplitude but having stable phase.

SBAS time series deal with the resolution cells that contain several scatterers, known as distributed scatterers, which show good coherence in several interferograms having a relatively short temporal and perpendicular baseline (Berardino *et al.*, 2002; Li *et al.*, 2009). SBAS has some advantages over PS specifically for the monitoring of man-made structures because of its ability to produce deformation maps with high spatial resolution. High-resolution is crucial for dam monitoring especially when movement is localized or clustered. For dam deformation monitoring, the spatial pattern of the deformation is necessary in order to interpret the dam behaviour, the deformation type and the magnitude of displacement. This can be potentially achieved by InSAR time series. In the following section, the principles of the SBAS time series are discussed in detail.

The SBAS algorithm is based on distributed scatterers (DS) which are defined as the scatterers which exhibit good coherence for a long time but not necessarily for the entire time span of SAR acquisitions. Recently, Wang *et al.* (2018) has applied the SBAS time seies to the ground based SAR (GBSAR) to select the coherent pixels over a whole period of observations. In contrast to the spaceborne radar, temporal decorelation is rare in the GBSAR application due to the short observation time. SBAS combines all of the available acquisitions using multiple reference (master) images. This approach can increase the redundancy of measurements which not only reduces decorrelation but can also be exploited to estimate other noise sources such as DEM error and the atmospheric phase screen (APS). SBAS starts with a set of N+1 SAR acquisitions acquired at times $t_{0,\dots}t_N$ to produce a set of M interferograms with preferred perpendicular and temporal baselines. Utilizing interferograms with short perpendicular baselines and suitable time separations should mitigate temporal and geometrical decorrelations. Each acquisition should at least be connected to another acquisition in the spatial-temporal baseline network. Thus, the number of the interferograms ranges between (N+1)/2 and N(N+1)/2. Neglecting typical noise sources and DEM uncertainties, the interferometric phase for each pixel in a specific interferogram can be written as follows (Berardino *et al.*, 2002):

$$\delta\emptyset_j(r,a) = \emptyset(t_m,r,a) - \emptyset(t_s,r,a) \approx \frac{4\pi}{\lambda}[d(t_s,x,r) - d(t_m,x,r)] \quad (2.20)$$

where $\delta\phi_j$ denotes the interferometric phase in the *j*th interferogram, *r* and *a* refers to the range and azimuth coordinates of the pixel respectively and t_m and t_s are the acquisition epochs for the master and slave images which are used to generate the *j*th interferogram, while $d(t_s,r,c)\ and\ d(t_m,r,c)$ are the accumulative deformations in epochs t_s and t_m, respectively with respect to the reference acquisition t_0. Rewriting equation (2.20) for M interferograms in a matrix form yield:

$$\boldsymbol{A\phi} = \boldsymbol{\delta\phi} \quad (2.21)$$

If the rank of A ≥ N, which means that all the acquisitions are connected in a single subset, the system of M equations in equation (2.21) can be solved for N unknowns using the least squares approach. The unknowns are the cumulative LOS movement $d(t_1, r, c)$ ... $d(t_N, r, c)$, presuming that the deformation at t_0, $d(t_0, r, c)$ is zero.

$$\widehat{\boldsymbol{\phi}} = (\boldsymbol{A^T A})(\boldsymbol{A^T \delta\phi}) \quad (2.22)$$

In cases where the interferogram network is separated into L subsets, A^TA is a singular matrix and the rank of A is N-L+1 (Berardino *et al.*, 2002). Thus, the least squares solution yields an infinite number of solutions. To avoid the singularity of A^TA, an assumption is made that the velocity of displacements between sequenced epochs, $d(t_m,x,r)\ and\ d(t_s,x,r)$, is constant. Thus, the magnitude of displacement is substituted by the velocity as follows.

$$\boldsymbol{v^T} = \left[\boldsymbol{v_1} = \frac{\boldsymbol{\phi_1}}{\boldsymbol{t_1 - t_0}}, \dots, \boldsymbol{v_N} = \frac{\boldsymbol{\phi_N - \phi_{N-1}}}{\boldsymbol{t_N - t_{N-1}}}\right] \quad (2.23)$$

Equation (2.23) transforms the phase in the *jth* interferogram into:

$$\boldsymbol{\delta\phi} = \sum_{\boldsymbol{k=IS_j+1}}^{\boldsymbol{IE_j}} (\boldsymbol{t_k - t_{k-1}})\boldsymbol{v_k}, \qquad \forall \boldsymbol{j} = \boldsymbol{1}, \dots, \boldsymbol{M} \quad (2.24)$$

And this yields the following manipulated system:

$$\boldsymbol{B_i v_i} = \boldsymbol{\delta\phi_i}, \qquad \forall \mathbf{i=1,\dots,k} \quad (2.25)$$

When k is the number of pixels in each interferogram, *B* is the $M \times N$ matrix in which $B(j, k) = t_{k+1} - t_k$ for $IE_j \geq k \geq IS_{j+1}$, ∀j=1,...,M while $B(j, k) = 0$ elsewhere. Now, equation (2.25) can be

solved to determine the velocities between adjacent acquisitions. The pseudoinverse of B, that is B^{+}, can be determined using singular value decomposition (SVD) as follows.

$$\boldsymbol{B = USV^{T}} \textbf{ and } \boldsymbol{B^{+} = VS^{+}U^{t}} \tag{2.26}$$

where S= diag(σ1 … σN-L+1, 0, ….0) and its pseudoinverse S+=diag(1/σ1 … 1/σN-L+1, 0, ….0)

Equation (2.25) can be expressed as:

$$\boldsymbol{\bar{B}\bar{v} = \delta\bar{\phi}} \tag{2.27}$$

Which can be solved as $\hat{v} = B^{+}\delta\emptyset$, so that the accumulated deformation between t_0 and t_i is:

$$\widehat{\emptyset}_{(t_i)} = \sum_{k=1}^{i} (t_k - t_{k-1})\,\hat{v}_k, \forall = 1, \dots, \mathrm{N} \tag{2.28}$$

The SBAS algorithm has witnessed developments in terms of determination of the non-linear deformation component (Lanari *et al.*, 2004b) or to investigate the impact of DEM uncertainties, on the accuracy of the estimated deformation signal (Fattahi and Amelung, 2013). Lanari *et al.* (2007) reviewed the reliability of SBAS in term of large-scale and localized deformation mapping. SBAS is more effective if the scatterers contribute equally across the resolution cell, while PS works more efficiently with a single scatterer dominating the signal of the resolution cell. Furthermore, a combination of the two algorithms can increase the number of pixel candidates, as well as the spatial resolution and the signal-to-noise ratio (Hooper *et al.*, 2012).

The InSAR time series is also capable of addressing the effect of the atmospheric variations. This can be achieved by using statistical approaches (Ferretti *et al.*, 2000; Berardino *et al.*, 2002) or by integrating InSAR with external data sources such as (GNSS) or an auxiliary remote sensing technique (Williams *et al.*, 1998; Li, 2005b; Li, 2005a). Given that atmospheric signals are uncorrelated in time and vary smoothly within a patch of 800 m in space (Hanssen, 2001; Hooper *et al.*, 2007), multi-interferogram techniques firstly introduced by averaging the phase gradients to remove the major part of the tropospheric delay. Sandwell and Price (1998) used an approach to average the phase gradient to partially remove the atmospheric effects. This approach is known as stacking and has been applied in several displacement applications (Strozzi *et al.*, 2000; Wright *et al.*, 2001). Although stacking can mitigate the atmospheric signal significantly, it may hide an important part of the displacement signal.

2.5 Determination of 2D and 3D displacement vectors

Another limitation of InSAR is that the deformation is estimated along the one-dimension of the LOS. In most of the deformation analysis the use of 3D displacement vectors is essential to understand the mechanism and source of the deformation. To derive 3D or at least 2D deformation vectors from InSAR, two or more observations from different viewing angles are required (Fialko *et al.*, 2001; Wright *et al.*, 2004b). Estimating the 3D deformation vector from only one track of SAR images is not possible. If the displacement vector in a specific reference frame such as international terrestrial reference frame (ITRF) is [E N U], then the estimated deformation from InSAR is the projection of this displacement vector to the LOS of the radar.

$$v = E\ \sin\theta \sin\varphi + N\ \sin\theta \cos\varphi + U\ \cos\theta \tag{2.29}$$

where *v* is the magnitude of the deformation along the LOS, E, N and U are the 3D components of the displacement vector in the east, north and upward directions respectively, θ is the radar incident angle, and φ is the azimuth direction of the projection of the LOS onto the horizontal plane. When the number of velocity maps is n and n > 3, equation (2.29) can be written in a matrix form as follows:

$$R = \begin{bmatrix} v1 \\ \vdots \\ vn \end{bmatrix} \qquad U = \begin{bmatrix} E \\ N \\ U \end{bmatrix} \qquad P = \begin{bmatrix} \sin\theta_1 \sin\varphi_1 & \sin\theta_1 \cos\varphi_1 & \cos\theta_1 \\ \vdots & \vdots & \vdots \\ \sin\theta_n \sin\varphi_n & \sin\theta_n \cos\varphi_n & \cos\theta_n \end{bmatrix}$$

The above matrix form can be solved with the least square approach to determine the magnitude of displacement as:

$$U = (P^t W P)^{-1}\ (P^t W R) \tag{2.30}$$

where W is the weight matrix which can be derived from the error maps of the timeseries of each dataset as the inverse of the variance map. The error in the E, N, U component can be estimated from the variance-covariance matrix as follows.

$$\Sigma_{xx} = (P^t \Sigma_{vv} P)^{-1} \tag{2.31}$$

where Σ_{vv} is the inverse of the variances of three line of sight velocities estimated from SBAS time series. The diagonal axis of the Σ_{xx} is the variances of the 3D components: σ_e^2, σ_n^2, σ_u^2.

Chapter 3. Dams in Iraq

This chapter presents a breif history of the water system in Iraq and describes two major dams, the Mosul and Darbandikhan dams, which are the main case studies in this thesis. Iraq has one of the oldest water systems with origins dating back to 705-681 B.C. The two major rivers in Iraq, the Tigris and Euphrates, contributed to the development of the Assyrian and the Sumerians civilizations who settled along the basins of these two rivers. Since that time, dams have played a vital role in the rise and decline of civilisations, especially for people highly dependent on agriculture. An ancient irrigation system in Mesopotamia was developed by the Babylonians and Assyrians as early as 2100 B.C (Jansen, 1983). Two masonry dams have been discovered on the Khosr and Atrush rivers, and the earliest dams were built by the Assyrian king Sennacherib to protect the city of Nineveh (the ancient name of Mosul) (Jansen, 1983). One of the major ancient dams in this area was 240 m long and 3 m high (Jansen, 1983). To the south of Baghdad, the Babylonian king Nebuchadnezzar II also constructed an ancient dam at Abu Habba. Fast forward to the present day and in the last 50 years, seven major dams have been constructed in north and north-east Iraq. The majority of these dames were built on rivers coming from the west of Iran and the south of Turkey (Figure 3.1). Six of these dams are embankment dams. Table 3-1 shows the types of these dams with other specifications of the structure and reservoirs. Most of these were multipurpose dams whose main functions are to regulate water, and providing irrigation, power generation and protection from flood hazards. In addition, the reservoirs of dams such as Dokan and Darbandikhan are considered to be tourist sites.

Dokan was the first concrete dam to be built in Iraq, on the Lesser Zab river and was constructed in 1959 as a cylindrical arch with a crest length of 345 m and a height of 116.5 m (Hassan *et al.*, 2017). The Lesser Zab river is one of the major flows from the Qendeel mountains in the west of Iran into the Tigris river about 80 km south-west of Al-Dibis city. The capacity of the dam's reservoir is 7.250×10^9 cubic metres, 0.700×10^9 cubic metres of which is dead storage (Cordell, 2006; Hassan *et al.*, 2017). The Darbandikhan dam is located on the Diala river which flows from the west of Iran into the Tigris river about 31 km north of Baghdad. It was the first embankment dam to be constructed in Iraq with a height of 128 m and a crest width of 17m. More details of this dam are presented in Section 3.3 and Chapter 5.

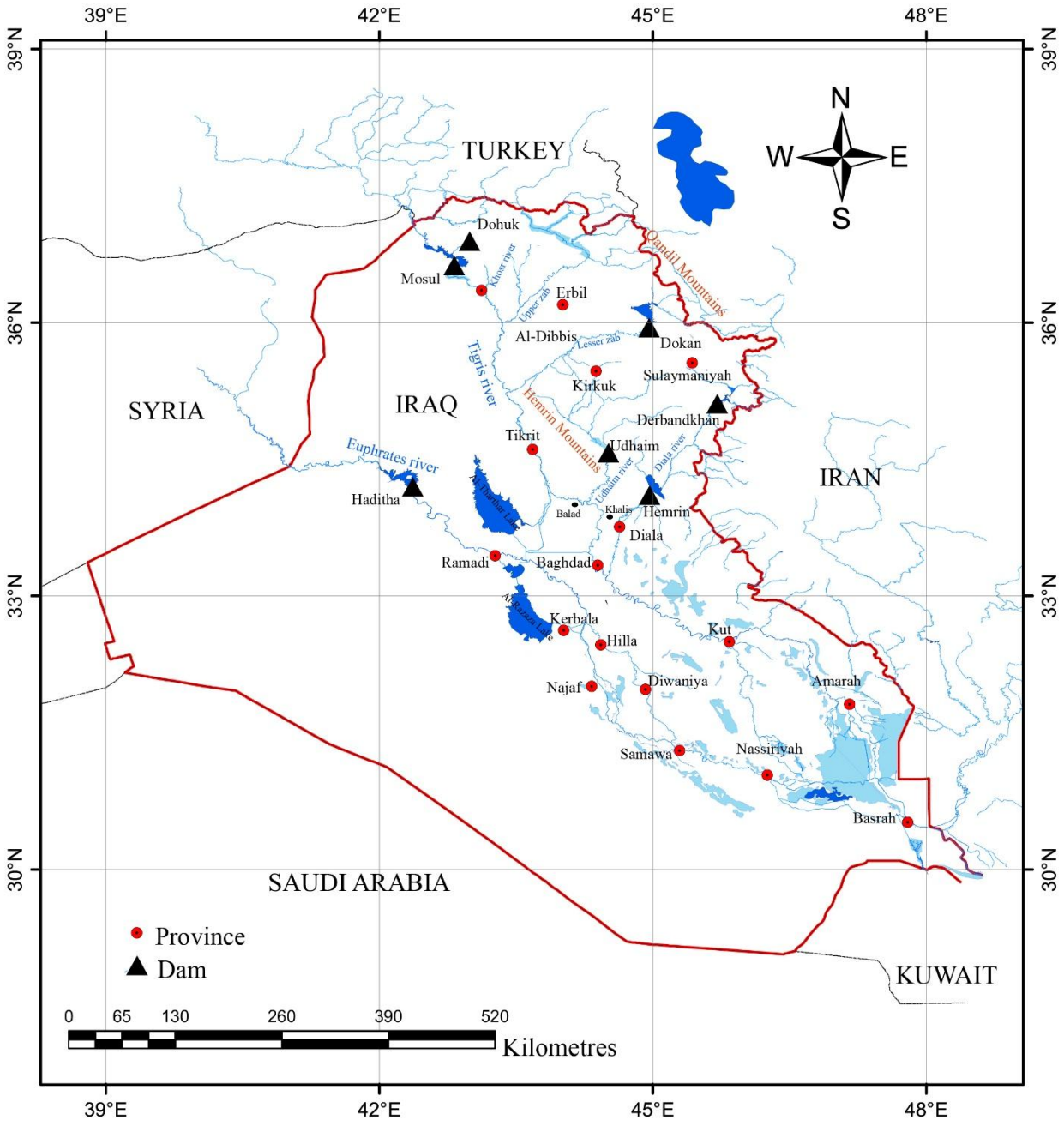

Figure 3.1. The major dams in Iraq (black triangles) and provinces (red circles).

In the 1980s, Iraq adopted a programme to construct additional dams on the Euphrates and Tigress and their tributaries. This program started with building the Himreen dam in 1981 on the Diala river about 120 km north-east of Baghdad. The dam was constructed downstream of Darbandikhan to protect Baghdad from flood risks. It was the first earthfill dam constructed in Iraq with a height of 40 m and a length of 3560 m. In 1985 the Mosul dam, which is the largest in Iraq was built on the Tigris river. The volume of the dam reserve is 11.11 $\times 10^9$ cubic metres and it is used for irrigation and power generation. Nevertheless, the Mosul dam is a most problematic structure because of the existence of soluble gypsum rocks in its foundations. More details about this dam are presented in Section 3.3 and Chapter 4. One year after the construction of the Mosul dam, the Haditha dam was constructed on the Euphrates river, about

7 km to the north-west of Haditha city. The only dam to have been constructed on the Euphrates, it is the site of of the second largest hydropower station operating in Iraq (Shamout and Lahn, 2015). It is an earthfill dam with a length of 8150 m, only 500 m of which crosses the river valley, and it is used for irrigation in addition to power generation. In 1989, the Dohuk dam, which is also an earthfill dam with a clay core, was constructed on the Rowbar river with a height of 60 m and was constructed mainly for irrigation. The last dam in this programme was built on the Udaim river from which the dam took its name, and it is formed by tributaries originating in the Zagros mountains and flows into the Tigris river between Balad and Khalis. The Udaim dam is an earthfill dam constructed on the intersection of the Udaim river with the Himreen mountain range, giving a reservoir of 119 km^2. A few other large dams are under construction, such as the Bakma and Taqtaq dams, in the Kurdistan region, but the political instability and economic crisis have hindered the completion of these dams.

Table 3-1. Specifications of the major dams in Iraq. Dead storage refers to the volume of water when the water level of the reservoir reaches minimum limit. Max and Min stand for maximum and minimum water level of the reservoir with respect to the mean sea level (msl).

Dam	Province	Total Storage $\times 10^9$ (m^3)	Dead Storage $\times 10^9$ (m^3)	Dam Type	Dam Height (m)	Power Generation (MW)	Completion Date	Max Elev. (msl)	Min Elev. (msl)
Haditha	Anbar	10.000	0.240	Earth fill	57	660	1987	150.3	129
Dohuk	Dohuk	0.052	0.004	Earth fill	60	_	1988	618.8	584
Mosul	Nainawa	11.110	3.420	Earth fill	113	750	1985	338.5	300
Dokan	Sulaimaniya	7.250	0.700	Arch	116	400	1959	515	469
Al-Udhaim	SalahAl Dain	3.800	0.500	Earth fill	62	27	1999	143	89
Darbandikhan	Sulaimaniya	4.040	0.470	Rock fill	127	240	1962	493.5	434
Himreen	Diyala	3.560	0.100	Rock fill	40	50	1981	107	92

In addition to the aforementioned dams, 11 other major regulators have been built on the Tigris and Euphrates and their tributaries for water regulation and protection from floods. All these dams and regulators are operated by the Ministry of Water Resources (MOWR) in Iraq. Geodetic monitoring of the structures and embankment of these dams is carried out by the State Commission of Surveying (SCS).

3.1 Topography and climate

As one of the aims of this thesis is to examine the stability of two major dams in Iraq, it is necessary to first address the topography and climate in the study areas. While the topography

and the climate of Iraq are suitable for the construction of dams, chalanges arise due problems with long-term stability of dams once constructed.

In terms of topography, the Kurdistan region on the north of Iraq is a mountainous area bordering Mesopotamia in the east and the Zagros and Taurus mountains in the west. The foothills of these mountains form the fertile plain of the Kurdish highlands. The high mountains of Kurdistan cover 21 % of Iraq total area. The mountains are known for heavy snowfall with a mean precipitation of 1200 mm during winter, while it is dry and warm during summer (Stansfield, 2001). In contrast to the mountainous areas, the plains of Kurdistan have a Mediterranean climate that is rainy in winter and warm and dry in summer. This variation in the regional climate contributed to the formation of aquifers, springs and rivers which flow from the mountainous regions to the fertile plains, turning this region into a good base for agricultural land use. As mentioned in the introduction of this Chapter, the need for dams in this area dates back to 705-681 B.C. The Tigris basin have witnessed several flood events when the raise of the water level in the Tigris river can reach a rate of 300 mm/hour (Jaradat, 2002). Therefore, regulators and dams have been constructed in this region to organise the water supply for irrigation and to protect downstream residential and agricultural areas from flooding.

Iraq is one of the 19 countries that has been most affected by the global climate change in the 20th century (Al-Ansari, 2013). The variations on weather patterns and the harsh weather conditions accompanying climate change increase the risk of dam failures (Tofiq and Guven, 2014; Tofiq and Guven, 2015). It has been shown that a slight variation in climate conditions possibly increases the risk of structural damage to dams (Auld *et al.*, 2006). Accordingly, to overcome the challenges of climate change regarding dam safety, it is necessary to improve dam design specifications, which may lead to economic issues, or to find more rapid and precise inspection procedures (Tofiq and Guven, 2015).

Before investigating the stability of the Mosul and Darbandikhan dams in Chapters 4 and 5 respectively, it is necessary to provide historical information about these two dams in the following sections.

3.2 The Mosul dam

3.2.1 History of the Mosul dam

The Mosul dam is the largest in Iraq and located on the Tigris river between Duhok and Mosul. It is an earthfill dam with a clay core. It was constructed after a long debate and investigation into the site's suitability for the construction of such a huge dam. The geological investigation

was carried out by the Techno-brom Export Company in 1962, followed by another geological study in 1964 carried out by the Foima company (Alabayachi, 2015). The dam's design was carried out by a consortium of Swiss Consultants. Four groups, namely Suiselectra, Motor Columbus, Electrowatt and Societe General pour 1'Industrie, cooperated in this project (Sissakian *et al.*, 2014). Construction work by a consortium of highly experienced international German-Italian contractors started in 1981. The stages of construction were supervised by the Swiss Consultants group and the Yugoslavian Energo-Projekt (Sissakian *et al.*, 2014). The construction was completed in 1985 and the first filling of the reservoir started in June 1986. The seepage of water was noticed immediately and thus a continuous grouting programme recommended by the consultants. Water seepage was mainly noticed in the gallery and both sides of the spillway with a maximum flow of 70 l/s from the left side of the spillway (Kelley *et al.*, 2007).

The dam consists of main embankment, the spillway, a hydropower station and an inspection-gallery (Figure 3.2). The gallery is used for maintenance and the monitoring of the foundation's stability. As shown in Figure 3.3, the old river channel passed through the left abutment of the dam and this could be the reason why this part is highly karstified in this area (Kelley *et al.*, 2007). During construction, the river stream was diverted several times to the east and west sides of the embankment to satisfy the construction needs (Kelley *et al.*, 2007). The vertical section of the river bed in the dam site consists of 20 m of sandy and clayey silt (Sissakian *et al.*, 2014). The geology of the Mosul dam is strongly influenced by its regional geological setting. The topographical slope of the area has a gradient of 50 m/km, which is not the usual topography in which karstification can be found. According to Jassim *et al.* (1997), karstification normally occurs in topographies with gradients less than 35 m/km.

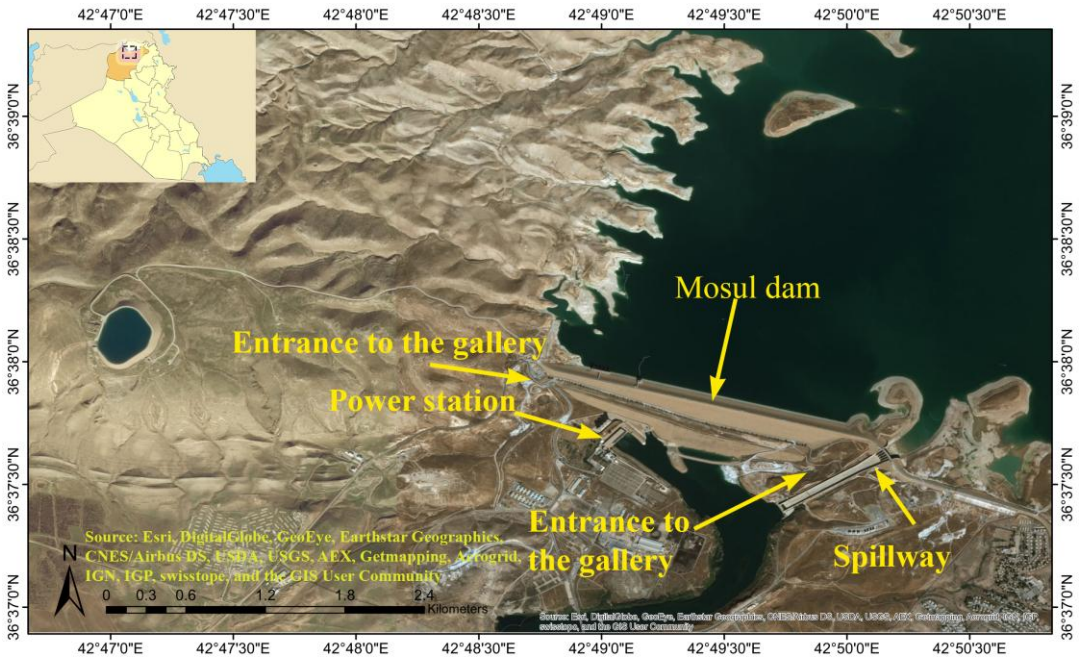

Figure 3.2. Main features of the Mosul dam (background image from Esri DigitalGlobe 2018)).

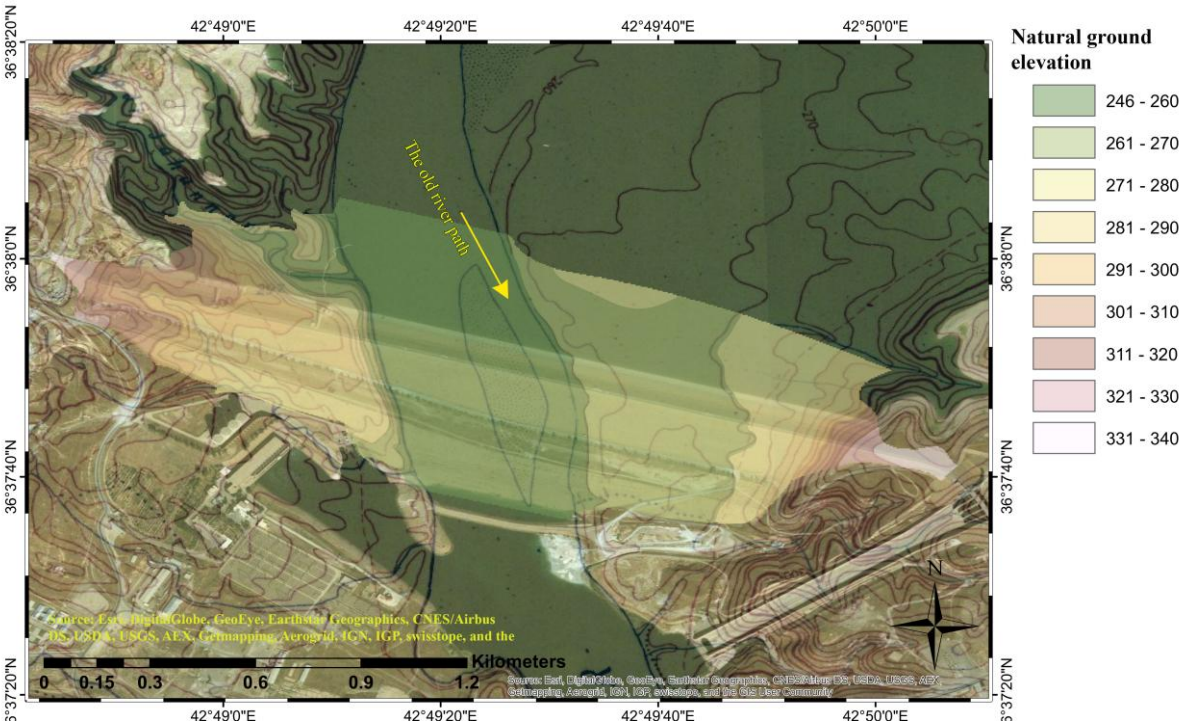

Figure 3.3. Topographical map of the ancient path of the Tigris river at the location of Mosul dam as provided by the SCS. The shaded area is the footprint of the Mosul dam while the colour scale refers to the topography of the area prior to the dam's construction (background image is from Esri DigitalGlobe 2018).

Figure 3.4 illustrates a typical section of the dam embankment. The dam core was constructed from clayey silt layers up to 20 m thick whereas the slopes of the embankment consisted from conglomerate and alluvium materials taken from the river section. According to Charles (1986) puddle clays and granular materials have a similar compaction coefficient ranges between 0.001

and 0.004 and for poorly compacted fill it can reaches 0.007. The compaction coefficient of the Mosul dam puddle core and conglomerate materials are estimated in Chapter 6.

The Mosul dam is located about 60 km north of the city of Mosul, which is the second largest city after Baghdad in Iraq. The concerns over the dam's safety started with the first filling of the lake when water leakage was observed in several parts of the downstream side. It was reported that 6 million people would be affected in the case of dam failure, with two millions of them at risk of 2 m of inundation (Annunziato *et al.*, 2016). Mosul would be the most seriously affected city facing a wave of 25 m height after less than two hours, while the capital Baghdad would be inundated with a 2 m wave after 84 hours (Annunziato *et al.*, 2016).

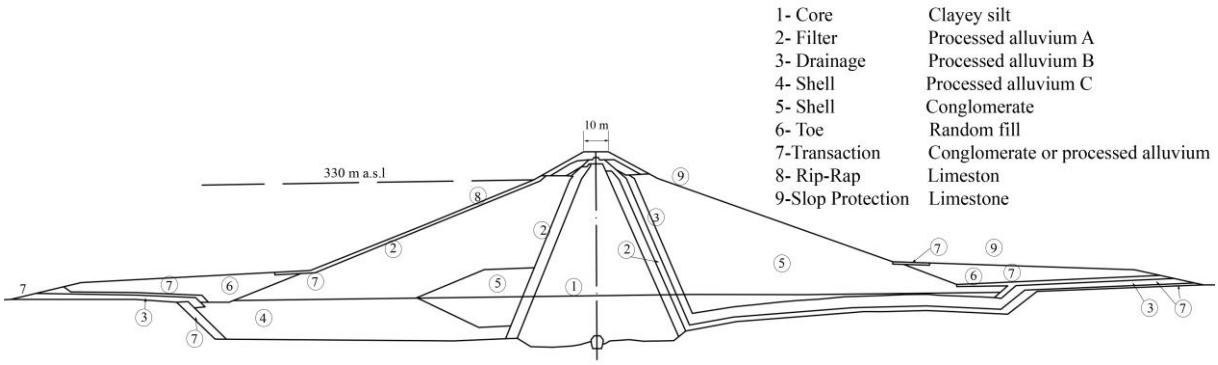

Figure 3.4. Typical embankment section of the Mosul dam showing construction materials.

3.2.2 Geological setting of the Mosul dam

Mosul province is located on the Arabian plate, which was for a long-time part of the continent of the Gondwanan. The geology of the Mosul area generally consists of three settings (Al-Saigh and Al-Dabbagh, 2011). The upper marl series consists of two clayey types: silty clay and marls. The underlying setting is the lower Marl series which mainly consists of clayey marls, limestone and gypsum layers (Salih, 2013). The earliest geological setting is the Jeribe Formation (Early Miocene) which consists of dolomitized limestone, dolostone, sporadic thin gypsum and clayey dolostone. The second unit is the Fatha Formation (Middle Miocene) which is divided into two main layers with varying regional thickness. In the Mosul area, the thickness of the lower layer is about 90 m, and its vertical section from top to bottom consists of limestone, gypsum and carbonate (Jassim *et al.*, 1997). The upper layer consists of gypsum and to less extent carbonate as well as green and red claystone. The upper unit is the Injana formation (Upper Miocene) which consists of fluviatile claystone (Sissakian *et al.*, 2014). In general, 11-15% of Iraqi soil compromises gypsums, forming 7.3-10% of the world's gypsum area (Salih, 2013).

The presence of gypsum rocks under high-pressure fresh water is an enabling factor for the development of voids and karst features. The permeability of water through the fractures accelerates the rate of solubility of gypsum (Thanoon, 1990). The other factors which may contribute to the development of voids are temperature, the hydraulic gradient and the length of water passages for both ground and surface water (Ford, 1988). The solubility rate in streaming water can reach 0.10-0.08 m^3/year, and this can lead to a progressive dissolution of gypsum rocks. Karst features can take four forms, namely: sinkholes; shafts and karren; karst valleys and caves (Jassim *et al.*, 1997). Sinkholes are underground voids formed in gypsum areas with a size reachs 400 m^3 and they have been detected around the Mosul dam in several locations (Kelley *et al.*, 2007; Salih, 2013; Sissakian *et al.*, 2014). The depth and diameter of sinkholes depend on the thickness of the gypsum bed, and whether it is overlaid by limestone (Jassim *et al.*, 1997). Karren and shafts are narrow and deep holes which develop in gypsum areas and they can reach depths of 20 m and widths of 1-2 m, while karst valley is a rectangular drainage path developed on limestone with underlying features. Caves are not known in the Mosul area, but some do exist in Tel Afar (Jassim *et al.*, 1997).

The karstification around Mosul city was investigated by Jassim *et al.* (1997) using aerial photogrammetry. A variety of dissolution features were detected, namely, shafts, karren and sinkholes. It was noted that the sizes of the sinkholes range between 2 and 25 m. The presence of dissolution features was quite clear even during the initial construction phases of the Mosul dam (Kelley *et al.*, 2007). Sinkholes emerged, in early stages of the operation, around the dam site and fissures developed in the foundations. Seven sinkholes were detected to the downstream side with a settlement magnitude of 2-3 m (Bowen, 2007). Additional sinkholes were detected between 2005 and 2006 indicating continuous dissolution taking place in this area. Thus, it was recommended that the dam should be continuously grouted until stability is achieved (Bowen, 2007). However, the grouting works was suspended for an unknown period after the dam site witnessed severe conflict between 7th and 18th August 2014 (King, 2016).

The complex geology of the Mosul area has been discussed in several studies, although most are merely reviews of previous reports presented during the construction stages or afterwards. Kelley *et al.* (2007) published the first detailed report to sum up the available information about the geology of the Mosul dam. Their study provided the first geological cross-section of the dam. Other geological information about the Mosul dam can be found in (Jassim *et al.*, 1997; Jassim *et al.*, 1999). In terms of conventional geodetic monitoring, no previous study has examined the instability of the Mosul dam using in-situ data.

3.3 The Darbandikhan dam

3.3.1 The history of Darbandikhan dam

The Darbandikhan dam was built between 1956 and 1961 at the intersection between the Diala (Sirwan) river and Baranand Dagh anticline (Cordell, 2006; Tofiq and Guven, 2014). The embankment type is a clay core rock-fill with a maximum height above the foundation of 128 m. Figure 3.5b shows a typical cross section of the dam. The gradient of the upstream and downstream slopes is 1:1.75 (V: H) in the upper slope and 1:2 (V:H) in the lower slope, and the length and width of the crest are 535 m and 17 m, respectively. The dam crest connects the road between Sulaimaniya province and Darbandikhan city, which is about 2 km to the west of the dam. The volume of the slope rocks is 5.2×10^6 m^3, and those were taken from the surrounding mountainous area (Cordell, 2006). The volume of the clay core is 1.3×10^6 m^3, covered with filters which are granular material allows the passage of water and prevents the movement of the sediment through the dam body with a volume of 0.6×10^6 m^3. Remedial work was carried out mainly to stabilise a sliding area on the left and right banks of the reservoir (Cordell, 2006). Between 1999 and 2000, the upstream slope was protected by extra riprap which is a layer of rocks placed on the upstream slop to prevent the erosion caused by fluctuation in the reservoir's water level. This remedial work was followed by another efforts to support the slope in 2006 (Cordell, 2006). Between 1983 and 1985, a new 249 MW power station was installed on the dam toe to replace a smaller one. The water flow to the turbines is controlled by an intake that has three vertical gates, each with dimensions of 4.75 m × 9.50 m (Figure 3.5c). A spillway was constructed on the western abutment to control the water level in emergencies. The elevation of the spillway ogee is 470 m, allowing a discharge of 5700 m^3/s to 11400 m^3/s when the reservoir water level varies between 485.00 and 493.50 m, respectively (Cordell, 2006; Tofiq and Guven, 2014). The grouting and inspection gallery is divided into two parts separated by 75 m of the dam that is not penetrated by the gallery. The right gallery runs from a point under the spillway head and ends 175 m from the right abutment at an elevation of 366 m. The left bank gallery extends for 250 m starting from the left abutment and ending at an elevation of 373 m (Cordell, 2006).

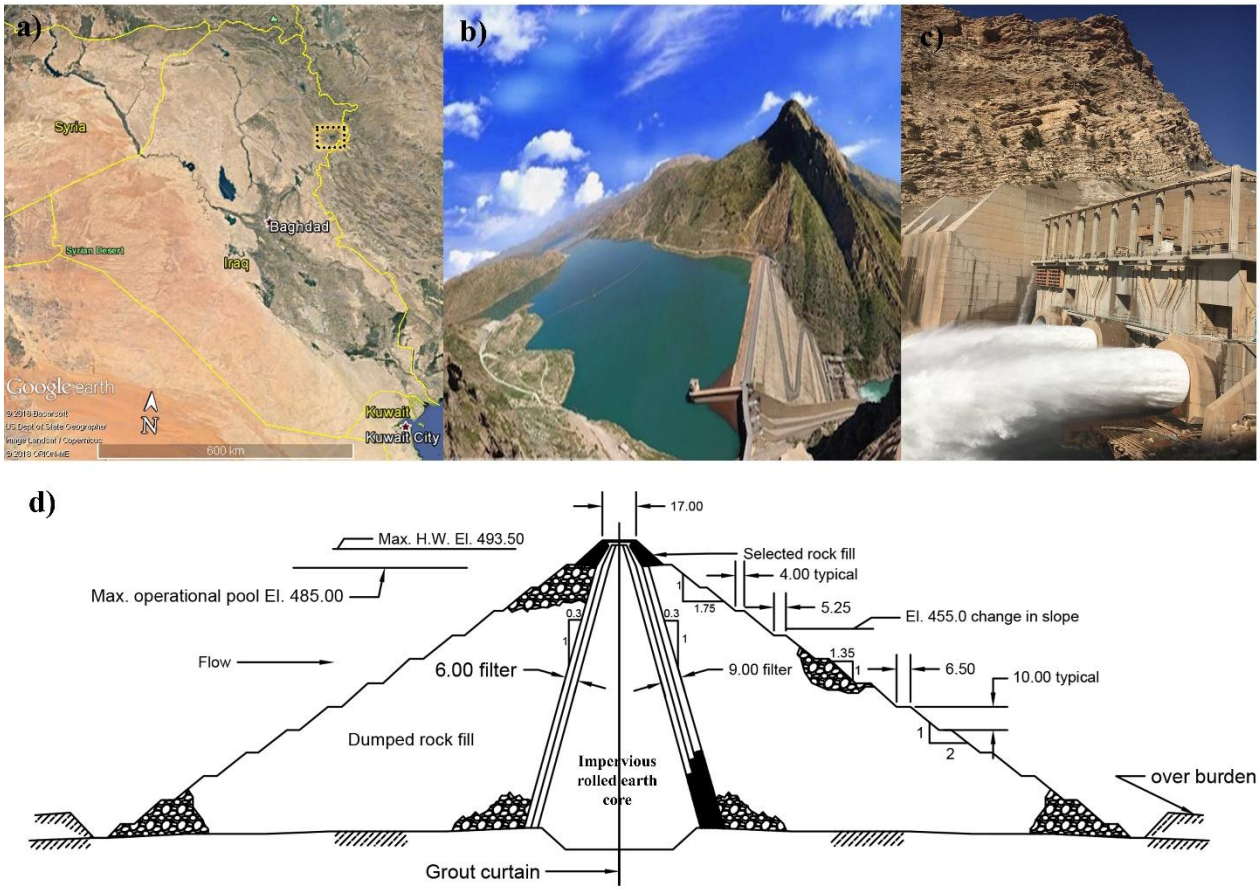

Figure 3.5 a) The location of Darbandikhan dam indicated on satellite image from Google earth, b) overview to the dam site from http://www.rudaw.net/english/kurdistan/03122013 , c) the hydropower station of the dam from https://twitter.com/WorldBankMENA?lang=en and d) a typical cross section of the dam.

The design of the dam was carried out by the American Harza engineering company (Tofiq and Guven, 2015) while the investigation drilling was accomplished by the Britain Cementation and the French Sondages Injections Forages companies. Several contractors and sub-contractors from the USA, Germany and Austria collaborated in constructing the dam embankment. The reservoir capacity is 3×10^9 m^3 when the water level is 485 m and; covers an area of 133 km^2; whereas the live storage capacity is 2.5×10^9 m^3. The minimum drawdown water level is 434 m; which allows for a dead storage volume of 0.5×10^9 m^3. The reservoir has been exposed to rockslides on more than one occasion. Therefore, a high water level is maintained to prevent any potential slides which could lead to overtopping (Al-Ansari and Knutsson, 2011).

3.3.2 Geological setting of the Darbandikhan dam

Darbandikhan dam is located 230 km to the north-east of Baghdad and 65 km south-east of Sulaimaniyah province (45°51'23.512"E 34°27'10.021"N), see Figure 3.5a. Its location was selected to span the gorge formed by the intersection of the Daila river and Branand Dagh anticline. Four main geological units can be found in the area: Qarah Chauq Limestone, Green

Marl Formation, Buff Formation and Bituminous Marl Formation. The dam's foundation is based on the latter two strata (Cordell, 2006). The dam is located close to the collision between the Arabian and Eurasian tectonic plates in the Zagros collision zone (Sadeghi and Yassaghi, 2016). According to Binnie and Partners (1987), the dam was designed to be safe during earthquakes with a maximum Mw of 6.5. The reservoir is surrounded by mountains which have witnessed several landslides and rockfall events. It is fed by two rivers, the Diala in the east and Tanjero in the north.

On 12 November 2017, an earthquake with a magnitude of Mw 7.3 struck the border region between Iraq and Iran with an epicentre located about 30 km from the Darbandikhan dam. The destruction in the nearby cities on both the Iranian and Iraqi sides was extensive. This event is the strongest to have occurred in this region. The embankment of Darbandikhan dam was seriously affected by shaking and rockfall from the surrounding mountains. The deformation of the embankment is obvious, and several cracks on the dam crest emerged. These cracks are critical to slope failure should another earthquake take place in the future because they require less energy to contribute to the slope failure (Utili and Abd, 2016). In Chapter 5 of this thesis, the stability of the dam is examined using three independent datasets: GPS, levelling and Sentinel-1A/B.

3.4 Summary

This chapter presents a brief summary of historical information of the water system in Iraq and described the dams studied in this thesis. Furthermore, historical information is provided about the major dams in Iraq and the geological setting of the Mosul and Darbandikhan dams. A brief background of the water systems in Iraq is followed by descriptions of the major dams and their locations. Topography and climate of Kurdistan, and how these factors contribute to the dam's construction purpose and stability challenges is also discussed. As the evaluation of the stability of Mosul and Darbandikhan dam is one of the major aims of this thesis, the construction history, geological setting and main issues for each dam are detailed. Also, construction information and historical remedial work at both dams are summarised. The problematic geology of the Mosul dam foundation is explained along with the development of the karstification in the area. Finally, history of Darbandikhan dam and its geological setting are described. The information summarized here is crucial to understand the background of these dams before studying their instability in the following chapters.

Chapter 4. Mosul Dam Instability Revealed from Multiple Geodetic Data

4.1 Introduction

Embankment dams are subject to different types of load depending on the geology of the site and the construction materials and specifications (Berga, 1998). Loads on an embankment dams mainly arise from the embankment self-weight and the reservoir water pressure (Johnston *et al.*, 1990). Consequently, embankment may be deformed with different patterns and magnitudes. Furthermore, pore water pressure may be compromised due to a weakness in the construction materials or the instability of the dam's foundation which are the main reasons for the potential failure of a dam. Deformation can occur in the dam's crest, foundation or slopes. The early detection of deformation and identification of its cause is crucial for dam safety. Several dam failure events in history were catastrophic and resulted in huge loss of lives and properties. One of the worst disasters in the history occurred when the St. Francis dam in California collapsed (Rogers, 1995). The most recent catastrophic event was the collapse of a dam under construction in Laos on 23 July 2018, when thousands of people were left homeless with hundreds of lives lost (BBC News Asia, 2018).

The monitoring of dam behaviours during construction and surveillance are crucial and controlled by legislation in many countries (Berga, 1998). The investigation of dam stability can be carried out with instruments or visually. Large, rapidly developing deformations such as those caused by earthquakes, can easily be detected, while the slow deformation that results from the dissolution of material requires continuous monitoring. Instruments are used to observe the measurable quantities such as surface displacements, foundation subsidence, water seepage, hydraulic pressure and the quantity of leaked water whereas visual inspection can help to detect cracking or seepage at the early stages.

InSAR has been approved as an effective tool for large-scale deformation mapping such as in mining (Alex *et al.*, 2011; Li *et al.*, 2015), oil and gas extraction (Blom *et al.*, 1999; Khakim *et al.*, 2013; Liu *et al.*, 2015), water pumping (Lanari *et al.*, 2004a; Bozzano *et al.*, 2015) and tunnelling. Moreover, it has been widely utilised for estimating the pre- co- and inter-seismic and volcanic deformation (Rosen *et al.*, 1996; Beauducel *et al.*, 2000; Hooper *et al.*, 2004; Spaans and Hooper, 2016). The millimetre level accuracy achieved by InSAR and the high temporal accuracy of the new SAR constellations has motivated researchers to evaluate the effectiveness of monitoring the stability of dams using InSAR techniques (Blom *et al.*, 1999; Tarchi *et al.*, 1999; Usai and Klees, 1999; Vöge *et al.*, 2011; Wang *et al.*, 2011; Wang and

Perissin, 2012; Lazecky *et al.*, 2013; Tomás *et al.*, 2013; Di Martire *et al.*, 2014; Sousa *et al.*, 2014; Anghel *et al.*, 2016; Milillo *et al.*, 2016a; Milillo *et al.*, 2016b; Emadali *et al.*, 2017; Milillo *et al.*, 2017; Raventós and Marcos, 2017). The major advantages of InSAR over conventional monitoring techniques are its low cost, high resolution and the ability to work in all weather conditions during the day and night. However, there are a few drawbacks which may affect this ability. Firstly, the deformation can be estimated only in one dimension along the line of site (LOS), and secondly there is low sensitivity to the north-south movement in contrast to up-down and east-west movement (Wright *et al.*, 2004b). Furthermore, when used at embankment dams, the imaging geometry can cause distortions, such as layover and foreshortening, that may hinder proper monitoring (Cigna *et al.*, 2014; Emadali *et al.*, 2017). Nonetheless, InSAR can be utilised to assess the previous behaviour of structures which have not been investigated using conventional geodetic approaches if SAR images are available. InSAR can also be used in disasters to evaluating inaccessible sites rapidly. Therefore, InSAR can be considered as a complementry approach even if not an alternative to other monitoring techniques.

Mosul dam is the largest embankment dam in Iraq. It suffers from geological issues that lead to the risk of a catastrophic scenario at any moment (Bowen, 2007; Annunziato *et al.*, 2016; Milillo *et al.*, 2016a). The geological issues with this dam have been discussed in Chapter 3. It is obstructing about 11.11×10^9 cubic metres of water from rushing down towards Mosul and ultimately southward to Baghdad. The dam was built in 1985 for the purpose of irrigation and power generation. The majority of previous studies have focused on the geological setting of the dam foundation and the surrounding area using construction reports (Jassim *et al.*, 1997; Jassim *et al.*, 1999; Bowen, 2007; Kelley *et al.*, 2007; Wakeley *et al.*, 2007; Al-Saigh and Al-Dabbagh, 2011; Sissakian *et al.*, 2014; Al-Ansari *et al.*, 2015). The results of these studies suggest that the Mosul area is highly karstified due to the presence of the soluble rocks encountered in this region (Kelley *et al.*, 2007; Salih, 2013). A few other studies have investigated the sedimentary impact on the dam lake (Ezz-Aldeen *et al.*, 2013; Issa, 2013; Issa *et al.*, 2013). It has been revealed that the lake is exposed to high sedimentation rates that reached 17.6 m in the upper part of the lake between 1986 and 2011 (Issa, 2013).

Coffman (2009) utilised Envisat images to analyse the movement of the dam surface using multi-temporal InSAR for the period between 2003 and 2010. According to the results the velocity of vertical displacement on the dam surface is 8 mm/year along the LOS. Milillo *et al.* (2016a) used multi-temporal and multi-platform InSAR to monitor the instability of the dam between 2003 and 2016 using SAR data from Envisat, Sentinel-1 and COSMO-SkyMed. Their

study showed an acceleration of dam displacement after August 2014 when grouting activities were paused for an unknown period after the dam site was captured by the self-proclaimed Islamic State (IS).

This chapter firstly describes the instability of the dam using levelling epochs collected between 1989 and 2017 over 87 BMs on the dam surface. The history of the dam's instability along the dam axes and in the lateral upstream-downstream directions is discussed in detail. Areas with critical instability are indicated precisely by comparing the surface and foundation displacements. Additionally, the relationship between the magnitude of subsidence and variations in the reservoir water level is investigated. Secondly, an InSAR time series analysis is presented. Six tracks, two from Envisat, one from COSMO-SkyMed, one from TerraSAR-X and two from Sentinel-1 are used to monitor the external surface movement of the dam. The velocity of the vertical and horizontal displacements is estimated using 2D InSAR computations. For the time span between 2003 and 2010, ascending and descending Envisat tracks are used while, for the period 2014-2017, three tracks from Sentinel-1 ascending, Sentinel-1 descending and COSMO-SkyMed ascending are used. The agreement between InSAR and the vertical movement from levelling data is presented.

4.2 Datasets

4.2.1 The horizontal monitoring network of the Mosul dam

Mosul dam is provided with two geodetic networks to monitor the stability of the embankment, power station, water intake and spillway. The first network is used for the monitoring of the horizontal movement in the main dam and its surrounding area. The second is used to monitor vertical subsidence in the dam crest, foundation and the other controlling structures such as the guard chamber, power station intake, and spillway. The horizontal network consists of 20 pillars, six of which are fixed on the dam crest and labelled P1 to P6 (see Figure 4.1). Each pillar is fixed along the main axes of the dam with a concrete monument and distributed on almost equal intervals (Figure 4.2b). The other pillars are distributed on the surrounding area of the main dam. The State Commission of Survey (SCS) is one of the Ministry of Water Resources (MOWR) institutes in Iraq, and it is in charge of the geodetic monitoring of the dam. According to the SCS, the main horizontal network consists of two subnets surrounding the area of the dam. These subnets are distributed in two zones surrounding the dam site. The first subnet is monitored every five years using the Iraqi national geodetic network every five years. However, this subnet has been destroyed, but it was being used to monitor the second network closer to the dam site every 2.5-years. This second subnet is the only one that still exists, and it

is used to monitor the six pillars fixed on the dam crest every six months. The survey of the whole network requires the measurements of 154 distances and 214 angles. According to the International Commission on Large Dams ICOLD (2005), the stability of the reference network should be examined using the external network before observing the monitoring pillars. However, this examination has not been performed because the external reference network has been destroyed. Therefore, the horizontal network is not used in this study to avoid any analysis mistakes which can results from the distortion in this network.

Figure 4.1. The horizontal geodetic network of the Mosul dam. The monitoring pillars P1-P6 are monitored using the other reference pillars on the dam site. Background image from (Esri, DigitalGlobe 2018).

4.2.2 The vertical monitoring network of the Mosul dam

The vertical monitoring network consists of 87 pillars arranged in six longitudinal lines parallel to the dam axis (Figure 4.2a). Levelling data for the first line on the upstream side is not available because these pillars are seasonally covered with water, and thus they are not involved in the monitoring plan. The six pillars from the horizontal network on the dam's crest (P1-P6) are additionally involved in precise levelling. All of the benchmarks on the dam are used to assess vertical movement with respect to a reference benchmark fixed on a stable area outside

the dam site. The reference benchmark is known as BM20 and is indicated by a black square in Figure 4.2a. Other pillars are established on the hydraulic power station, the spillway and the guard chamber to monitor the stability of these structures. The benchmarks on the dam crest are fixed with a metal pole inside a concrete box and protected with a metallic cover Figure 4.2d). The benchmarks on the dam slope are established with a concrete monument and are fixed on the compacted rock surface (Figure 4.2c). The pillars are distributed regularly to cover the dam crest and the upstream and downstream slopes. The names of the pillars can be found in Figure 4.3.

Levelling is carried out by a specialist team from the SCS every six months (mostly in June and November each year) (SCS, 2017). The reservoir water level typically reaches its maximum and minimum levels during these two times of year. However, the campaign measurements were cancelled or delayed a few times due to security issues or economic circumstances. Geodetic observations were carried out using an optical level during the period from 2005 to 2012. In recent years, GNSS observations have been collected to evaluate the horizontal instability while an electronic level is utilised for precise levelling. However, GPS data is not available for this study. It is not known exactly in which year the electronic level instead of optical level has been used. The surveying was carried out with closed loops which are shown in Figure 4.2 as one to the upstream benchmarks and the other for the downstream benchmarks on the dam surface. The same procedure and loops are followed during each levelling epoch to guarantee similar monitoring circumstances. The elevation of each BM is adjusted using the least-squares approach to yield the instant elevation for each BM (SCS, 2017). The relative vertical displacement of each BM with respect to the first epoch t_0 is calculated as follow.

$$dV_{bi} = H_b(t_i) - H_b(t_0) \tag{4.1}$$

Were dV_{bi} is the vertical displacement of any BM which occurred between t_i and t_0, and $H_b(t_i)$ is the absolute height of that BM at t_i. The mission of observing the whole network usually takes 10-15 days.

Figure 4.2. The vertical geodetic network of Mosul dam: a) location of BMs on the Mosul dam, where dashed lines refer to the levelling loops which are used in geodetic levelling monitoring. Background image from (Esri, DigitalGlobe 2018), b) monument pillar of the horizontal network, c) BM on the dam slope; d) BM on the dam crest; e) BM on the gallery.

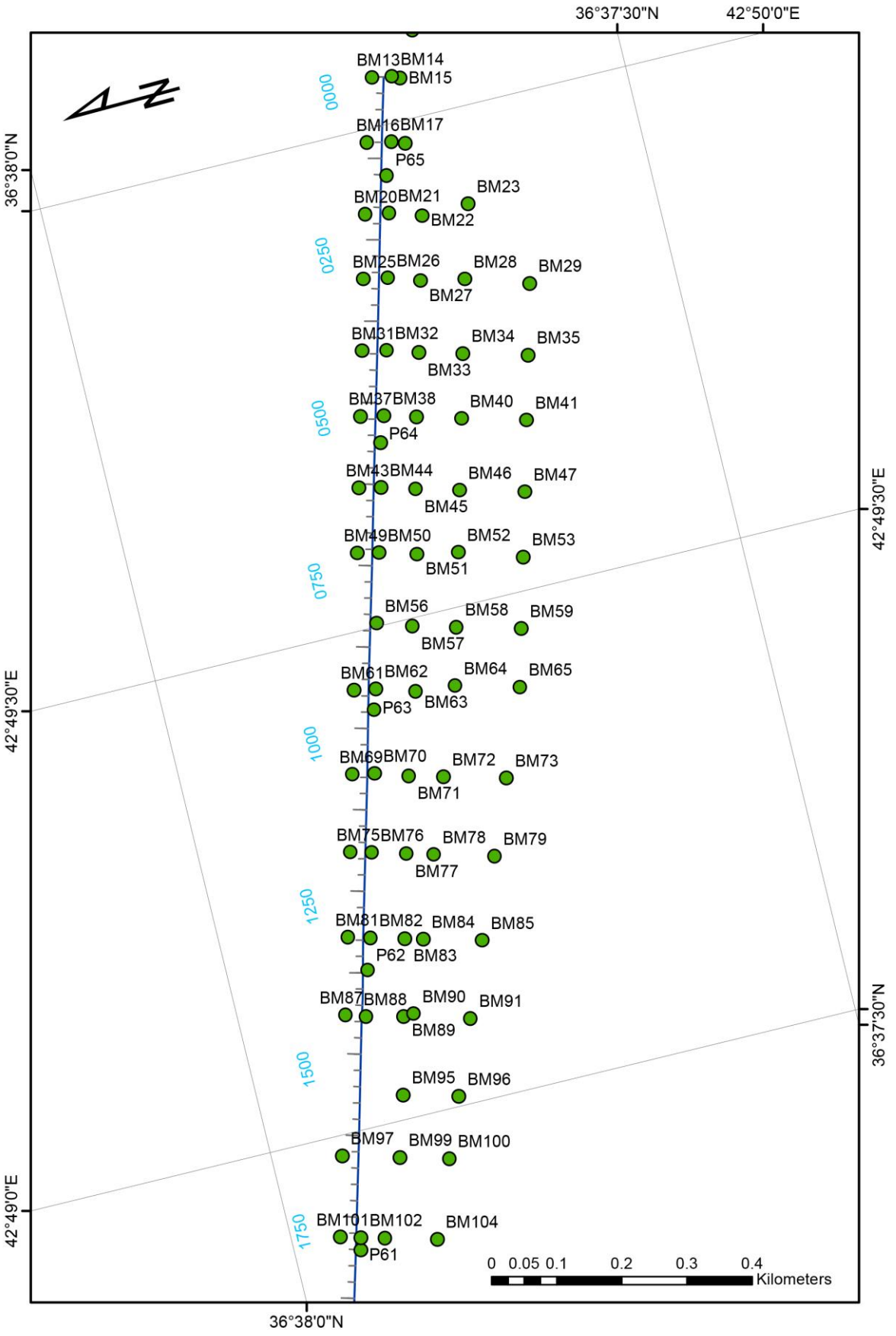

Figure 4.3. Levelling benchmarks of the Mosul dam.

4.2.3 SAR datasets

The InSAR analysis described in this chapter utilises SAR images collected during the span between March 2003 and August 2017 from four different platforms: 1) ESA's Envisat; 2) ESA's Sentinel-1[S1]; 3) the Italian COSMO-SkyMed [CSK]; and 4) the German TerraSAR-X [TSX]). The number of images in each track is shown in Table 4-1. Figure 4.4 illustrates the temporal coverage of each dataset. Both ascending and descending tracks from Envisat and Sentinel-1 are utilised. There are 22 ascending and 24 descending C-band Envisat images, 39 ascending X-band CSK images, 14 descending X-band images from TSX, and 47 ascending and 51 descending C-band Sentinel-1A/B images. Figure 4.5a shows the spatial coverages of the Envisat, CSK and TSX datasets while the Sentinel-1 coverage is shown in Figure 4.5b. As the number of acquisitions and spatial coverage of Sentinel-1 images are huge compared to the other platforms, thanks to the Copernicus Sentinel-1 program for high temporal resolution, the processing of all the Sentinel-1 images would be computationally very expensive during both the differential interferometry and the time series analyses. Accordingly, cropping the image to a small area can reduce the processing time significantly. Nonetheless, if the size of the cropped image segment is quite small, any long wavelength signals from orbital error or atmospheric delay may not be easily observed. Therefore, three bursts of Sentinel-1 images were extracted from the whole datasets to be used in the interferometry processing. The procedure used for extraction is explained in section 4.3.1.

Table 4-1. SAR datasets used in this study

SAR system	**Pass direction**	**Number of images**	**Number of interferograms**	**Time span (from/to)**	
Sentinel-1 A/B	Ascending	47	595	03/10/2014	22/09/2016
	Descending	51	780	04/10/2014	11/09/2016
Envisat	Ascending	22	84	27/03/2003	29/04/2010
	Descending	24	89	12/06/2003	23/09/2010
TerraSAR-X	Descending	14	91	25/05/2015	11/05/2016
COSMO-SkyMed	Ascending	39	288	03/01/2014	18/04/2016

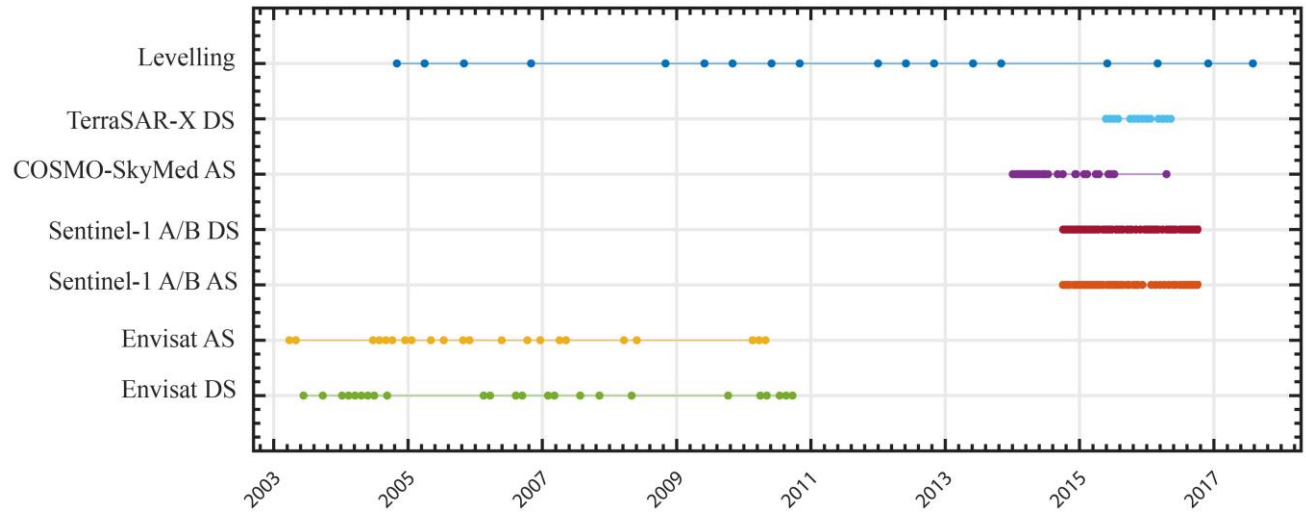

Figure 4.4. Temporal coverage of the SAR images and levelling data used in the Mosul dam study.

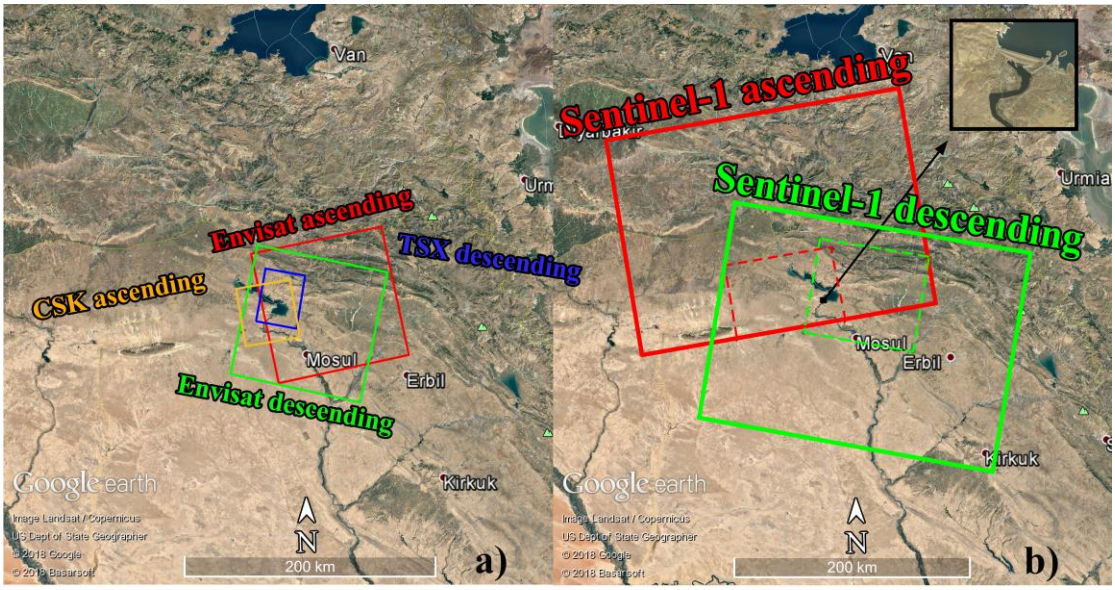

Figure 4.5. Coverage of SAR datasets: a) Envisat, COSMO-SkyMed and TerraSAR-X; b) Sentinel-1 coverage where dashed boxes refer to the coverage of three bursts extracted from the Sentinel-1 scene while the black square in the image subset refers to the area used in time series processing.

4.3 Methods

4.3.1 Sentinel-1 processing

The Sentinel-1 Interferometric Wide Swath (IWS) images are collected in the TOPS acquisition mode (De Zan and Guarnieri, 2006). In this mode, the radar antenna is tilted to the azimuth and range direction so as to achieve a large swath coverage of about 250 km at the cost of along-track spatial resolution. The IWS acquisition consists of three Single Look Complex (SLC) subswaths with a few bursts in each subswath (Figure 4.6). The area of interest can be covered by two or three successive acquisitions. Therefore, a MATLAB script was developed to extract

a subset from each acquisition followed by mosaicking these subsets to generate an SLC image segment covering the area of interest. This was achieved by using a Google Earth kml polygon covering the area of interest (AoI). From each acquisition, only the bursts that are within or intersect with this polygon are extracted from the scene. This process detects the common bursts from two acquisitions automatically and determines the adjacent bursts from two successive acquisitions.

Firstly, a sequence number between 1 and 3 is given to the three subswaths. Also, each burst within the subswath is given a sequenced number between one and the maximum number of bursts in each subswath. This gives each burst a position within the scene represented by a pair of coordinates. The first number of this pair refers to the subswath and the second number refers to the sequenced number of the burst in this subswath. For example, a burst having the coordinates (2,4) is the fourth burst within the second subswath. Hence a subset of the image can be represented by a pair of coordinates referring to the first and last bursts in the image subset. For example, the subset (1,4;3,7) refers to an image segment that includes all the bursts located between the fourth burst in the first subswath and the seventh burst in the third subswath. An auxiliary text file containing the subset coordinates is generated for each acquisition. This file is used then to extract the SLC subset and to mosaic the adjacent acquisitions when the AoI is partially covered by two successive scenes.

Figure 4.6 illustrates an example of the extraction of the area of interest from two successive acquisitions to generate an SLC image segment that fully covers this area. The first subset is (2,1;2,1) representing only the first burst from the second subswath, while the second subset from the second acquisition is (2,8;2,9) representing the 8^{th} and 9^{th} bursts of the second subswath. This approach is merely a technical solution to reduce the time and effort involved investigation of each scene in order to generate an image segment covering the area of interest. One of the Fringe 2017 workshop recommendations was to find a solution to the problem of the different coverage slicing in Sentinel-1 acquisitions (Fringe, 2017). Following this approach overcomes this problem, and the processing time and efforts can be remarkably reduced.

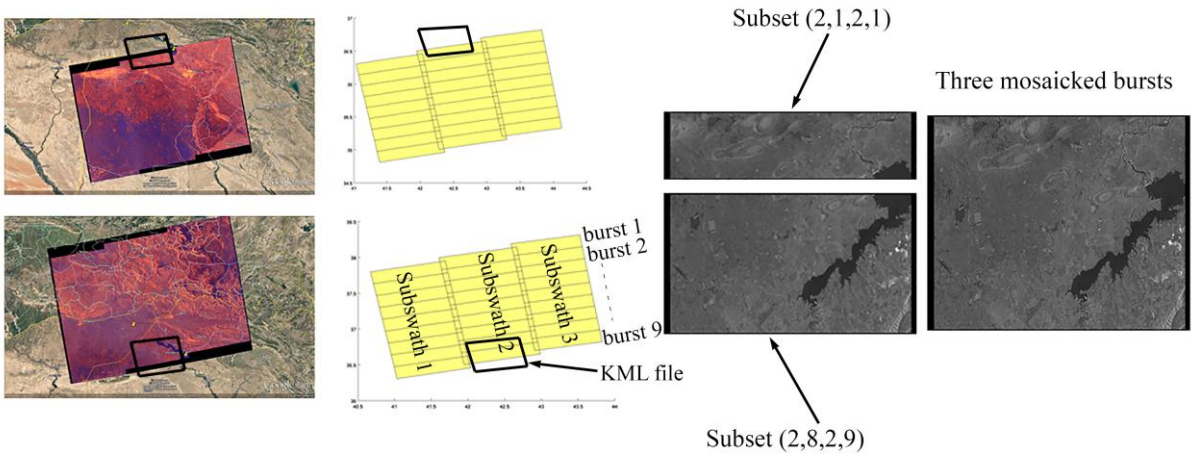

Figure 4.6. Mosaicking two Sentinel-1 adjacent acquisitions to cover the area of interest.

4.3.2 Interferometric processing

Gamma software (Wegmüller and Werner, 1997) was used for interferometry processing. For each dataset, the SLC images were generated in the first step. For Envisat and Sentinel-1 images, the precise orbit vectors were used to eliminate the first order long wavelength orbital error. The Sentinel-1 precise orbit vectors were downloaded from *https://qc.sentinel1.eo.esa.int/aux_poeorb/*, while the Envisat DORIS precise Orbit State Vectors were downloaded from *https://earth.esa.int/web/guest/data-access/browse-data-products/-/article/doris-precise-orbit-state-vectors-1502*. In order to generate an image with an almost squared pixel, Envisat and Sentinel-1 data were multilooked with 1×5 and 5×1 respectively. This multilooking achieves a pixel size of about 20 m × 20 m. The co-registration of each dataset was carried out using the first acquisition as a reference for all other images. Special attention was given to the Sentinel-1 co-registration (Scheiber and Moreira, 2000; Wegmüller *et al.*, 2015), because the conventional co-registration approach is not sufficient due to the phase discontinuity present on the burst overlap along the azimuth direction. This is a consequence of the Doppler shift of the spectrum in TOPS imaging mode. Therefore, the spectral diversity algorithm (Scheiber and Moreira, 2000) was used to enhance the accuracy of co-registration.

Only interferograms with a perpendicular baseline smaller than 400 m were generated in order to mitigate the geometrical decorrelation. The visual inspection of some interferometric pairs with a perpendicular baseline longer than 400 m showed that such pairs are not reliable because of their geometric decorrelation. Another constraint was applied to treat interferometric pairs having a temporal baseline of fewer than 900 days. This choice is supported by evidence that the man-made structures can show good coherence over several years (Usai, 2000; Hanssen and van Leijen, 2008). However, it has been noticed that interferograms with a temporal baseline

longer than 900 days show low coherence over the Mosul dam because of the high phase gradient and temporal decorrelation. Figure 4.7 illustrates the spatial-temporal network of the six SAR tracks used in this chapter. It can be observed that a massive number of interferometric pairs is generated from the Sentinel-1 acquisitions because of the favourable perpendicular and temporal separations. In order to separate the topographical phase component from the other components, a DEM with a spatial resolution of 6 m was generated from a pair of TanDEM-X [TDX] images collected in 2012 and an auxiliary 30 m Shuttle Radar Topography Mission (SRTM) DEM.

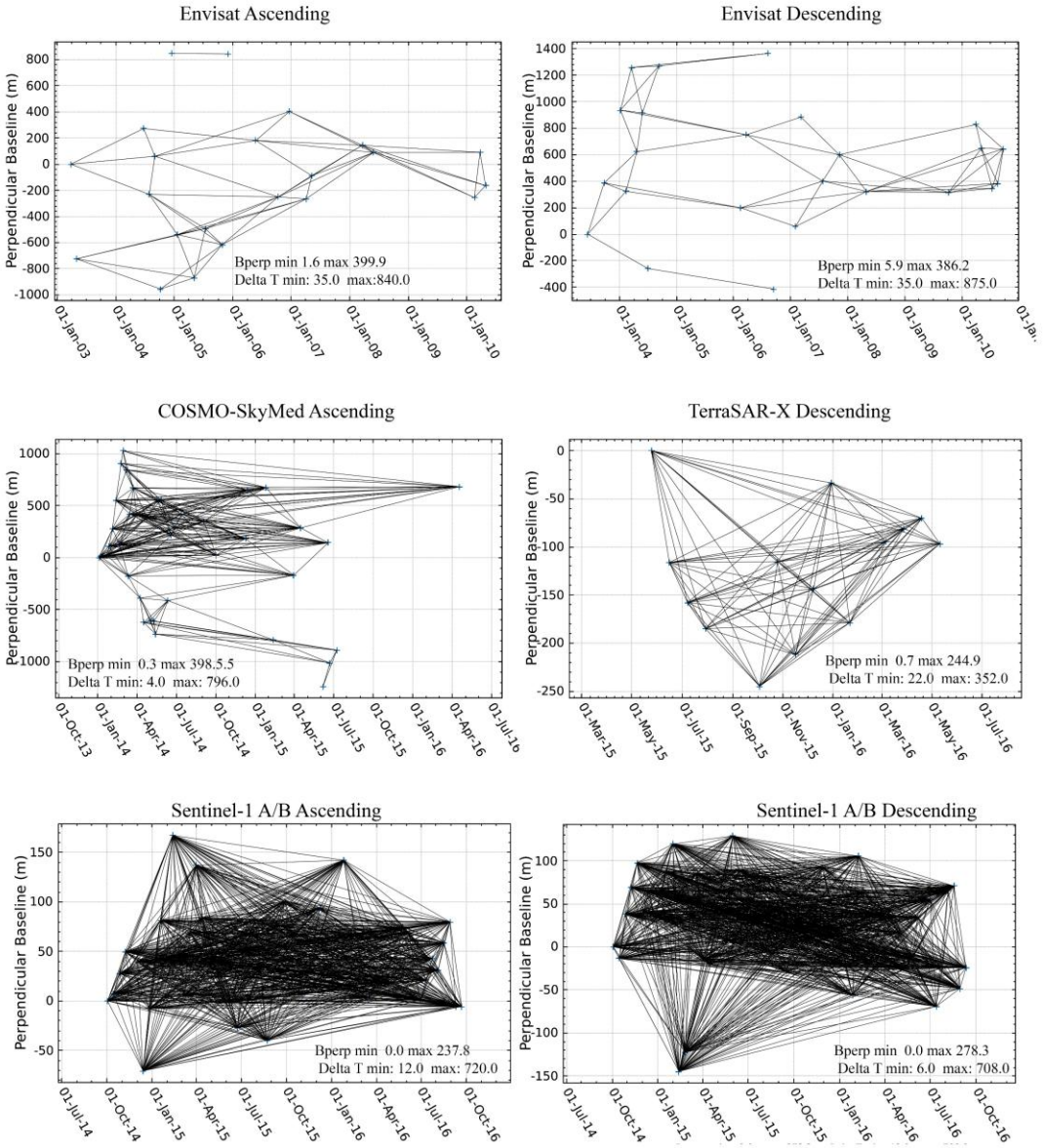

Figure 4.7. Spatial-temporal baseline network for: a) Envisat ascending; b) Envisat descending; c) COSMO-SkyMed ascending; d) TerraSAR-X descending; e) Sentinel-1 ascending; and f) Sentinel-1 descending.

It can be seen from Figure 4.7 that the interferometric pairs from Envisat, CSK and TSX have longer perpendicular baselines compared with Sentinel-1. A long perpendicular baseline leads to a slight difference in viewing angles. As a result, geometrical decorrelation can be significant. In order to reduce this decorrelation in such interferometric pairs, range spectral shift filtering was applied so that only the common spectral band between the master and the slave acquisitions would be considered (Gatelli *et al.*, 1994b). This method can reduce geometrical decorrelation when the spatial separation is relatively long. Since the acquisition mode of Envisat, CSK and TSX images is the StripMap (ST) where the look angle is fixed in the azimuth direction, no azimuth spectral filtering is required. In contrast, Sentinel-1 acquisitions are acquired from small spatial separations. Thus, the ground wavenumber spectra of the master and slave acquisitions can be quite similar and, therefore, no spectral bandpass was applied.

Figure 4.8 shows individual differential interferograms from each dataset in this study. It can be noticed that the 455-day interferogram from Envisat is strongly affected by temporal decorrelation because of the long temporal interval. However, the coherence over the dam site and some other rock surfaces are still sufficient for deformation estimation. The coherence of the other interferograms is functional due to their short time separations. The phase signal in the interferograms is a combination of deformation, atmospheric delays, orbit errors and DEM errors. However, the spatial variability of the signal refers to the domination of the tropospheric signal. This tropospheric signal can mask the deformation signal completely (Zebker *et al.*, 1997; Hanssen, 2001). The separation of the deformation signal from other components is required, and this is discussed in section 4.3.3.

In order to mitigate temporal and geometrical decorrelation, spatial adaptive filtering (Goldstein and Werner, 1998) was applied to the interferograms. This approach should lower phase noise and make phase unwrapping easier. However, the spatial resolution can be reduced slightly. The exponent of the non-linear filtering applied to all datasets was 0.7 with a filtering window of 64 pixels for Envisat and Sentinel-1 data which represent 960 m while for CSK and TSX the filtering window size is 32 pixels which represent 128 m. The window size is a critical parameter, especially for the non-linear localised deformation. The window size must be carefully selected as a trade-off between a reliable estimation of coherence and compatibility with image resolution (Usai and Klees, 1999). Ultimately, the noise in the filtered interferograms is reduced significantly, and this leads to less unwrapping errors.

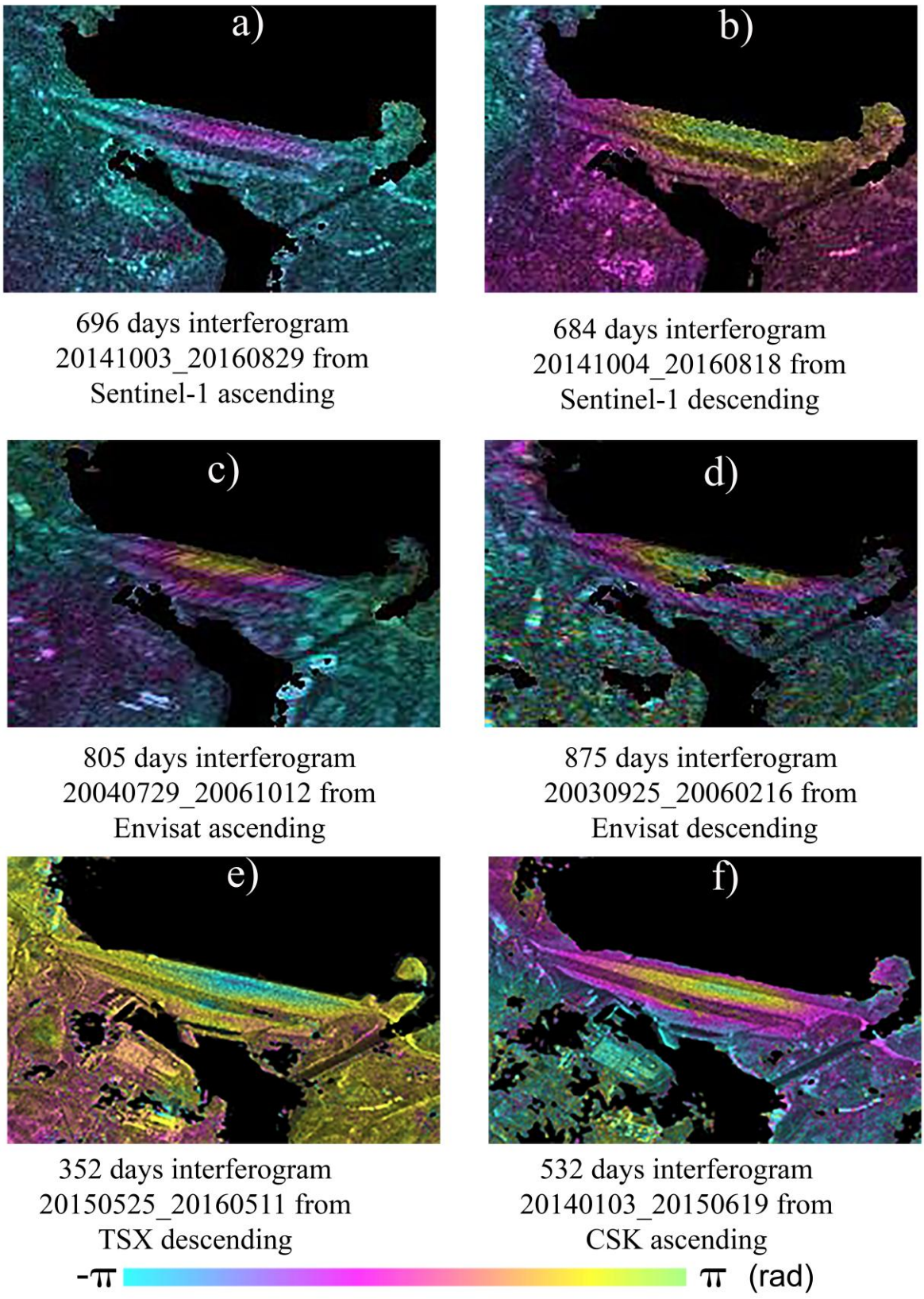

Figure 4.8. Sample interferogram from each dataset used in the Mosul dam study. a) 696 days ascending interferogram from Sentinel-1; b) 684 days descending interferogram from Sentinel-1; c) 805 days ascending interferogram from Envisat; d) 875 days descending interferogram from Envisat; e) 352 days ascending interferogram from CSK; f) 532 days descending interferogram from TSX.

The unwrapping step was carried out using the minimum cost flow (MCF) 2D unwrapping (Costantini, 1998). Given that the phase of each pixel is related to the change in the Satellite-target distance, the unwrapping process should adopt a reference area to guarantee that the unwrapped phase for all pixels is relative to one reference. Accordingly, the levelling reference benchmark BM20 was selected as the centre of the reference area for the unwrapping process. This not only eliminates the phase offset among the individual interferograms, but also to mitigate the displacement offset between the levelling and InSAR. BM20 was installed on what was presumed a relativly stable area of the west side of the dam (Figure 4.2) and close to the dam site, which makes it suitable as an unwrapping reference. Unwrapping errors in some Envisat descending interferograms was quite clear and thus a manual correction of these errors was carried out. The correction was performed on areas showing phase discontinuities by adding 2π for these areas until acceptable phase continuity is achieved. The unwrapped interferograms were then geocoded and cut for a small area covering the Mosul dam site (Figure 4.5). Due to the small scale of the area of interest, the local oscillator decay were not removed from Envisat datasets as this is neglectable for such a localised area (Marinkovic, 2013). The size of the cut area is shown in Figure 4.5b by a black rectangle.

4.3.3 InSAR time series analysis

Surface displacement time series and mean linear velocity were estimated for each datasets using the in-house InSAR TS+AEM software (Li *et al.,* 2009) which is based on the small baseline subset (SBAS) approach (Berardino *et al.,* 2002). The network of differential interferograms was inverted to the phase time series of the acquisition epochs using the least square approach. The constraints adopted in the interferometry processing result in a fully connected network. Given that the tropospheric contribution is corelated in space only and the noise is not corelated with both time and space, a temporary linear velocity (TLV) model is used to estimate the atmospheric phase screen (APS). The process was iterated until divergence achieved. The results of the SBAS approach are the displacement time series, the mean linear velocity, the APS time series and the DEM errors, all estimated along the LOS direction.

A high-resolution TanDEM-X DEM was generated using a pair of images collected in 2012. A coherence masking threshold of 0.7 was selected to mask out the water bodies from the DEM. Thus, in all the interferograms, the signals from the water bodies of the reservoir and the river are completely masked out.

4.3.4 2D and 3D displacement models

To carry out a comparison between the InSAR and levelling displacements, these displacements must be estimated along the same vertical axis. Additionally, they have to be estimated at the same epochs. The time series of InSAR from one side and the time series from the levelling data from the other side were collected in completely different epochs. Furthermore, the InSAR time series was estimated along the LOS direction while the levelling time series was estimated along the vertical direction. Therefore, 2D velocity maps were generated to estimate the vertical (U) and horizontal (H) velocity maps using two or more LOS maps with the assumption that the direction of the horizontal deformation vector is perpendicular to the dam axis. The 2D estimation was used for the interval between 2003 and 2010 as only two tracks from Envisat were available, while three tracks from Sentinel-1 ascending, Sentinel-1 descending and CSK ascending were used for the interval from 2014 to 2017. The 2D computations is derived as follow:

In the 3D computations, east (E), north (N) and up (U) components can be derived by using the following formulas:

$$R = U.P \tag{4.2}$$

where R is the projection of the velocity vector *U* onto the LOS, and P is the unit vector pointing from any target on the ground to the SAR antenna. Accordingly, equation (4.2) can be written as:

$$v = E\ \sin\theta \sin\varphi + N\ \text{sine}\,\theta \cos\varphi + U \cos\theta \tag{4.3}$$

where ν is the velocity along the LOS, E, N and U are the three components of the deformation velocity vector, θ is the incidence angle, and φ is the azimuth of the LOS.

When the number of velocity maps from InSAR is *n* then equation (4.3) can be rewritten in matrix form to be solved as:

$$R_{n\times 1} = \begin{bmatrix} v1 \\ \vdots \\ vn \end{bmatrix} \qquad U_{3\times 1} = \begin{bmatrix} E \\ N \\ U \end{bmatrix}$$

$$P_{n\times 3} = \begin{bmatrix} \text{sine}\,\theta_i \sin\varphi_i & \sin\theta_i \cos\varphi_i & \cos\theta_i \\ \vdots & \vdots & \vdots \\ \text{sine}\,\theta_n \sin\varphi_n & \text{sine}\,\theta_n \cos\varphi_n & \cos\theta_n \end{bmatrix} \wedge\ i{=}1 \ldots n.$$

This matrix form can be solved using the least squares approach:

$$U = (P^t W P)^{-1} (P^t W R) \quad (4.4)$$

The error in the 3D components can be estimated from the variance-covariance matrix Σ_{xx} as follows.

$$\Sigma_{xx} = (P^t \Sigma_{vv} P)^{-1} \quad (4.5)$$

where Σ_{vv} is the inverse of the variances of three line of sight velocities estimated from the SBAS time series. Thus, the diagonal axis of Σ_{xx} is the variances of the 3D components: σ_e^2, σ_n^2, σ_u^2. An important concern should be raised here, as the nearly polar orbit of the SAR system causes a significant reduction in the precision of the N component. In other words, if there is a movement in the downstream direction, it may be inaccurate because the flight direction is almost in the polar orbit (Wright *et al.*, 2004b; Motagh *et al.*, 2017).

In the cases when only two tracks are available, an assumption can be made that the horizontal movement of the dam is dominantly downstream. In other words, zero movement along the dam axis is assumed. However, this assumption may still mis-estimate the lateral movement because the direction of the dam axis is mostly in an east-west direction which may result in reduced sensitivity to the horizontal component. The 2D computations are performed as follows.

If *E* and *N* in equation (4.3) are substituted by the following

$$E = H \sin\lambda \text{ and } N = H \cos\lambda \quad (4.6)$$

where *H* is the horizontal component of the dam movement toward the downstream and perpendicular to the dam axis, and λ is its azimuth, then equation (4.3) can be rewritten as:

$$v = H \sin\lambda \sin\theta \sin\varphi + H \cos\lambda \sin\theta \cos\varphi + U \cos\theta \quad (4.7)$$

In equation (4.7), *H* and *U* can be computed using only two observations from the Envisat ascending and descending datasets. Alternatively, three LOS maps can be used as a redundant observation and the equations solved using the least squares approach. Figure 4.9 shows the geometry of the 2D computations.

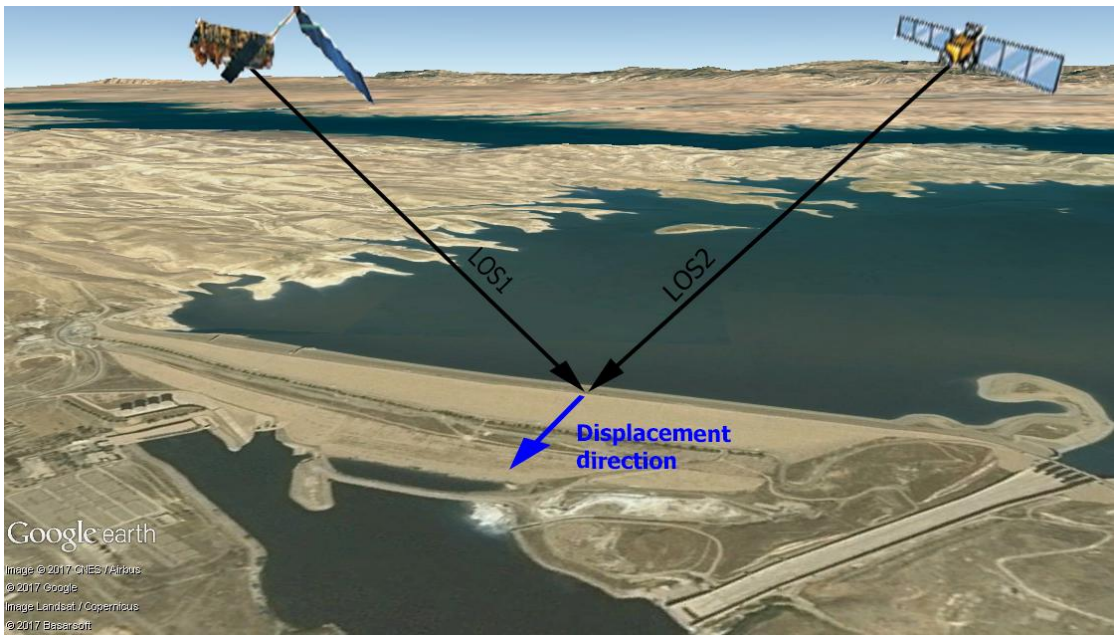

Figure 4.9. Geometry of the 2D computations indicated on a Google earth image.

4.4 Results and discussion

4.4.1 Crest vertical displacement from levelling data

Figure 4.10 shows a comparison of the vertical movement of five cross-sections on the dam crest. The analysis of 21 geodetic monitoring epochs carried out between June 1989 and August 2017 shows that the pillars on the centre of the dam crest exhibited the maximum movement using June 1989 as the reference date, with zero settlement for all benchmarks. The extent of each cross-section is indicated in Figure 4.10f. For discussion purposes, each cross-section is given a name to distinguish it from the others. The names are Upstream, Crest, Downstream1, Downstream2 and Downstram3. The three cross sections on the downstream slope are arranged from top to bottom respectively. The cross-sections are arranged in almost parallel lines with respect to the dam axis in order to compare the settlement of the dam in the lateral direction. In order to mitigate the correlation between the magnitude of the displacement and the height of each BM, the pillars in each cross section were chosen to have almost similar elevations. It is worth mentioning that the elevations of some pillars are missing at specific epochs.

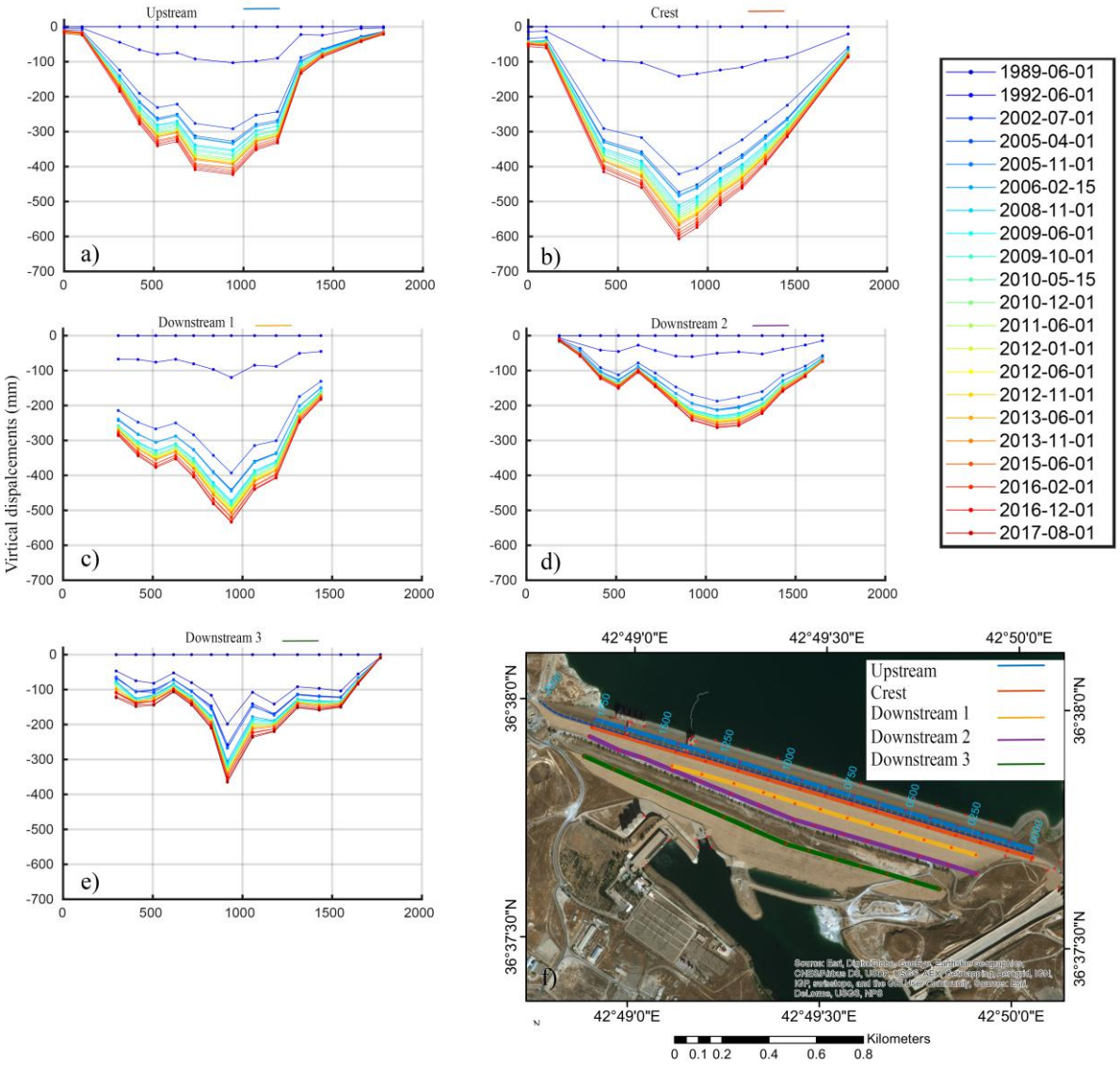

Figure 4.10. The Vertical displacements of the Mosul dam: a-e) on five cross sections on the dam surface between 2005 and 2017. f) the extent of each cross section. The names of the pillars can be found in Figure 4.3.

In Figure 4.10 the maximum settlement in the crest is 610 mm, which is located at 840 m from the reference station on the east abutment of the dam. The average height of the Upstream cross-section is 330 m, which is 15 m higher than the average height of the Downstream1 cross-section. However, the displacements of the Downstream1 cross-section is larger than the displacements in the Upstream1. This may indicate that the downstream slope of the dam has subsided faster than the upstream slope during 1989-2017. The Downstream2 cross-section shows the least displacement compared to other cross-sections, with a maximum settlement of 250 mm. Nonetheless, the area close to station 0+500 has subsided faster than the neighbouring points which are closer to the dam centre, and this is also revealed by the Upstream and Downstream1 cross-sections. The pillar BM56 in the crest is the closest to the centre of the subsidence, having a maximum vertical displacement of 610 mm occurred between 1989 and 2017, while the maximum vertical displacements in the upstream is 420 mm in BM63 for the

same period. In contrast, the maximum vertical displacements in Downstream1 and Downstream2 are 530 and 250 mm as observed in BM63 and BM72 respectively. According to the above analysis, Downstream2 behaves differently in comparison to the other cross-sections. In other words, the maximum displacement of the Upstream, Crest and Downstream1 cross-sections occurs between station 0+839 and station 0+940, while the maximum displacement in Downstream2 occurs in station 1+063. This confirms heterogeneities of the dam behaviour on the Downstream2 cross-section.

4.4.2 Gallery vertical displacement from levelling data

In addition to the analysis of the Mosul dam crest, 150 levelling BMs inside the grouting gallery were utilised to assess the instability of the dam foundation. The levelling was carried out with Zeiss Ni2 and Topcon digital level taking BM20 as a reference benchmark. The standard deviation of the adjusted levels for all BMs was less than ±2 mm. Thus, the expected uncertainty in the estimated displacement between each two epochs is:

$$\sigma_l = \sqrt{\sigma_1 + \sigma_2}$$

where σ_l is the error in displacement, σ_1 and σ_2 are the standard error in the first and second observations respectively, presuming different types of equipment are used in the observations.

Figure 4.11 shows a longitudinal cross-section of the vertical displacement in the dam foundation between June 1989 and August 2017 and a geological section showing the estimated water pressure in the construction time. It can be seen that the maximum displacement in the gallery was 180 mm, that is slightly shifted towards the east abutment of the dam. the subsidence area falls within the maximum water pressure measured in the construction time Nonetheless, there was clear progressive subsidence around the three stations: 0+413, 0+959 and 1+339. This localized subsidence of the dam foundation is an evidence of the potential for failure (Charles, 1986; US Army Corps of Engineers, 2002), because it could lead to a hydraulic fracture and thus development of a seepage path (Almog, 2011). Insufficient grouting could shorten the seepage paths and concentrates the hydraulic pressure in specific zones which could lead to piping in the foundation (ICOLD, 2005). The subsidence of station 0+950 during only four months between June 2009 and October 2009 was 6mm. This rapid displacement is unprecedented during the displacement history of this point. Data on the grouting history was not available in order to allow an investigation of the reason for this rapid displacement.

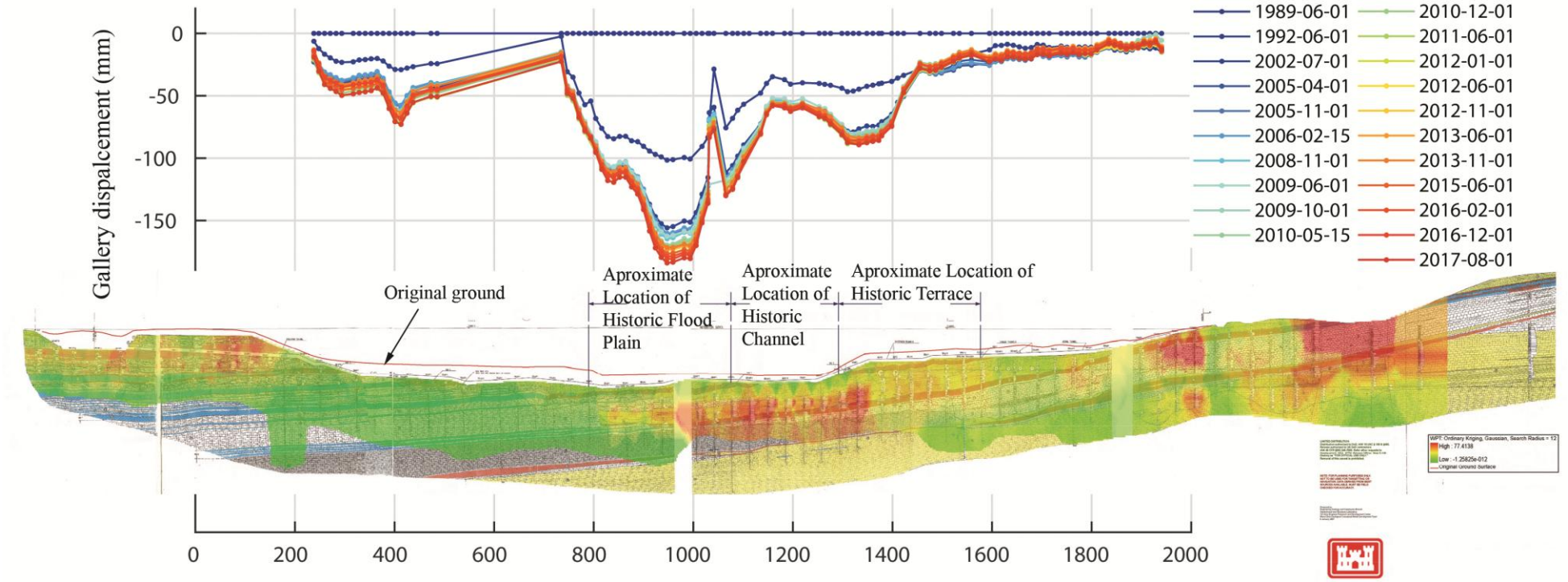

Figure 4.11 Progressive vertical displacement of the Mosul dam foundation measured between June 1989 and August 2017 plotted with geological section of the dam showing the water pressure on the foundation estimated in the construction time (Kelley et al., 2007).

A comparison of Figure 4.10 and Figure 4.11 shows that the displacements at the crest is larger than that of the foundations. This is likely to have occurred because the volume lost at the foundations is substituted by a larger volume from the upper layers due to the large compaction forces on the layers close to the foundation. Hence, this could loosen the compaction on the layers close to the crest and accordingly internal erosion may occur.

Figure 4.12 shows the displacement of the dam foundation at stations 0+413, 0+959 and 1+339 respectively whereas the surface subsidence was discussed in section 4.4.1. Velocity of the displacement where estimated over three periods, 1989-2005, 2005-2014 and 2014-2017. As revealed in section 4.4.2, the displacements rate was fast between 1989 and 2005, slowed down between 2005 and 2013 and reaccelerated after 2014.

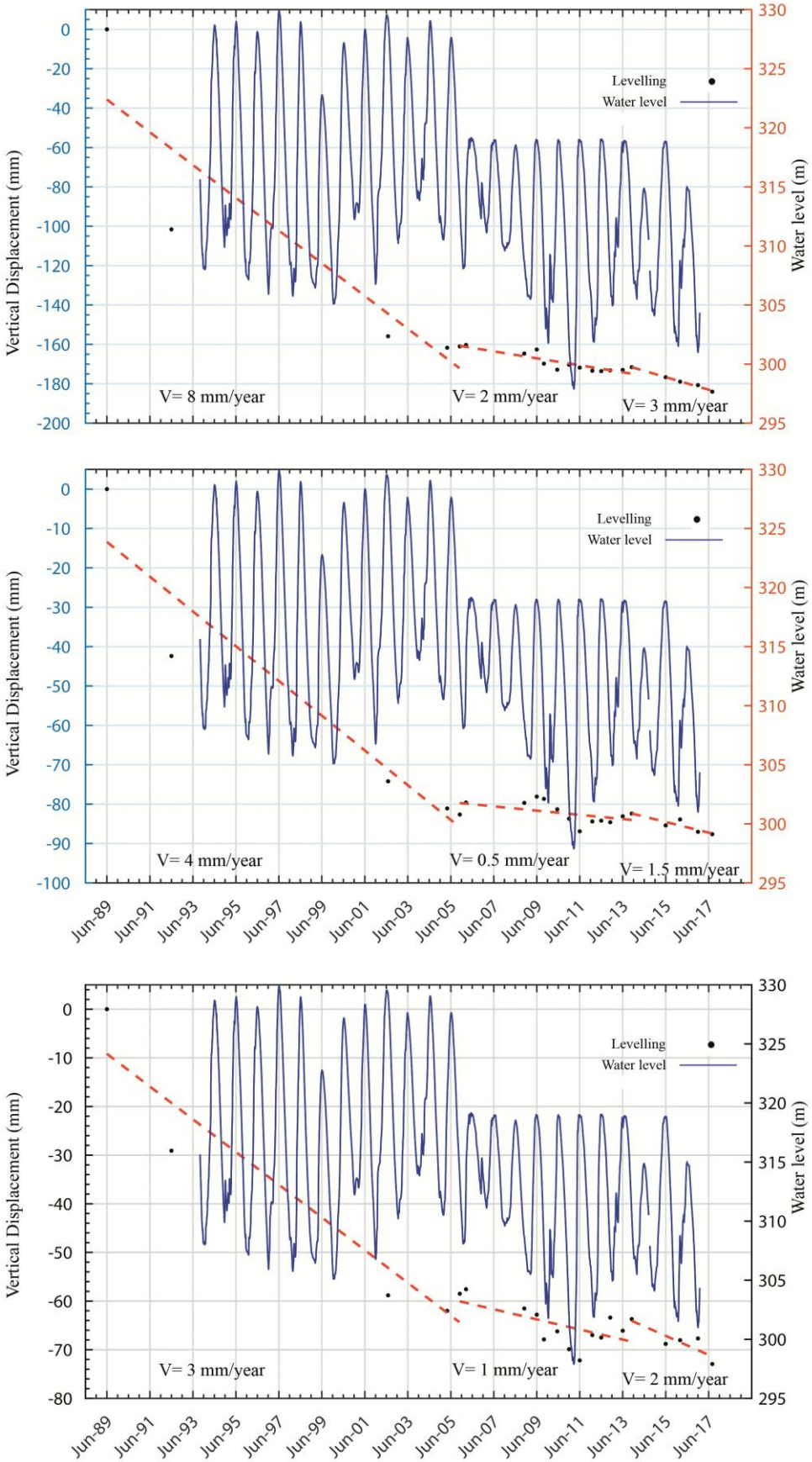

Figure 4.12 Vertical displacement and velocity (V) of three stations in the gallery. a) Station 0+960; b) Station 1+349; and c) Station 0+400.

4.4.3 Correlation between displacements and water level.

Figure 4.13 shows the vertical displacement of the crest on the centre of the area of deformation at two benchmarks, BM56 and BM65 along with the water level time series. The correlation between subsidence velocity estimated over two period, 1989-2005 and 2005-2017. The correlation between the water level and the displacement rate is clear. It can be seen that the velocity of the subsidence was about 29 mm/year between 1989 and 2005 but when the water level lowered to 320 m, the velocity decelerated to 11 mm/year. The same effect of the water level reduction can be seen in Figure 4.13b.

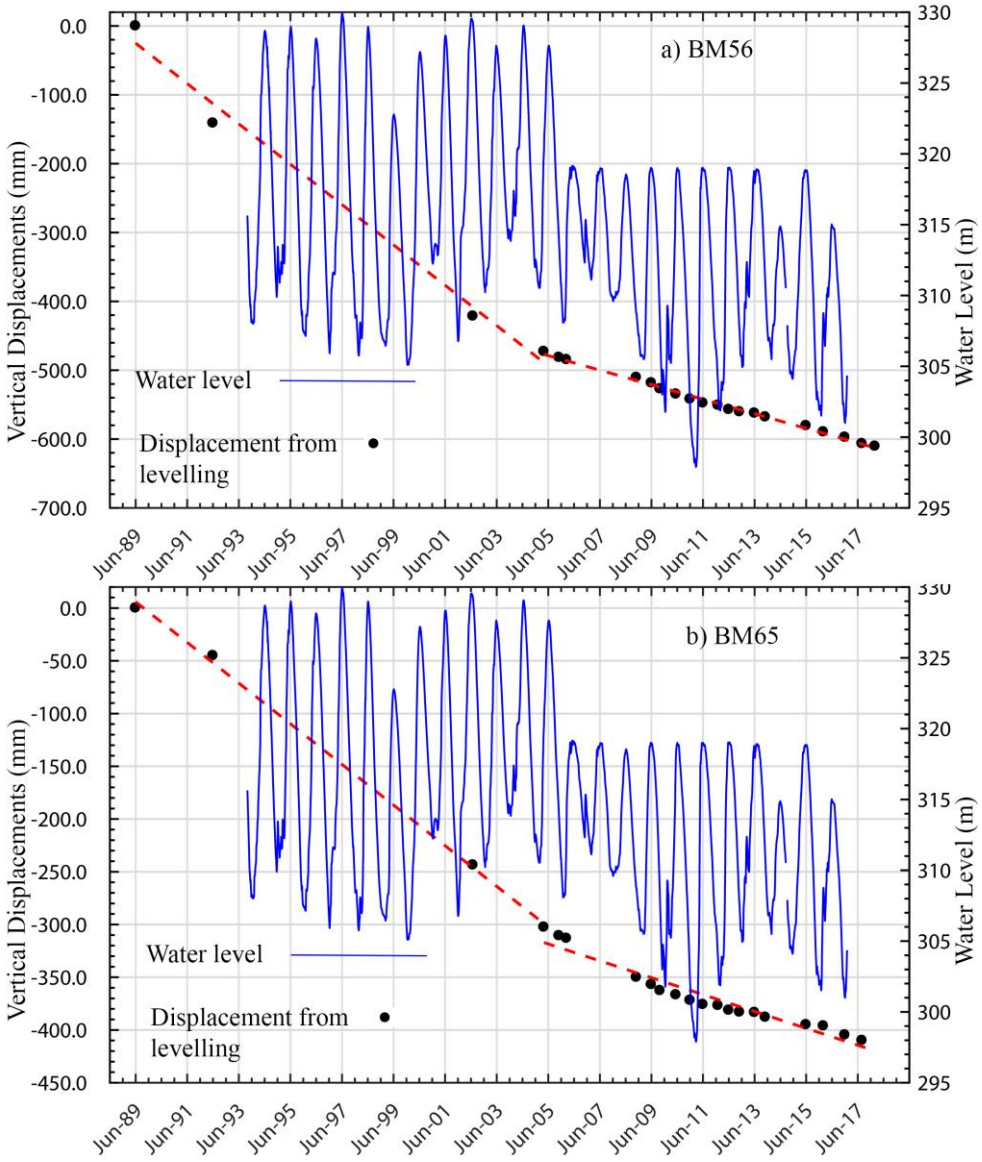

Figure 4.13 Correlation between the water level and the displacement at station 0+840 (centre of the deformation area).

4.4.4 InSAR time series results

Figure 4.14 shows the LOS velocity map for each track of the six SAR datasets used in this study. The pattern of displacement from the six displacement maps is very similar. However, the magnitude of the subsidence differs slightly in the six maps. This is likely to be due to: 1) the different acquisitions geometry of the SAR datasets; and 2) the difference in temporal coverage for each dataset. The displacement maps from Envisat, from the ascending and descending data, show rapid subsidence of 10 mm/year during the period 2003-2010. The disagreement between the ascending and descending maps may occur due to the foreshortening of the dam slope in the ascending images which can under estimate the displacement signal.

The comparison of the six maps shows a rapid displacement between 2003 and 2010 with a deceleration of displacement velocity between 2014 and 2015. Additionally, the TSX map shows an acceleration in displacement between 2015 and 2016. This acceleration is very likely occured after the suspension of grouting operations in August 2014. Rapid displacement at station 0+916 is indicated in Figure 4.14f which agrees with the levelling results at the Downstream3 cross-section. The acceleration of the displacement could take few months before becoming apparent on the dam surface, and thus it can be shown clearly in the data collected a few months after the event and this is achieved by TSX data. Also, it can be seen, in all the velocity maps that the descending data shows a stronger signal than the ascending data due to the imaging geometry and the dam orientation, thus the acceleration can be seen clearly in the descending data.

The displacement maps from Sentinel-1 ascending and descending exhibit better coherence than the Envisat maps. This is due to the higher temporal resolution of the Sentinel-1 acquisitions. Given that the X-band images are more sensitive to the temporal decorrelation, the velocity maps from CSK and TSX show larger masked (incoherent) areas in contrast to Sentinel-1 and Envisat maps because of temporal decorrelation. Moreover, the displacement map from TSX exhibits a more irregular signal because of the short temporal coverage of the TSX acquisitions.

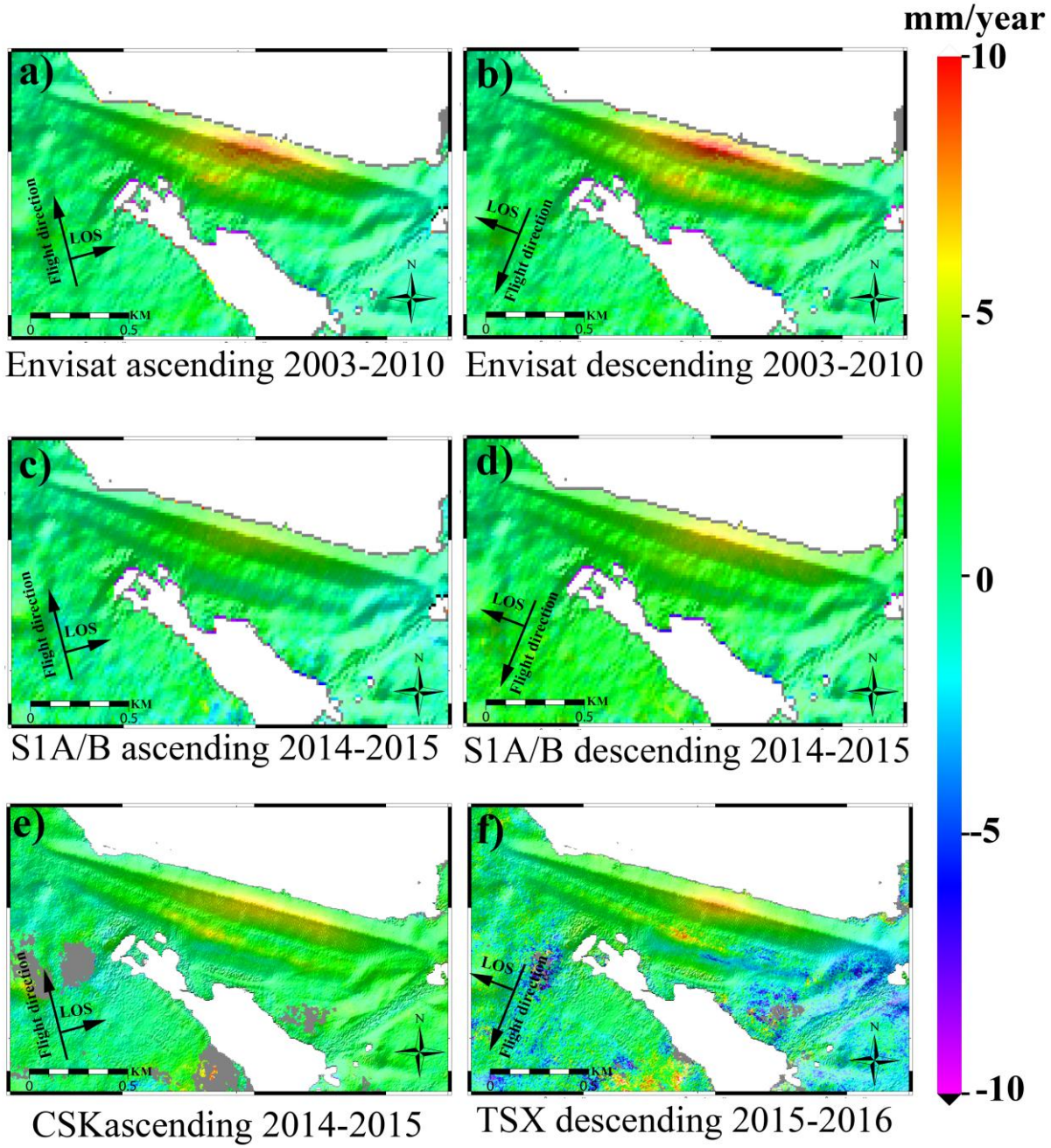

Figure 4.14. LOS velocity maps from six tracks in three different time spans: a) Envisat ascending and b) descending tracks during 2003-2010; c) Sentinel-1 ascending and d) Sentinel-1 descending; e) COSMO-SkyMed ascending during 2014-2015; and f) TerraSAR-X descending during 2015-2016. Note that the map from TerraSAR-X is noisier than the others due to the limited number of TSX images and the short time span.

Figure 4.15 shows the vertical and horizontal velocity maps estimated using the 2D computations discussed in section 4.3.4. Envisat ascending and descending data was used for the period between 2003 and 2010, while Sentinel-1 ascending, Sentinel-1 descending and CSK ascending data was used for the period between 2014 and 2016. The CSK data overlaps with the Sentinel-1 data for 1.5 years between October 2014 and April 2016. The horizontal velocity maps do not show significant horizontal movement between 2014 and 2017, while some noisy signal, can be seen in the 2003-2010 map. If the direction of horizontal movement is assumed

to be downstream (south-west), then such movement could have been partially underestimated (Wright *et al.*, 2004b; Motagh *et al.*, 2017).

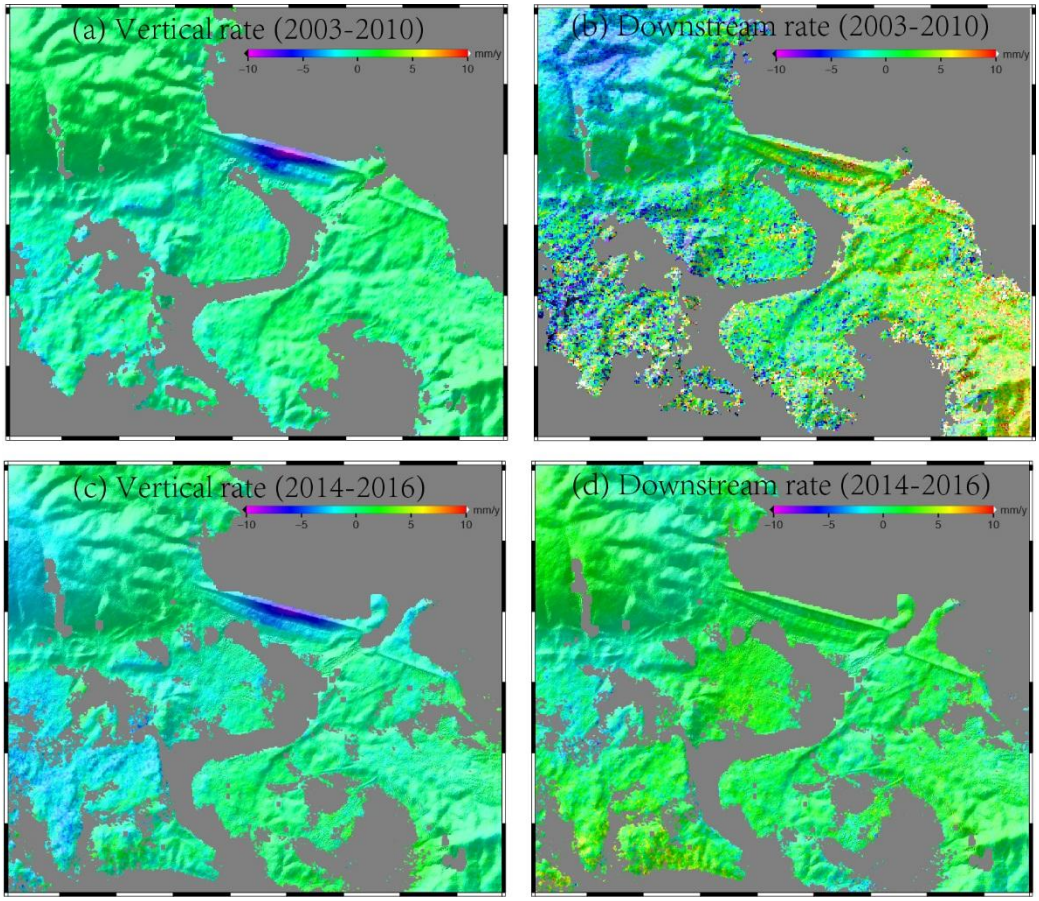

Figure 4.15. 2D deformation maps for two periods, a,b) vertical and horizontal deformation maps from 2003 to 2010 and c,d) vertical and horizontal deformation maps from 2014 to 2016. The first two maps were estimated from Envisat ascending and descending, while c) and d) estimated from Sentinel-1 ascending, Sentinel-1 descending and CSK ascending tracks.

4.4.5 Comparison of InSAR and the levelling dispalcements

In order to validate the InSAR 2D velocity maps, levelling data collected over 87 benchmarks on the dam surface was employed. The average velocity of each benchmark for the span covered with SAR data was estimated and compared to the vertical velocities estimated from the use of InSAR 2D approach. The comparison suggests an RMS of 1.7 mm/year and a correlation of 0.93 between InSAR and levelling data during 2003-2010. In contrast, the RMSE for the difference between InSAR and levelling velocities is 0.88 mm/year during 2014-2017 with a correlation of 0.95. Moreover, difference of velocities between the two techniques during the period 2003-2010 is less than that for the span between 2014 and 2017. This could be caused by the acceleration of the surface displacement between 2014 and 2017.

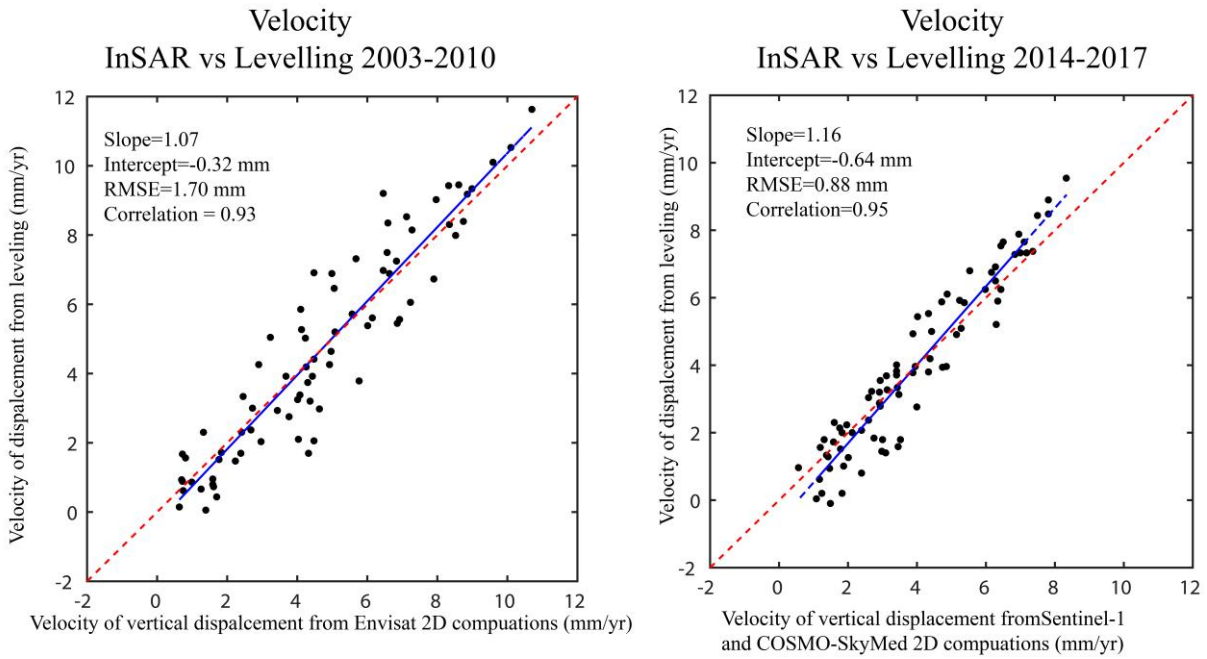

Figure 4.16. Comparison between mean linear velocity from InSAR and levelling using 87 benchmarks on Mosul dam: a) for the period between 2003 and 2010; and b) for the period between 2014 and 2017.

Since the horizontal movement of the Mosul dam embankment is not very significant as was shown in Figure 4.15, the agreement between vertical displacement from levelling data and InSAR timeseries for each track has been examined. The vertical displacement from leveling was projected to the LOS using the incidence angle of each track. Figure 4.17 shows the agreement between levelling and TSX timeseries of six benchmarks on the upstream and downstream slopes for the period between 2015 and 2016. The RMS for the six benchmarks is less than 1 mm.

The comparison between leveling and InSAR timeseries at benchmark located on the center of the deformation (BM56) for each dataset is shown in Figure 4.18. The best agreement is achieved by the CSK and TSX timeseries and this is likely due to the high spatial and temporal resolution of this data. Since Envisat ascending data exposed to high foreshortening factor, timeseries from this dataset shows the largest RMS in contrast to other datasets, i.e., 8.6 mm. Similarly, Sentinel-1 ascending data shows larger RMS in contrast to Sentinel-1 descending for the same reason.

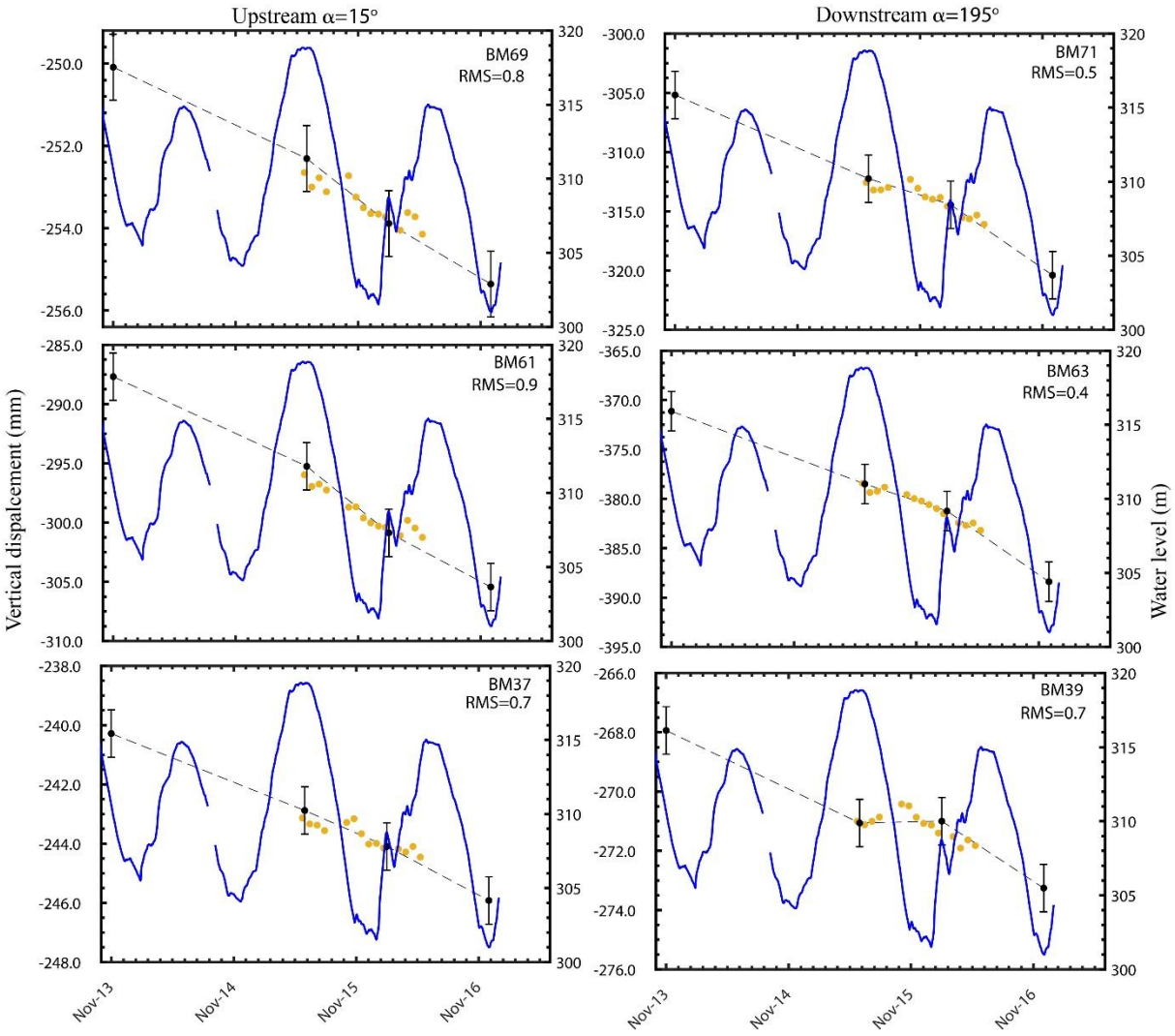

Figure 4.17. Agreement between levelling and TSX timeseries for benchmarks located on the upstream (left) and downstream (right).

The RMS maps for levelling and Envisat ascending and descending timeseries for all benchmarks on the dam surface is shown in Figure 4.19. The RMS for all BMs is less than 8 mm except BM65 which is indicated with red circle. This point is located in a small deformed area (see Figure 4.14f) and thus the RMS between levelling and InSAR is about 20 mm. This large RMS can be due to the high displacement gradient in this area (Emadali *et al.*, 2017).

Table 4-2. Imaging geometry and spatial resolution of SAR images collected over the Mosul dam.

Platform	Heading(deg)	Incidence angle(deg)	Spatial resolution (m)
CSK ascending	-10.34	35.81	5
Envisat ascending	-12.03	19.21	20
Envisat descending	-168.11	24.69	20
TSX descending	-170.51	43.09	3
Sentenel-1 ascending	-13.20	41.02	20
Sentinel-1 descending	-166.89	41.18	20

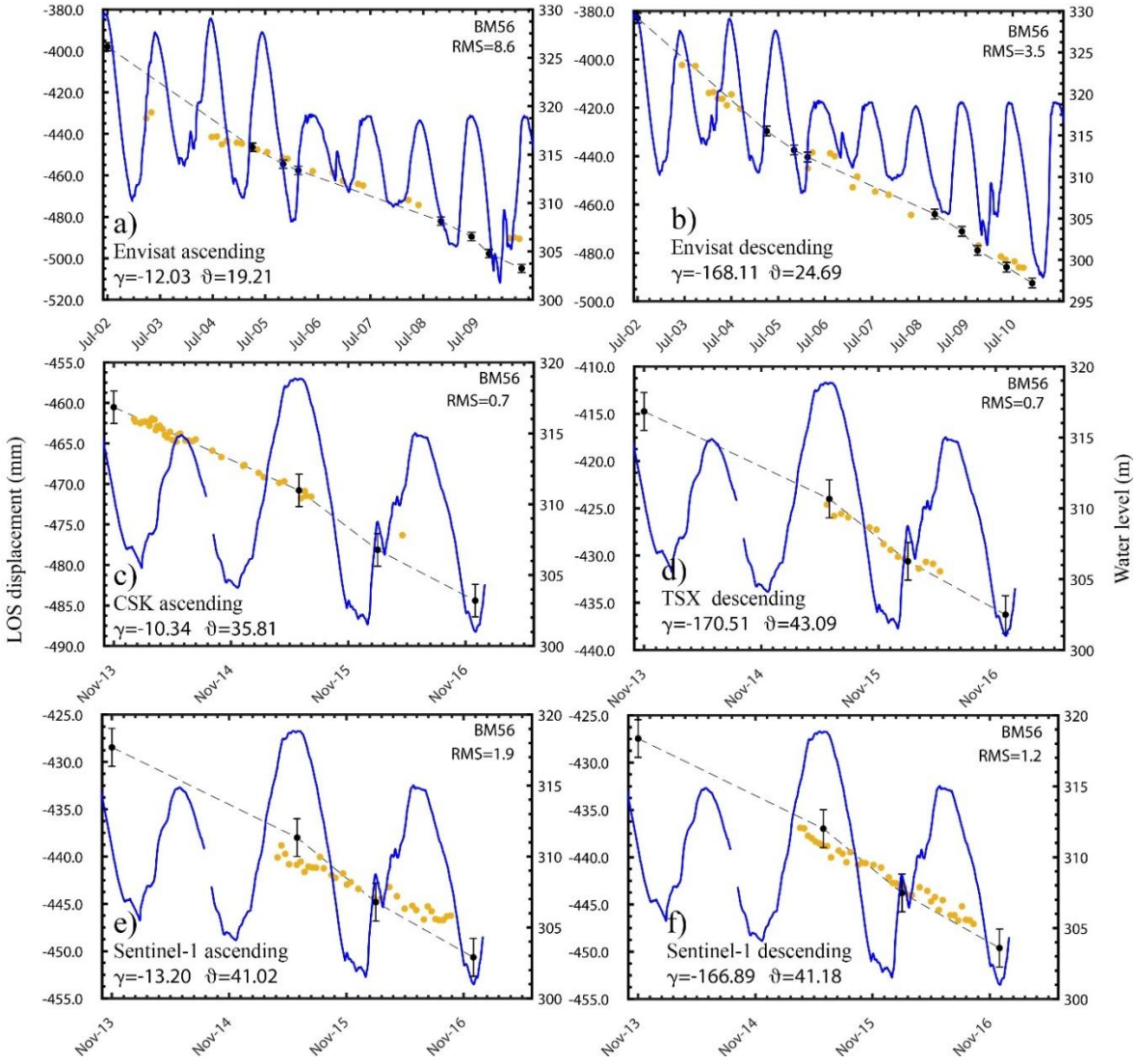

Figure 4.18. Agreement between levelling and InSAR timeseries for benchmarks located at the dam's deformation center (BM56), InSAR displacements were fitted to the leveling displacement by subtracting the mean difference between the two techniques, RMS value is indicated for each figure.

Figure 4.19. RMS map between levelling and InSAR timeseries for a) Envisat ascending and b) Envisat descending, BM 65 which is indicated with red circle has maximum RMS (≈20 mm) in both maps, background from Google Map.

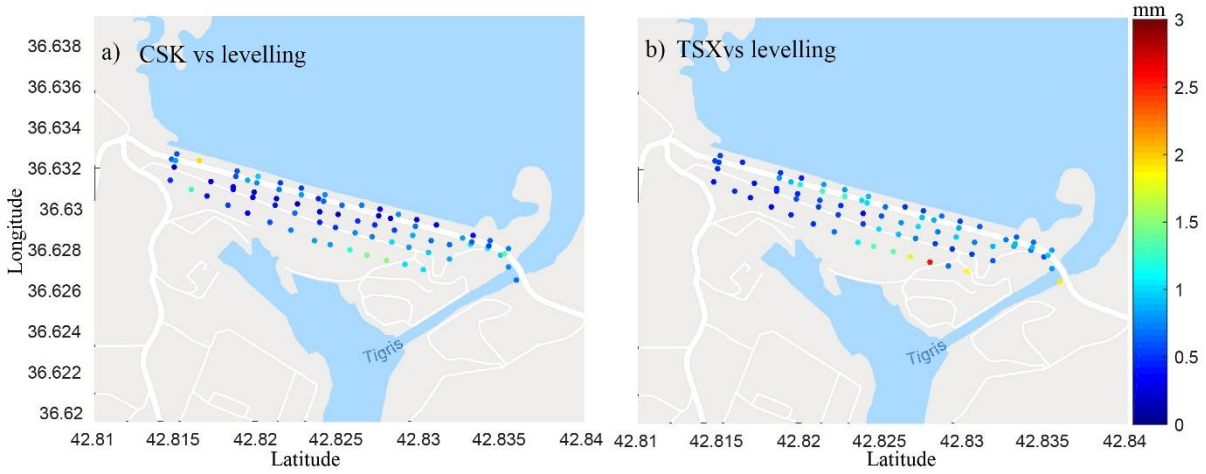

Figure 4.20. RMS map between levelling and InSAR timeseries for a) CSK ascending and b) TSX descending, background from Google Map.

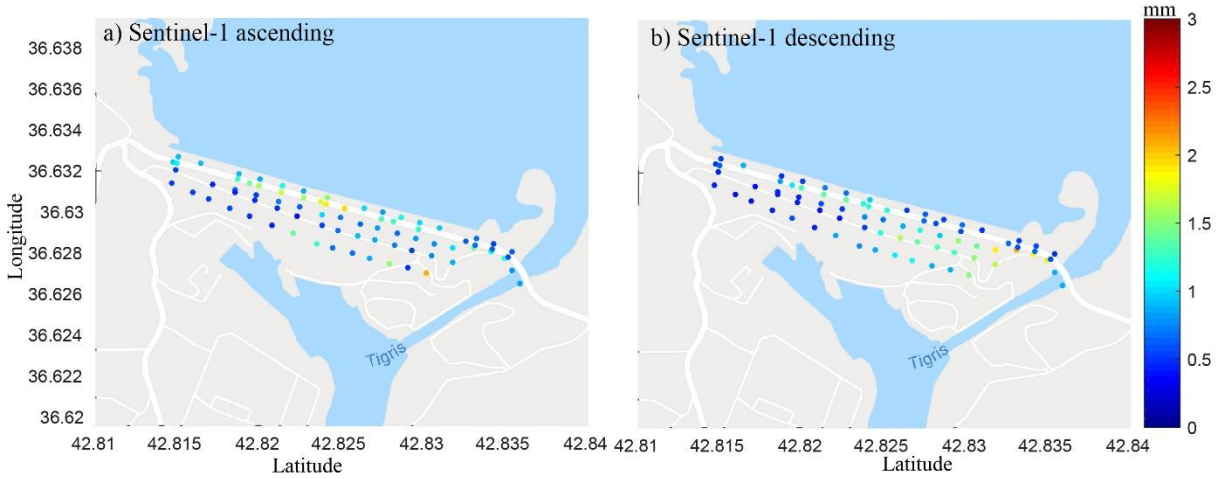

Figure 4.21. RMS map between levelling and InSAR timeseries for a) Sentinel-1 ascending and b) Sentinel-1 descending, background from Google Map.

4.4.6 Analysis of Mosul dam behavior between 1989 and 2017

Post construction deformation of dams continue long time after their construction has been completed. This deformation is indicative of the structure's performance to evaluate its task. Initially huge or unpredicted movements may be the only sign of critical process within a dam. If, however, the postconstruction subsidence can be empirically predicted, then a comparison of predicted and observed values can give indication to potential problems. To evaluate the behavior of dams, Sowers (1965) used a survey data of 14 rockfill dams. He found that the settlement per unit height, as a function of logarithm time, is always expressed in a straight line and can be expressed as follows:

$$\Delta H = C\alpha(\log t_2 - \log t_1) \tag{4.8}$$

in which ΔH = settlement to the embankment height percent between times t_1 and t_2 and Cα is the rate of ΔH. However, Clements (1983) argued that such approaches can lead to significant uncertainties in the predicted settlement if they used for different dams because they neglect important parameters such as the compaction procedures, construction method, embankment materials, etc. In other word, each dam should have a specific value of Cα. Accordingly, Clements (1983) suggests comparative approach between dam under study and other dams having similar characteristics. Based on Sowers's model, Charles (1986) suggested a settlement index S_I, which is analogous to Cα in equation (4.8) accept that the settlement rate expressed unitless per year instead of a percent of height per year. S_I can be used to evaluate the settlement of the dams as follows:

$$S_I = \frac{s}{1000 \times H \times log(t_2/t_1)} \tag{4.9}$$

where s is the crest settlement in mm measured between times t_1 and t_2 since the completion of the dam at a section of the dam with height of H meters (Charles, 1986).

Using the embankment height (H) for BMs on Mosul dam crest as the differential heights of points on the crest and those on the gallery, ΔH in equation (4.8) can be estimated as follows:

$$\Delta H = \frac{s}{H} \times 100\ \% \tag{4.10}$$

From equations (4.8), (4.9) and (4.10), it can be seen that $C\alpha = SI \times 100$. Charles (1986) suggests S_I value of 0.02 as a critical threshold in which a dam may suffers from a concerning process rather than the creep.

Hunter and Fell (2003) analyzed the deformation behavior of large number of dams during their normal deformation behavior. They used the long-term settlement index S_{LT} which equivalent to Cα to analyze the deformation of puddle core dams. The studied dams are divided into two groups: steady state and fluctuation state. In the steady state group, the water level was maintained almost constant level during the monitoring period while in the fluctuated group the reservoir water level was fluctuating in a normal operation. Based on available records analyzed by Hunter and Fell (2003) it was considered that Cα for normally behaved and steady state dams is less than 1% while dams operating in a large fluctuating water level Cα ranges between 2.6-7.5% which represent S_I of 0.026-0.075.

Figure 4.22 shows the possible scenarios of deformation in earthfill dams. The deformation can take place in the dam foundation as in Figure 4.22a or in the embankment as in Figure 4.22b. For the following discussion the terms S_{dam} and $S_{gallery}$ will be used to refer to the settlement of the dam body and foundation respectively. The total settlement observed on the dam crest is the summation of the possible settlement of these two components, i.e, S_{dam} and $S_{gallery}$. In addition, the dam settlement (S_{dam}) can involve abnormal movement caused by internal erosion or normal consolidation movement. Therefore, the total settlement can be expressed as follows:

$$S_{crest} = S_{dam} + S_{Gallery} \tag{4.11}$$

To evaluate the dam stability, S_I should be calculated using the total settlement observed on the dam crest (S_{crest}). Thus, any abnormal deformation on the dam body or the foundation can be detected by S_I.

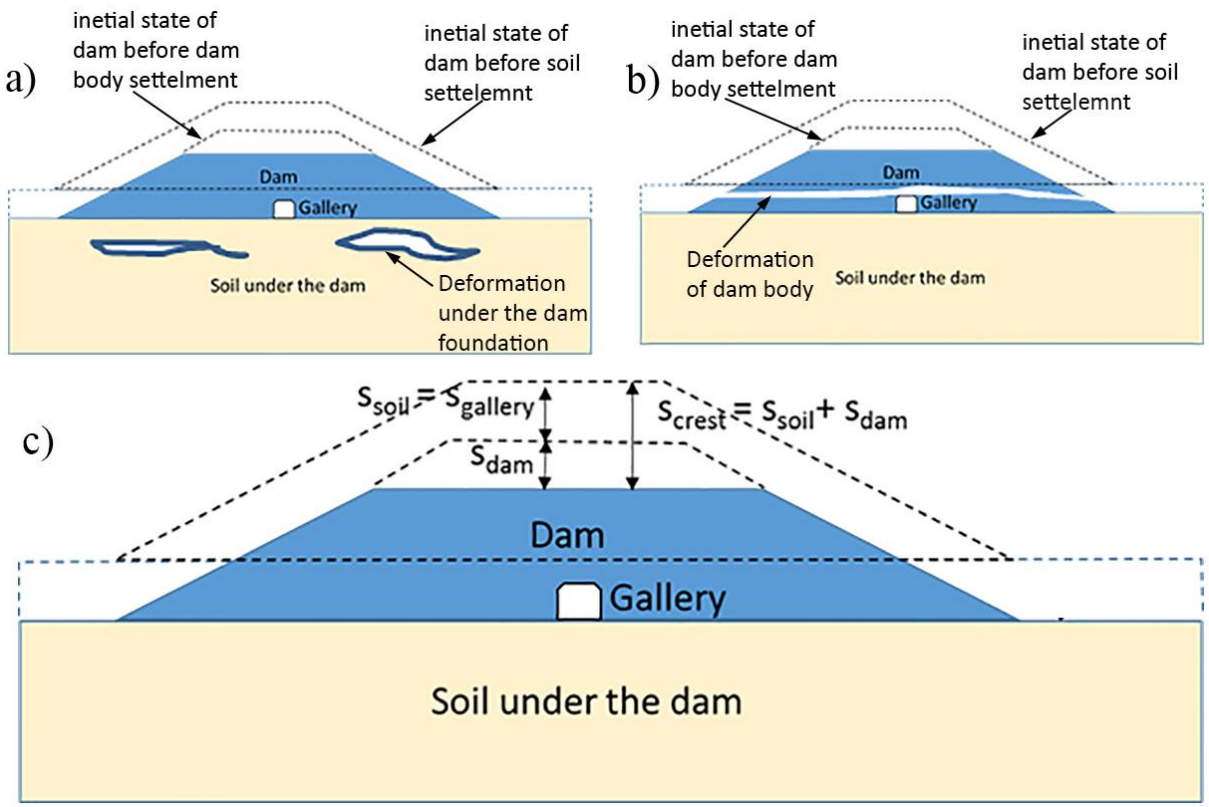

Figure 4.22. Possible deformation scenarios in earthfill dams (Tomás, 2018). a) deformation take place under the dam foundation, b) deformation takes place in the dam body and c) the relationship between crest, dam and gallery settlements.

Using Charles (1986) approach the settlement index S_I was calculated for the BMs on the Mosul dam crest. Figure 4.23 shows S_I calculated between 1989 and 2017 using the accumulated settlement since 1989. It can be seen that between 1989 and 2005 S_I was increasing and reached 0.007 just before lowering the water level significantly in 2005, which means that geotechnical conditions were worsening during this period. The increase of S_I is produced during the time period in which water level reaches maximum yearly elevation oscillations and maximum elevation levels. Additionally, S_I is less than the critical value (0.02) and thus, it means that there are not anomalous mechanism causing deformation besides creeping according to Charles (1986). For the period between 2005 and 2015 S_I was decreasing which means that geotechnical conditions are improving. It can be seen that S_I is slightly cambered between August 2009 and May 2012 due to the increase in the oscillation range of water level during this period and the mean S_I slightly increased after 2015. This increase may confirm the deterioration of the dam stability after the grouting work interruption.

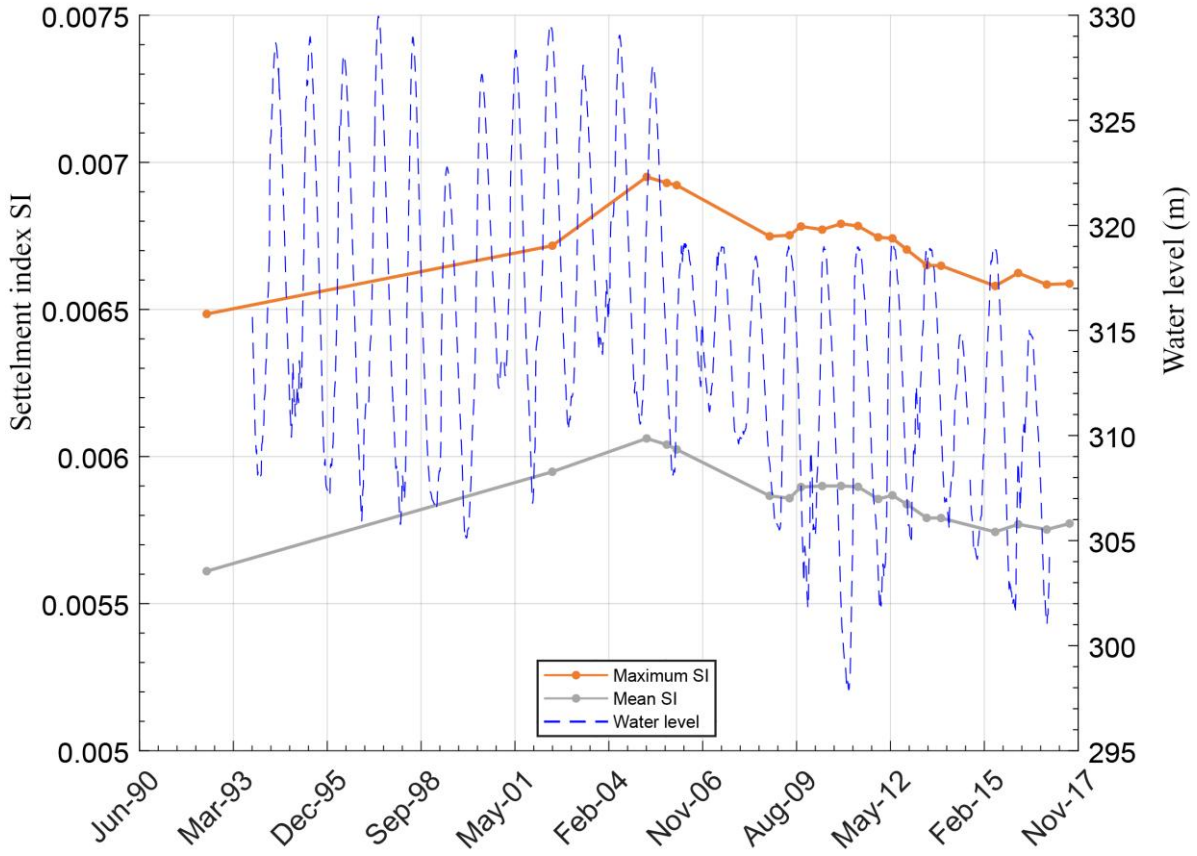

Figure 4.23. Mean and maximum settlement index SI over the period 1989-2017 calculated from 13 points on the dam crest with daily water level observations for the dam reservoir.

According to the previous observations, it is clear that S_I didn't cross the critical threshold (0.02). However, the dam was slightly settling while lowering the water level in 2005. Since the main concern about the Mosul dam is from the gypsum rocks dissolution, a sudden collapse of rocks under the foundation may occur. Thus, S_I may not be the best parameter to detect the collapse of the foundation since it depends on the total settlement observed on the crest. Therefore, other parameters such as the water seepage and the gypsum dissolution rate might be better to be used to evaluate the dam safety. Additionally, the spatial variation of crest displacement, which has been shown in section 4.4.1, is a concerning factor and thus further analysis for the temporal and spatial variation of the settlement will be discussed in section 4.4.7.

4.4.7 Separating benign and critical settlements

In sections 4.4.1 and 4.4.2, levelling data on the dam crest and gallery showed obvious anomalies in the dam's crest and foundations, thus it is essential to determine the critical areas at the dam foundation using the levelling data on the dam surface. Following Clements (1983) and Oscar and ASCE (1987), the mean Cα was calculated for all observations between 2005 and 2017 using equation (4.8). It is wealth to mention that the dam settlement (S_{dam}) was used

to calculate the mean Cα. Then the predicted settlement was modelled using the combination of equations (4.8) and (4.10) as follows (Clements, 1983; Oscar and ASCE, 1987):

$$s = \frac{H}{100} \times C\alpha(\log t_2 - \log t_1) \tag{4.12}$$

The predicted settlement for each levelling epoch is shown in Figure 4.24. The embankment heights for each benchmark was estimated from the differential elevation of benchmarks on the surface and those on the gallery. An assumption was made here that the river cross-section is identical to the gallery profile over the dam footprint to estimate the embankment height on the dam slopes.

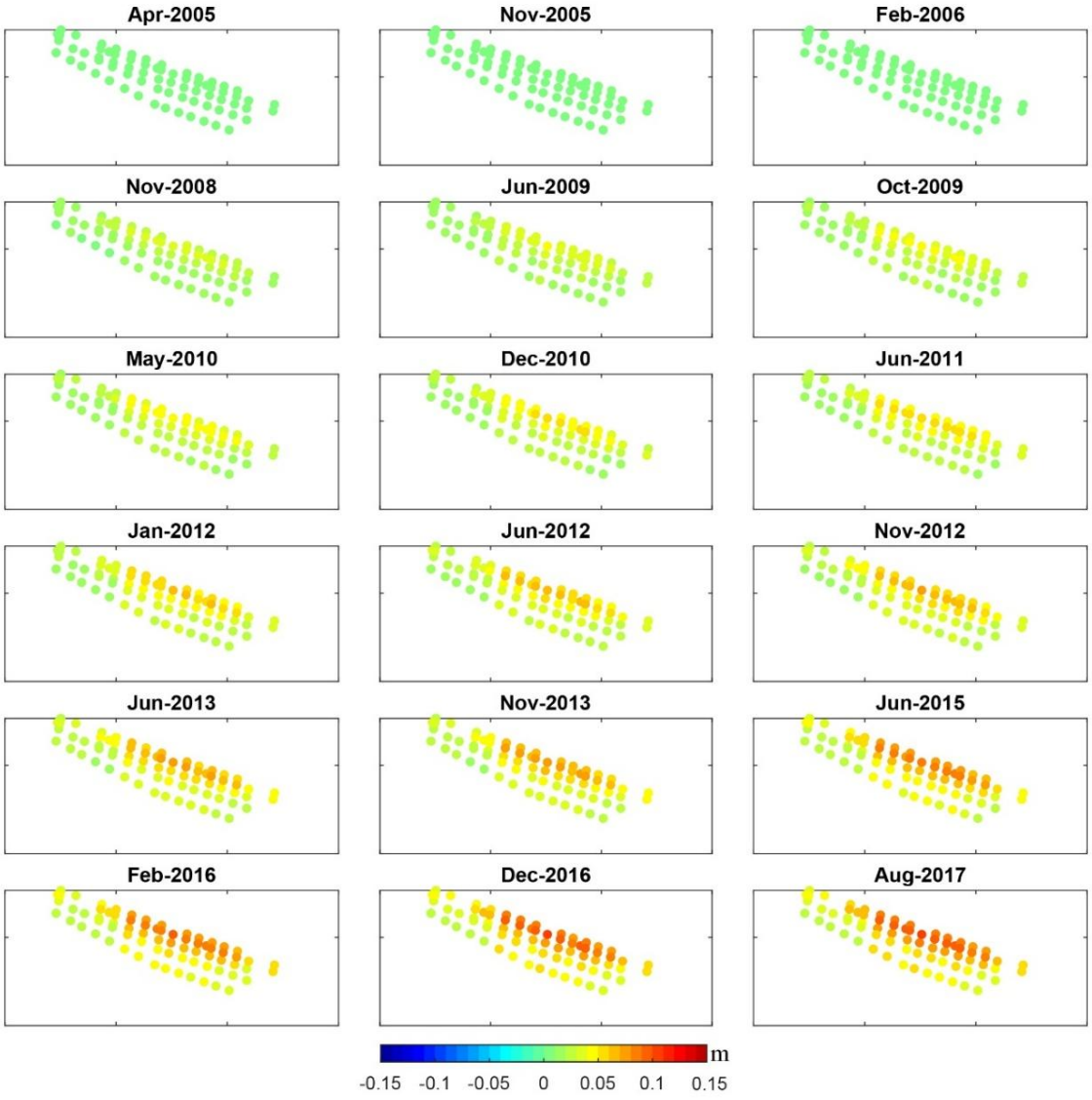

Figure 4.24. Predicted vertical displacement between April 2005 and August 2017 modelled using the mean settlement rate (Cα) of crest BMs between 2005 and 2017.

The modelled settlement is then subtracted from the observed settlement for each epoch to indicate areas that may have exhibited instabilities in the foundation. Figure 4.24 shows the

observed settlement while the residuals of the subtraction are shown in Figure 4.26. It can be seen that four areas exhibited unpredicted movement, which is very likely due to foundation movements. Two of these areas are located at the dam centre, with one of them on the crest and the other on the downstream slope. The other two areas are located on the east and west abutments of the downstream slope. The area on the east shows more localised displacement and has exhibited rapid subsidence in contrast to the other subsidence areas. These areas are very likely suffering from foundation movements. This is evidenced by comparing the settlement shown in Figure 4.26 with the gallery movement from the levelling data in Figure 4.10. It can be seen from these two figures that the displacement of the foundation at the centre of the dam is identical (≈ 25 mm).

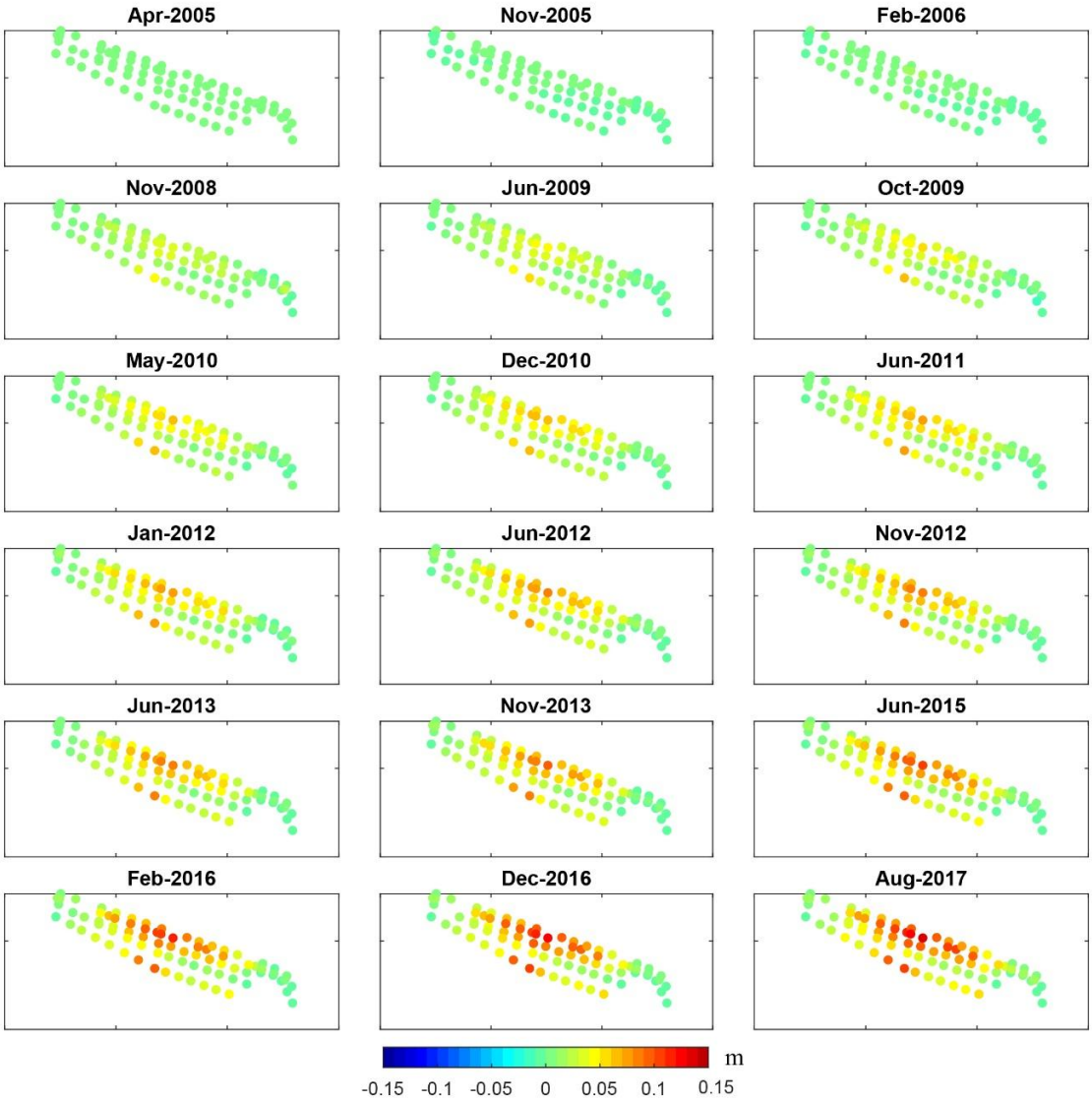

Figure 4.25. Observed vertical displacement during the period 2005-2017.

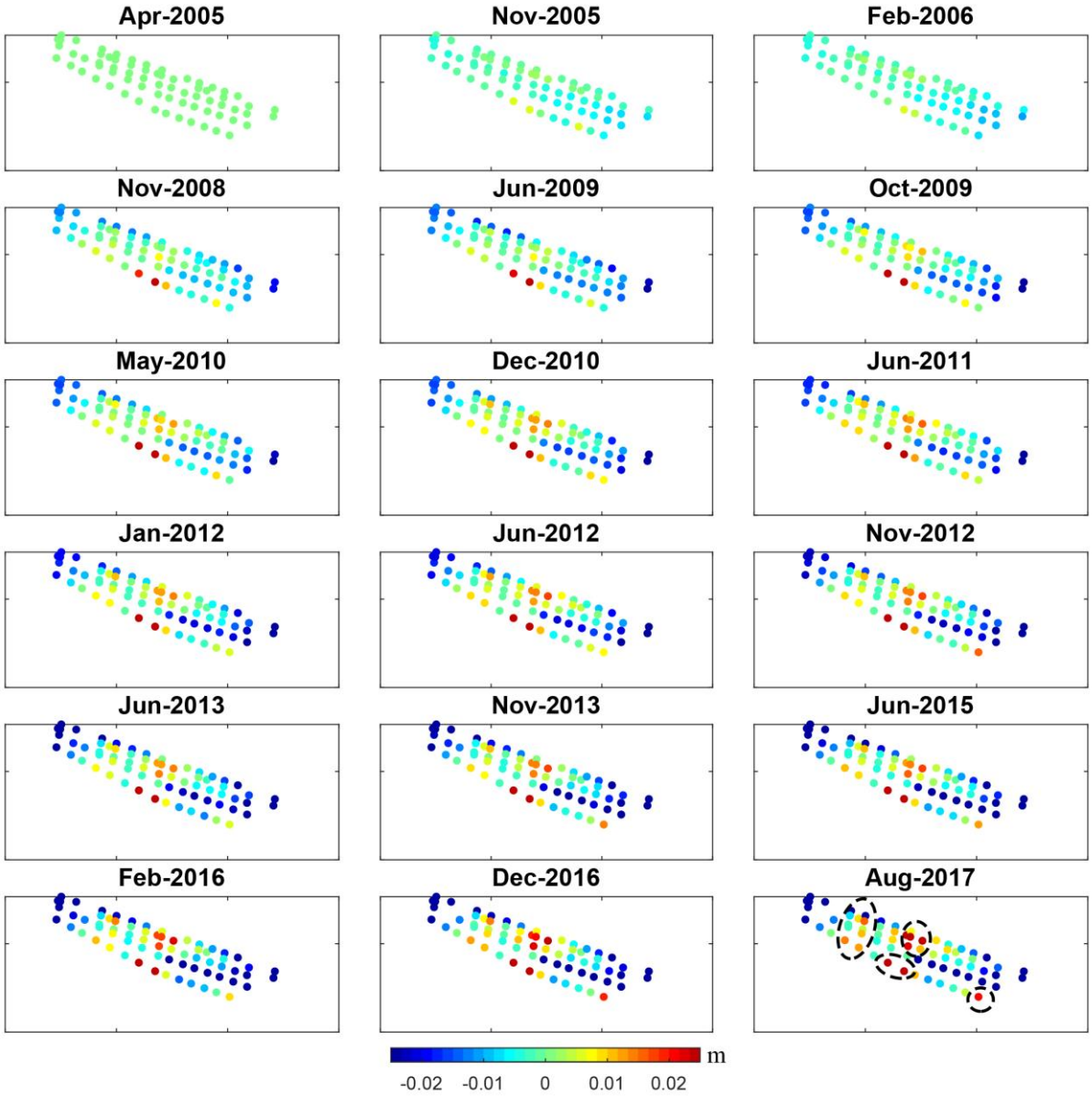

Figure 4.26. Vertical displacement of the Mosul dam after removing the predicted movement. Note that dashed black ovals indicate four regions with unpredicted settlements.

The spatial and temporal variation of vertical displacement on the dam, which is shown in Figure 4.26, is critical for the dam safety. Thus, monitoring of the dam displacement should continue carefully at least until the S_I trends starts decreasing. The procedure applied here to separate benign and critical dam movement is promising for application to InSAR. Although the levelling data have been successfully used to separate these two types of movement, there is a chance that some critical areas located between the benchmarks have not been detected. Therefore, the high spatial resolution of an InSAR deformation map can overcome this problem, and hence applying this procedure with the InSAR technique is one of the future plans arising from the finding of this thesis.

4.5 Conclusions

Mosul dam represents a serious threat to millions of people living in cities along the Tigris river basin between Mosul and Baghdad. The dam retains 11.11×10^9 cubic meters of water in the reservoir. The failure of the dam would be catastrophic, especially for Mosul city which is located about 70 km downstream of the dam. In this chapter, the dam's instability is addressed using two geodetic datasets. Levelling data collected between 2003 and 2017 for monitoring the dam embankment and its foundations along with radar images from Envisat, CSK, TSX and Sentinel-1 are used to examine the displacement of the embankment.

The analysis of the levelling data is carried out on the dam crest and gallery over the period between 1989 and 2017. The correlation between the dam's movement and the reservoir water level is also presented. The analysis was conducted along longitudinal cross-sections of the dam surface located on the upstream, the crest, and the downstream.

Additionally, SAR data from Envisat, CSK, TSX and Sentinel-1, collected between 2003 and 2017 were employed to monitor the displacement of the dam surface. The Envisat data cover the period between 2003 and 2010 with 22 images from the ascending pass and 24 images from the descending pass being used. High phase gradient and temporal gaps in the Envisat acquisitions resulted in a low coherence in some localized subsiding areas on the dam. Thus, manual unwrapping errors corrections was carried out. For the span between 2014 and 2017, three types of SAR datasets were used. Fourteen descending images from TSX covering the period between May 2015 and May 2016, 39 images from CSK covering the period between January 2014 and April 2016, 47 ascending and fifty-one descending images from Sentinel-1A/B covering the period between October 2014 and December 2017 were used in this study. The GAMMA InSAR processor was used for interferometric processing, and the TS+AEM time series package was utilised for the time series analysis. The TSX data between 2015 and 2016 show an acceleration of displacements. The horizontal and vertical displacement velocity maps are estimated using the 2D approach with the assumption that the horizontal movement is toward the downstream. The finding related to the velocity of the vertical displacement from levelling and InSAR analysis were cross-validated.

For the period between 2003 and 2010, the RMS of the difference between InSAR and levelling is 1.7 mm/year, with a correlation coefficient of 0.93. In contrast, for the span between 2014 and 2016, the RMS between InSAR and levelling data is 0.88 mm/year, and the correlation coefficient is 0.95. Further discussion about the agreement between InSAR and levelling was carried out by comparing the displacement timeseries from levelling with that from InSAR

results. The RMSE was less than 1 mm for TSX and CSK whiles it reaches 20 mm for Envisat over areas with localized displacement gradient. This can be due to low spatial and temporal resolution of Envisat images. This is evidenced by the good RMS from Sentenel-1 data that was about 1-2 mm.

Analysis from levelling and InSAR show that the Mosul dam has continuous movement for long time. The settlement index didn't cross the critical value since 1989. Furthermore, a spatial and temporal variation of movements is obvious over the dam crest and foundation which is considered a concerning factor for the dam safety. Monitoring of the dam movement and the water level fluctuation should continue until the dam reaches stability state.

Chapter 5. The Stability of the Darbandikhan Dam after the 12 November 2017 Mw 7.3 Sarpol-e Zahab (Iran–Iraq Border) Earthquake

5.1 Introduction

The 12 November 2017 Sarpol-e Zahab earthquake was one of the largest earthquakes occurring in the Iran–Zagros zone since 1900 (Alsinawi and Ghalib, 1975). About 396 lives were lost, and 7000 people were injured on both sides of Iraq–Iran border (BBC News Middle East, 2017), with the majority of fatalities occurring in the Iranian city of Sarpol-e Zahab, whereas Darbandikhan was the most impacted city in Iraq. The earthquake struck the northeast of Iraq, with its epicentre 30 km away from the Darbandikhan dam (Figure 5.1), and there is now serious concern about the Darbandikhan dam's safety. The dam was previously evaluated to be seismically safe under a maximum probable shaking of Mw 6.5 (Cordell, 2006). According to the map of the shaking intensity from the United States (US) Geological Survey (USGS) (Figure 5.1b), the dam lies within the region of 8 MMI (modified Mercalli intensity) for the 2017 event. Following this earthquake, the dam operators immediately lowered the water level in the reservoir because of concern about the dam's safety. The deformation of the dam body after the earthquake is visually apparent, and the State Commission on the Survey of Iraq observed several fissures on the crest soon afterwards. In the following months, this region exhibited 53 aftershocks with Mw >4.

Dams can be affected by earthquakes with several different types of deterioration, including: (1) slope failure; (2) cross-sectional and longitudinal cracks; (3) seepage from the foundation and the side slopes; (4) liquefaction of the dam body; (5) freeboard reduction; and (6) overtopping due to waves in the reservoir (Jansen, 1983; Seco and Pedro, 2010)

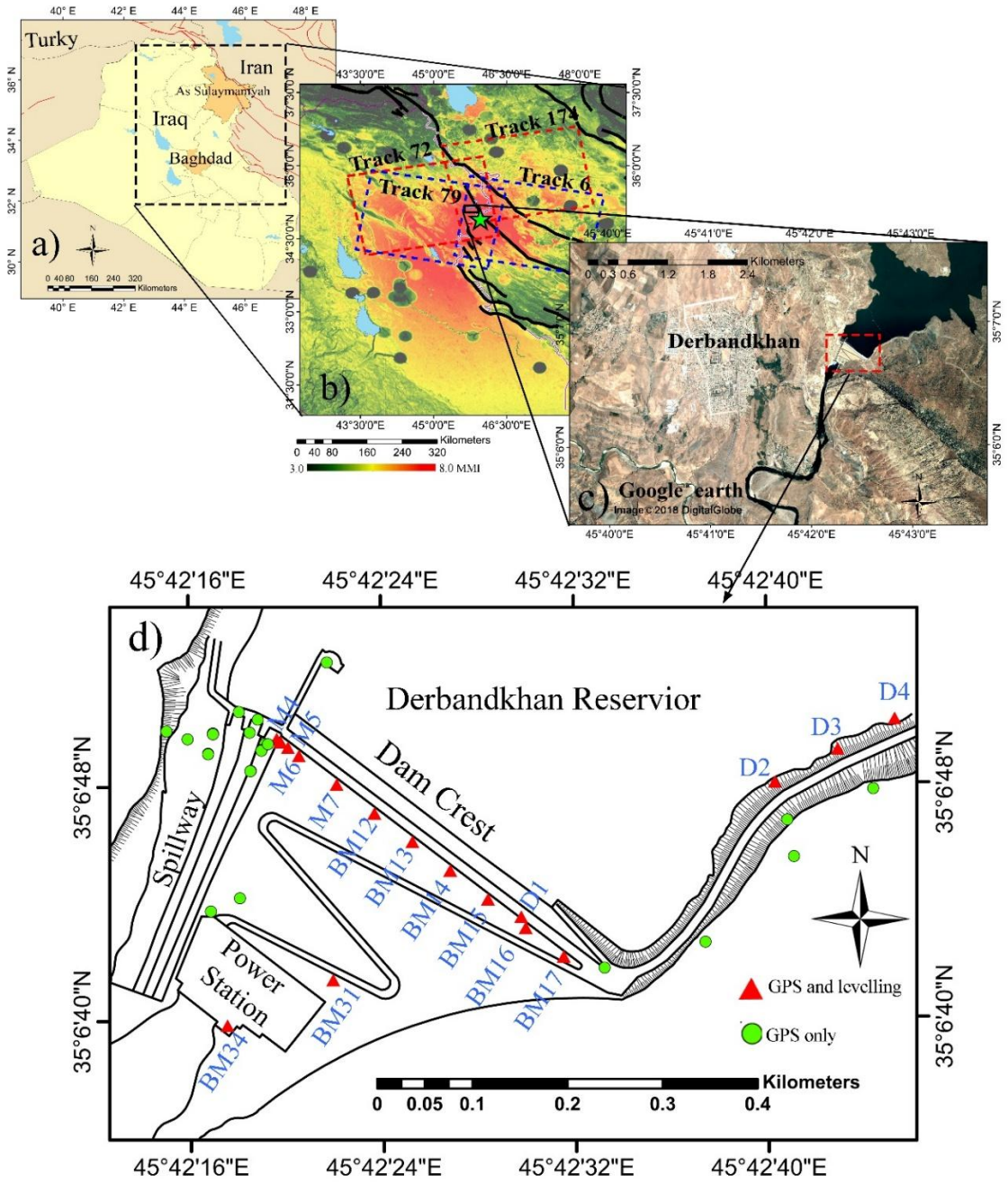

Figure 5.1 The geological settings of the Darbandikhan dam. (a) Regional map of Iraq, (b) shaking intensity map of the earthquake with geological faults indicated by black lines (USGS, 2017). The colour bar refers to the shaking intensity magnitude, the green star indicates the epicenter (USGS, 2017), (c) optical image showing the location of the Darbandikhan dam from Esri DigitalGlobe 2018) (d) the instrumentation network and the main features of the Darbandikhan dam. Triangles refer to the pillars observed with GPS, and levelling while circles indicate the pillars observed with GPS only.

The response of earth fill and rockfill dams to earthquakes differs according to the acceleration and velocity of the motion (Newmark, 1965), and also depends on the geological setting of the dam (Anastasiadis *et al.*, 2004). The most important factor that may affect the man-made infrastructure during an earthquake is the velocity of shaking (Newmark, 1965). When the acceleration is sufficiently large, the shaking causes a temporary downslope movement, which may reach 1.5 m (Serff *et al.*, 1976). Another critical factor is the construction quality. Dams

with a low degree of compaction are most susceptible to damage by earthquakes. The crest of the dam is the most vulnerable part during a seismic event, as its slopes can temporarily slide towards the toe of the dam. The failure of the dam can lead to permanent displacements along the slope and may extend to the whole surface or just part of the dam slope (Jansen *et al.*, 1995). Some notable dams were damaged by earthquakes with Mw > 6, e.g., the Sheffield Dam in 1925 and the San Andreas Dam in 1906 (both in California, US). Seco and Pedro (2010) reviewed several case studies of dam deformation following earthquakes, based on the history of embankment dams selected from all over the world. Not far away from the Darbandikhan dam, the Mosul dam threatened millions of people living downstream, and interferometric SAR (InSAR) has been used to detect its instability after the political instability of the area in 2014 (Milillo *et al.*, 2016a). The early detection of the instability of the Mosul dam with InSAR led to a maintenance plan to stabilize the foundation of the dam before it turned into a disaster (Annunziato *et al.*, 2016; Trevi, 2018). The worst scenario of dam failure triggered by an earthquake was the loss of 100,000 lives during the landslides following the 1786 Kangding–Luding Mw 7.7 earthquake, which struck Sichuan, southwest China (Dai *et al.*, 2005). Newmark (1965) discussed the mechanics of the dam structure during successive shakings. He suggested three possible movements of the dam: (1) dam slope motion either in the upstream or downstream direction; (2) creep of the whole dam in a specific direction; and (3) relative motion between the structural parts, which may lead to fissures in the dam body. The third is the most problematic, because it may be followed by internal erosion (Anastasiadis *et al.*, 2004).

Although the Darbandikhan dam lies in an active seismic region, there is no seismic instrumentation in the dam to monitor its behaviour during and after earthquakes. A previous concern about the safety of the dam was reported in Cordell (2006). This detailed report discussed the importance of monitoring the dam grouting gallery, as water seepage was observed here on more than one occasion (Cordell, 2006). Furthermore, it was reported that there was further concern about a landslide in the left bank and rock fill from the cliffs in the right and left abutments of the dam. Thus, there were some efforts to implement a maintenance plan between 2006 and 2010.

In This study three geodetic datasets namely: GPS, levelling, and Sentinel-1 data are integrated to evaluate the stability of the Darbandikhan dam in northeast Iraq after the 2017 Mw 7.3 Sarpol-e Zahab earthquake. GPS and levelling datasets collected in March and November 2017 were used to compute the co-seismic surface displacements of the dam. Sentinel-1 synthetic aperture radar (SAR) images collected between October 2014 and March 2018 were employed to recover the displacement time series of the dam. The large-magnitude displacement gradient

on the dam crest hindered the estimation of the co-seismic displacement using this medium-resolution SAR data. However, Sentinel-1 images are sufficient to examine the stability of the dam displacement before and after the earthquake. The results show that the dam was stable between October 2014 and November 2017, but after the earthquake, Sentinel-1 data shows a continuous subsidence of the dam crest between November 2017 and March 2018. To the best knowledge of the authors, this study is the first that utilises InSAR to investigate the behaviour of a dam after a large earthquake.

The layout of this chapter is as follow: Section 5.2 outlines the methodology used in the monitoring, including a description of the geodetic monitoring system, the principles of InSAR, and the limitations of small baseline subset (SBAS) InSAR to monitor the slopes of the dam. The results from geodetic and InSAR techniques are presented in Section 5.3, followed by a discussion of the main findings in Section 5.4. A summary and conclusions of the study are presented in Section 5.5.

5.2 Methods

5.2.1 Dam Instrumentation

The safety of Darbandikhan dam is inspected periodically by the Ministry of Water Resources/State Commission of Survey of Iraq by observing a geodetic network to detect any abnormal behaviour. Figure 1d illustrates the monitoring pillars of the dam, which are used in this study. This network consists of pillars installed on the dam surface, where regular GPS and levelling observations are taken, as well as levelling stations within the inspection gallery for which no relevant data are available. Only two epochs of GPS and levelling data, collected in March and November 2017, were available for this study. To plot a displacement profile of the dam crest and for analysis purposes, we consider the left edge of the spillway head (Station M4) as the reference. This is also applicable for calculating the gradient of displacement in Section 5.2.2.

Water seepage was monitored by nine piezometers installed in the dam body, and 23 piezometers installed in the gallery. Readings of the core piezometers taken during two periods—(i) from 1976 to 1978 and (ii) from January 1980 to May 1981 indicated normal behaviour of the dam (Cordell, 2006). The reservoir water level is monitored by a floating instrument installed close to the power station intake. The accuracy of the reading is ±10 mm.

5.2.2 InSAR

A total of 68 Sentinel-1 images from Track 6 were collected over the Darbandikhan dam. One of the limitations of using InSAR for dam monitoring is the foreshortening of the side slopes, which may result in underestimation of the deformation magnitude. Images of objects in the SAR images are projected to the line of sight (LOS) of the radar beam. Consequently, the distances of the dam slopes and crests appear to be shorter than their actual values by a factor depending on the SAR geometry and slope aspect. First, we investigated this compression factor, which is the ratio between slant and ground ranges, for the upstream and downstream slope in each track. The compression factor can be calculated as follows (Cigna *et al.*, 2014; Darvishi *et al.*, 2018):

$$R = \sin(\vartheta - \beta \cdot \sin(A)) \tag{5.1}$$

where ϑ is the incidence angle of radar signals, β is the dam side slope, and A is the aspect correction factor, which can be computed from the aspect of the slope (α) and the satellite heading angle (Υ). $A = \alpha - \Upsilon$ for the descending pass, and $A = \alpha + \Upsilon + 180°$ for the ascending pass (Cigna *et al.*, 2014). The parameters of Equation (5.1) are shown in Figure 5.2. Table 5.1 shows the compression ratios for different tracks of Sentinel-1 data on the upstream and downstream slopes of the dam. Over the downstream slope, tracks 72, 79, and 174 are more influenced by foreshortening than track 6, so we used images from track 6 only in this study. The same calculations over the upstream slope show that the foreshortening on the upstream slope is much more than that on the downstream slope. Although the upstream slope is often covered by water, the water level was reduced to a shallower level after the 12 November 2017 earthquake, and so part of this slope is now visible.

Table 5-1 Foreshortening compression factors over the upstream (UPS) and downstream (DNS) slopes of the Darbandikhan dam for both ascending (As) and descending (Ds) tracks. Note that (i) the average incidence angle for the dam area is provided for each track; (ii) the downslope of the dam (β) is 30°, and the aspect (α) is 220° for downstream and 40° for the upstream slopes. LOS: line of sight.

Track No.	Flight Direction	Heading (ϒ)°	LOS Inc (θ)°	A		Compression Factor	
				UPS	DNS	UPS	DNS
6	Ds	−167.0	45.6	53.0	233.0	0.29	0.90
174	As	−13.0	32.3	53.0	233.0	0.11	0.81
79	Ds	−167.0	34.9	53.0	233.0	0.15	0.84
72	As	−13.0	43.6	53.0	233.0	0.27	0.89

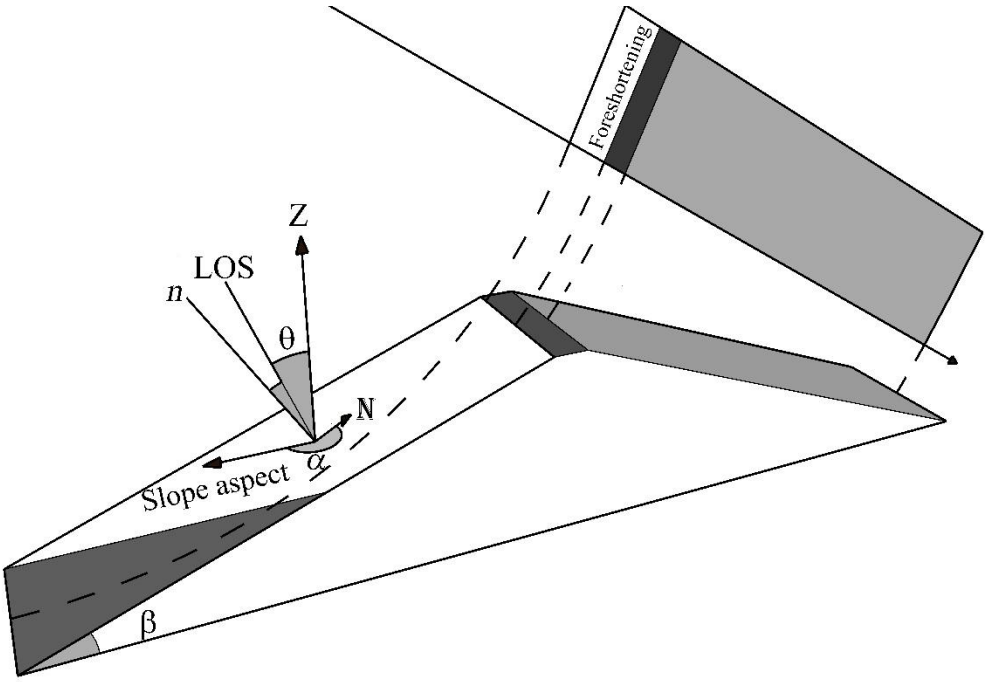

Figure 5.2. The foreshortening effect on the slopes of embankment dams. Plotted after Cigna et al. (2014).

According to Cigna *et al.* (2014), *R* takes values between 0 and 1 for each pixel on the dam surface. *R* = 0 when the LOS is perpendicular to the sloping surface, and *R* = 1 when the LOS is parallel to it. All of the pixels on a level surface, such as pixels on the dam crest, have:

$$R = \sin(\vartheta) \tag{5.2}$$

This is yielded by considering $\beta = 0$ in Equation (5.1). Thus, for pixels on the dam crest, *R* = 0.55 for the ascending pass, and *R* = 0.69 in the descending pass.

In Figure 5.3, the dam is indicated with red circles. The downstream slope of the dam and the terrain slopes facing to the radar LOS, look brighter than the other areas in the single-look complex (SLC) image. This is because the foreshortening increases the radar intensity (having more backscatter returned into a single pixel yield more intensity); the foreshortening factor *R* for slopes facing the radar is smaller than that for the slopes facing away from the radar LOS. Although tracks 72 and 174 are from the same ascending pass, those slopes look brighter in track 72. This is because the SLC image subset in Figure 3 is located in the far range of track 72, while it is in the near range of track 174. In other words, their incidence angles are different, leading to different foreshortening impacts.

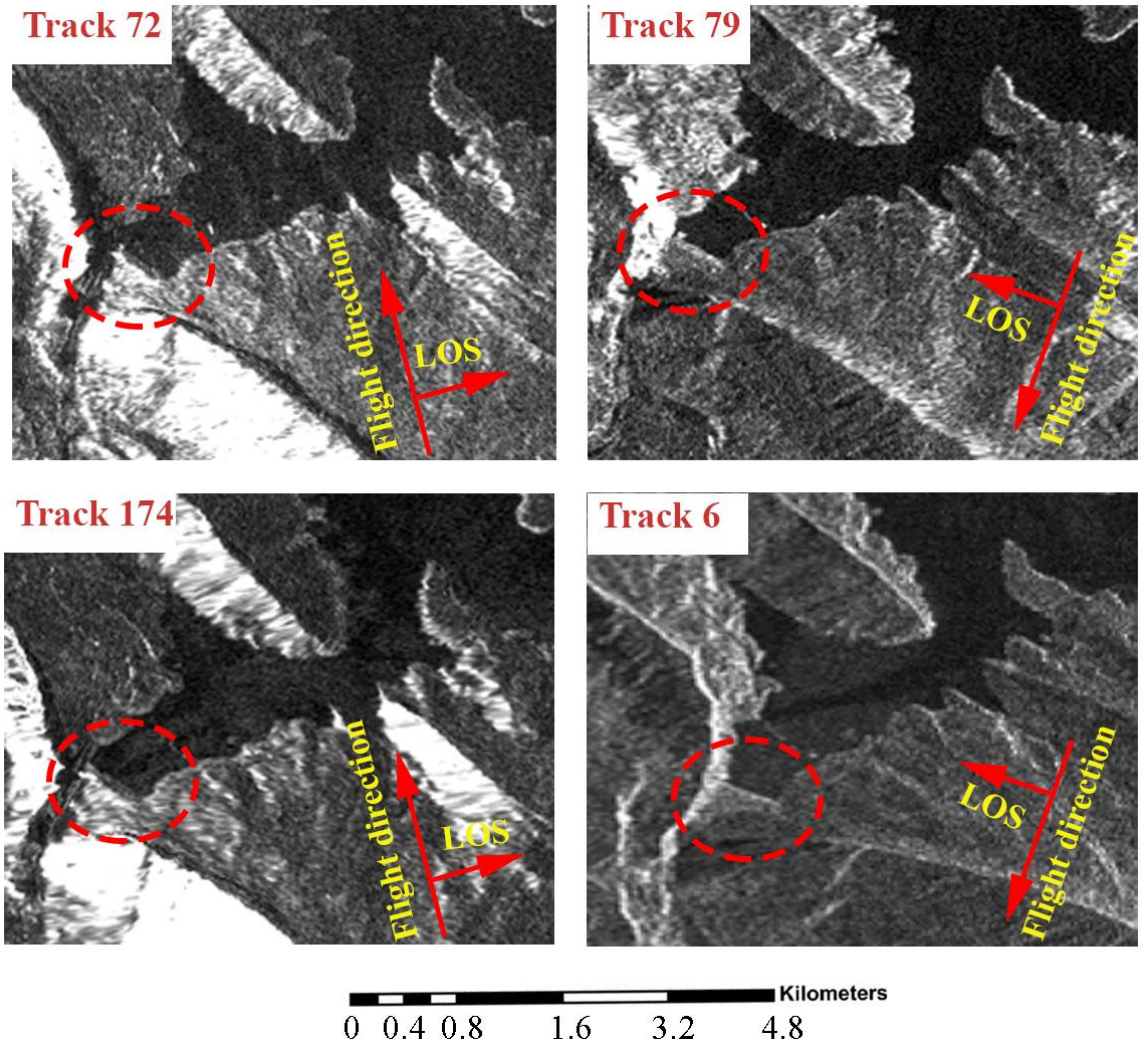

Figure 5.3. The foreshortening effects on the slope surface; four images from four tracks of Sentinel-1 images over the Darbandikhan dam. The dam is indicated with red circles.

Another limitation of InSAR is the difficulty of retrieving the LOS displacement when it exceeds the maximum detectable gradient (Di Traglia *et al.*, 2014; Singleton *et al.*, 2014). This limitation comes from an assumption that is made at the stage of phase unwrapping. This assumption is that the difference in the LOS phase changes between two adjacent pixels is less than $\pi/2$, which is equivalent to a difference of $\lambda/4$ in the LOS range changes because of the two-way travel path of the radar signals. To investigate the reliability of using Sentinel-1 for such large magnitude displacements, we computed the gradient along the LOS by simulating the LOS displacement from the levelling and GPS measurement on the dam crest using the following equation:

$$LOS_{dis} = E_G \sin\vartheta \sin\varphi + N_G \sin\vartheta \cos\varphi + U_L \cos\vartheta \qquad (5.3)$$

where LOS_{dis} is the projection of the three-dimensional (3D) displacement vector [E_G N_G U_L] to the LOS vector. E_G and N_G are the easting and northing components derived from GPS, U_L is the vertical component obtained from levelling, and ϑ and φ are the incidence angle of the

radar LOS and the azimuth of the satellite flight, respectively. The spatial resolution of the SAR images can be a critical parameter in cases of steep gradients of displacement (Singleton *et al.*, 2014). To evaluate the feasibility of the Sentinel-1 spatial resolution for such localised displacement over short distances (less than 500 m), the gradient of LOS displacement between every pair of adjacent benchmarks on the dam crest is computed by dividing the difference of their LOS displacements by the horizontal distance between them. Table 5.2 shows the computations of the simulated LOS displacement of Track 6 and the gradient between every pair of adjacent pillars on the dam crest.

Assuming the pixel size of the interferograms generated from Sentinel-1A/B is ≈20 m and the surface is completely flat (knowing that all of the benchmarks M4 to BM17 in Table 5.2 are on the crest), the maximum detectable gradient (MDG) of displacement is:

$$MDG = \frac{\lambda}{4D \times R} \tag{5.4}$$

where λ is the wavelength of the SAR system (0.0555 m for Sentinel-1), D is the pixel size, and R is the compression factor. Thus, the maximum detectable gradient is ≈1 mm/m, which is less than the LOS displacement gradient between all of the benchmarks on the dam crest, as shown in Table 5.2. In Table 5.2, the maximum gradient is 3 mm/m between M6 and M7. Thus, the minimum resolution required to detect this displacement is λ/4 g, which amounts to 4.57 m. In other words, when using data with a spatial resolution less than 4.57 m, it is impossible to recover such a large gradient displacement signal, which is evidenced by all of the co-seismic interferograms (Figure 5.4a) generated in this study. Here, we assume that the unwrapping path will follow the topmost part of the crest where the apparent displacement gradient is smallest. For points on the slope, the apparent displacement gradient G will be:

$$G = g/R \tag{5.5}$$

where g is the actual displacement gradient, and R is the compression factor. On the downstream slope, the gradient of the displacement will be significantly larger, because R is at most 0.69, and hence unwrapping errors are likely, hindering any estimation of co-seismic displacement using Sentinel-1 data. Following a different unwrapping path with a steeper gradient would require a spatial resolution better than 4.57 m. The High-Resolution Spotlight or the Starring Spotlight (SP) acquisition modes of TerraSAR-X are the most suitable to recover such large-gradient co-seismic displacements, but these were unavailable for our study. Consequently, Sentinel-1 data was used only to investigate the dam surface displacements before and after the earthquake, whereas the co-seismic displacements were estimated from GPS and levelling data.

The GAMMA software (Wegmüller *et al.*, 2009) was used for InSAR processing. Two constraints were applied to select the interferograms: (i) the perpendicular baseline should not exceed 400 m, and (ii) the time separation of the two SAR acquisitions should be less than 180 days. All of the SLC images were co-registered to one master. The differential interferograms were filtered using the adaptive filtering algorithm (Goldstein and Werner, 1998). This step was performed to increase the signal-to-noise ratio in some incoherent pixels so as to reduce the likelihood of unwrapping errors in the next step. The differential interferograms were unwrapped using the minimum cost network flow two-dimensional (2D) unwrapping method (Goldstein *et al.*, 1988; Costantini, 1998). The surface displacement time series and the mean linear velocities for each pixel were generated using the in-house InSAR TS+AEM software, which essentially employs the small baseline subset (SBAS) approach (Li *et al.*, 2009). Recent studies suggest that tropospheric delay products from external datasets such as the Global Navigation Satellite System (GNSS) and European Centre for Medium-Range Weather Forecasts (ECMWF) can be used to reduce the atmospheric effects on radar measurements (Yu *et al.*, 2017; Yu *et al.*, 2018a), which can, in turn, facilitate time series analysis (Li *et al.*, 2018; Yu *et al.*, 2018b). However, due to the small extent of the dam, we did not expect large spatial variations in the atmospheric water vapour. Thus, no such external information was used to mitigate atmospheric effects.

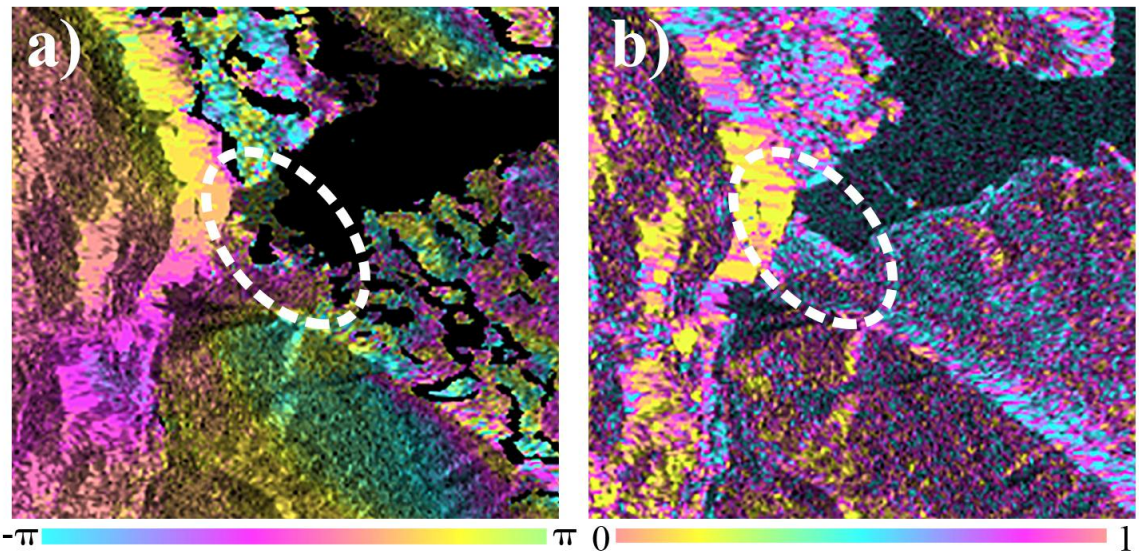

Figure 5.4 Co-seismic interferogram (7 November 2017 – 19 November 2017): (a) Interferogram, and (b) Coherence. Darbandikhan dam is indicated with white oval.

Table 5-2. The gradient of LOS displacement simulated from the global positioning system (GPS) and levelling data collected in March and November 2017 on the dam crest benchmarks. The incidence angle of the radar LOS is 45.65°, and the azimuth of the satellite flight is 260.59°.

BM	Latitude (Decimal Degrees)	Longitude (Decimal Degrees)	Orthometric Elevation (m)	East Displacement (m)	North Displacement (m)	Vertical Displacement (m)	Distance from M4 (m)	LOS Displacement (m)	Gradient (mm/m)
M4	35.11375536	45.70548463	477.959	0.103	0.069	−0.144	0	−0.187	
M5	35.11370024	45.70557167	479.410	0.121	0.066	−0.154	10.01	−0.207	−2.0
M6	35.11362193	45.70569536	481.547	0.143	0.068	−0.185	24.24	−0.244	−2.6
M7	35.1133471	45.70612983	482.839	0.193	0.119	−0.342	74.21	−0.395	−3.0
BM12	35.11307236	45.70656465	479.039	0.173	0.149	−0.470	124.2	−0.474	−1.6
BM13	35.11279793	45.70699924	478.886	0.169	0.205	−0.509	174.14	−0.505	−0.6
BM14	35.11252439	45.70743219	480.342	0.127	0.225	−0.462	223.91	−0.445	1.2
BM15	35.11224962	45.70786674	479.169	0.103	0.236	−0.391	273.88	−0.380	1.3
BM16	35.11197574	45.70830231	483.574	0.057	0.232	−0.249	323.86	−0.247	2.7
BM17	35.11169989	45.70873661	489.682	0.013	0.139	−0.123	373.89	−0.117	2.6

5.3 Results

5.3.1 InSAR Time Series

To investigate the behaviour of the dam before and after the earthquake, we generated the displacement time series using 68 Sentinel-1A/B images collected between October 2014 and March 2018. Only acquisitions from track 6 were used to generate the SBAS time series, because they are less distorted, as discussed in Section 3.2. We separated the time series into two time spans. Figure 5.4 shows the spatial–temporal separation of the acquisition for each time span. For the pre-seismic period between October 2014 and 7 November 2017, we generated the SBAS time series using 54 Sentinel-1 images. Figure 5.5a shows the mean LOS velocity map of the dam before the earthquake. The maximum rate of displacement of any point on the dam crest, with respect to the phase unwrapping origin point on bedrock just to the east of the dam (Figure 5.5b), is 4 mm/year during this period. Note that the apparent uplift across areas of higher topography away from the dam most likely represents residual atmospheric effects that are unrelated to deformation across the dam, and can be neglected. The time series error map is shown in Figure 5.7.

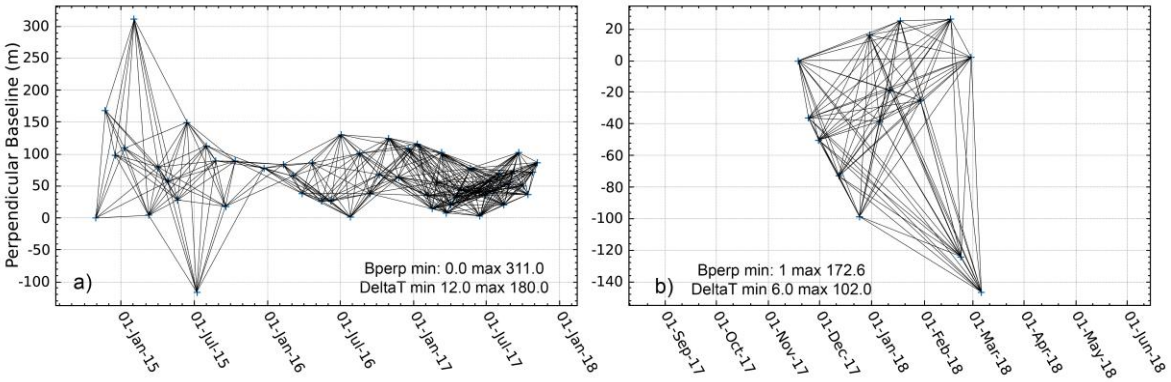

Figure 5.5 The perpendicular baseline network for a small baseline subset (SBAS) time series (a) before the earthquake and (b) after the earthquake.

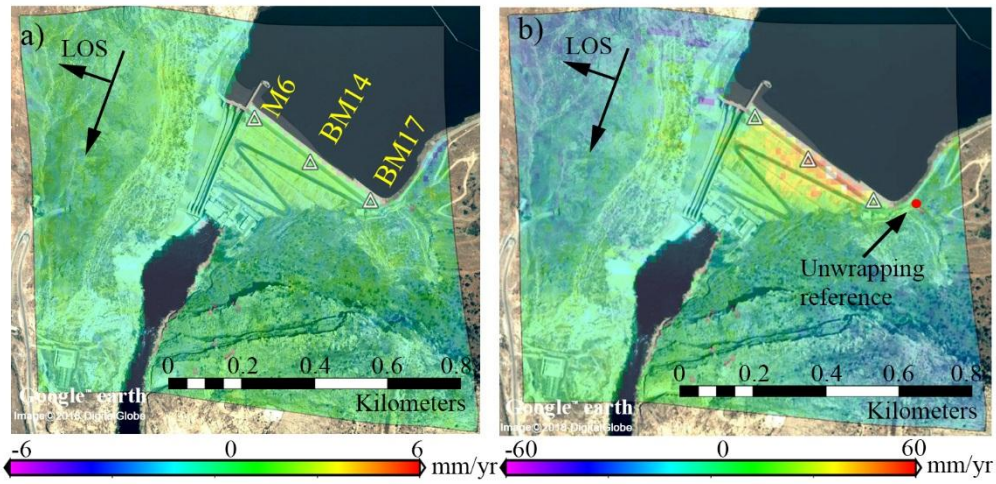

Figure 5.6 (a) The mean linear velocity estimated from Sentinel-1A/B before the earthquake event, during the period from 30 October 2014 to 7 November 2017, (b) the mean linear velocity after the earthquake, during the period from 19 November 2017 to 7 March 2018. Note that (i) the earthquake occurred on 12 November 2017 at 18:18 UTC, (ii) the reference point for phase unwrapping is indicated by the red dot in the abutment southeast of the dam, and (iii) positive implies that the Earth's surface moved away from the radar sensor (i.e., subsidence in the radar line of sight), and negative implies uplift in the radar LOS.

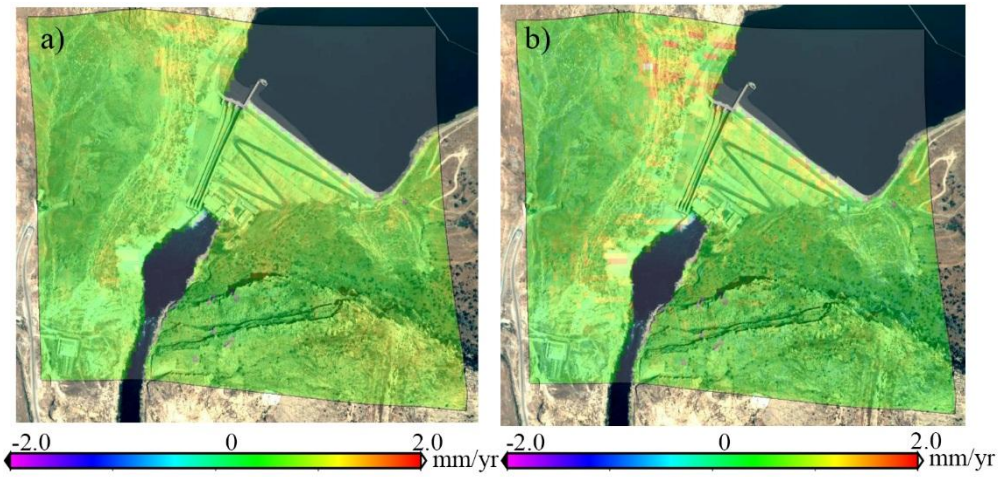

Figure 5.7 The corresponding error maps of the mean linear velocity maps in Figure 5.6a and b respectively.

Figure 5.5b shows the post-seismic LOS velocity map using 14 Sentinel-1A/B images between 19 November 2017 and 7 March 2018. The error map of the SBAS time series is presented in Figure 5.7. To connect the pre-event and post-event time series at the monitoring pillars on the dam crest, we estimated the LOS displacement for each benchmark from GPS and levelling data using Equation (5.3). Figure 5.6 illustrates the LOS displacement time series of three points on the dam crest—M6, BM14, and BM17—which are indicated in Figure 5.5a. BM14 is located close to the centre of the dam, and the other two are on the western and eastern edges, respectively. It can be seen that the dam was stable before the earthquake, but there is a rapid displacement of BM14 after 11 November 2017, and it is clear that the dam crest is continuously

moving, even four months after the earthquake, with a 17-mm LOS displacement of BM14 between 19 November 2017 and 7 March 2018.

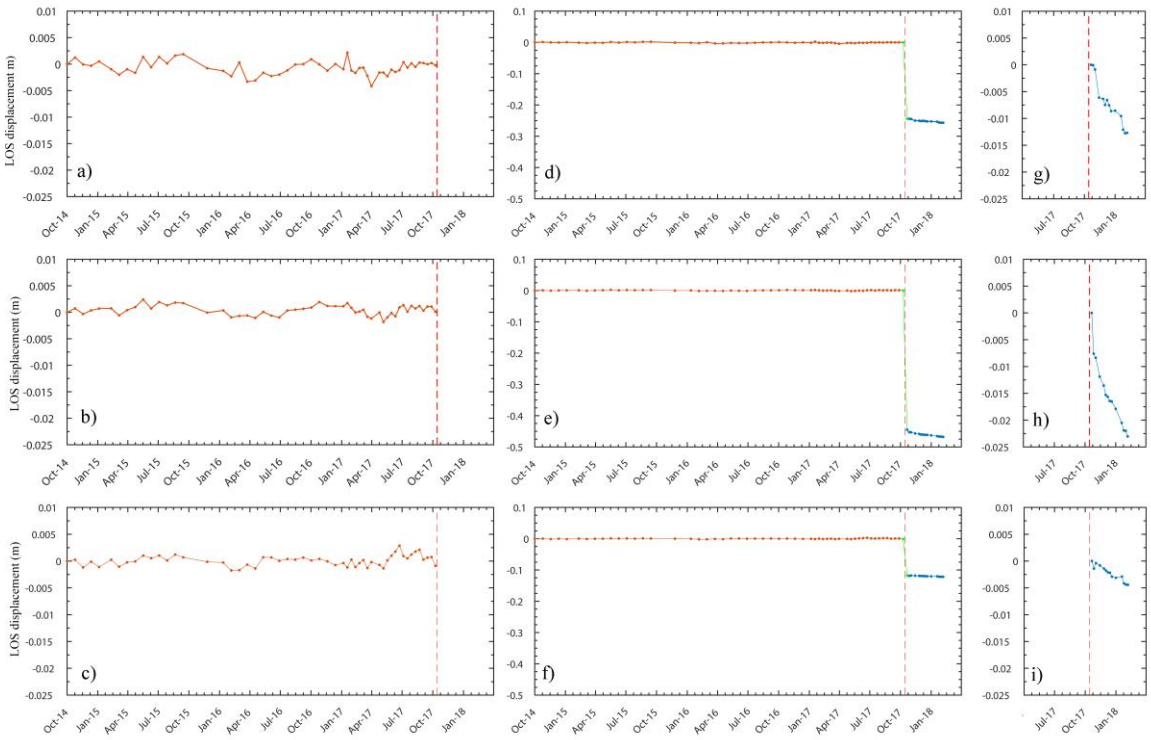

Figure 5.8 The LOS displacement of two time series: from October 2014 to March 2018 of three points on the Darbandikhan dam crest: M6 (top row), BM14 (middle row), and BM17 (bottom row). The location of each point is indicated in Figure 5a. (a–c) The time series of the displacement before the earthquake. (d–f) The time series before and after the earthquake is connected using the co-seismic movement estimated from GPS and levelling. (g–i) The post-seismic movement estimated from the SBAS time series. The ranges of panels (a–c) and (g–i) are identical. Note, to be consistent with GPS and levelling displacements, interferometric synthetic aperture radar (InSAR)-derived displacements were multiplied with −1, so that positive implies that the Earth's surface moved towards the radar sensor (i.e., uplift in the radar LOS), and negative implies subsidence in the radar LOS.

5.3.2 Co-Seismic Displacement from GPS and Levelling Measurements

The first GPS and levelling campaign was carried out in March 2017, and the second was carried out in November 2017. Figure 5.9 shows the absolute co-seismic displacements relative to ITRF08. Four stable points (indicated by a black oval) outside the dam body and close to the spillway moved by a similar magnitude to the spillway head and the dam toe (both indicated by red circles). The average horizontal displacement of these four stable points is approximately 0.12 m in the southwest direction, which represents the absolute co-seismic movement of the dam and its surrounding area. It is well-known that relative movements are more crucial in terms of dam safety. Therefore, the average displacement of the four stable points away from the dam body, which are indicated by the black oval in Figure 5.9, is subtracted from the dam movements. Figure 5.10 shows the vertical and horizontal relative displacements of the dam crest and its spillway measured by GPS and levelling after subtracting this average horizontal

movement. The maximum relative horizontal displacement measured by GPS is 0.27 m at station BM13. The relative horizontal displacements of the left and right abutments are around 0.14 m and 0.12 m, respectively. It can be seen that the pattern of displacement of all of the points on the crest tends towards the centreline of the dam. The pillars near the centre of the dam moved perpendicular to the dam axis, while points on the right and the left of the dam moved in the northeast and northwest directions, respectively.

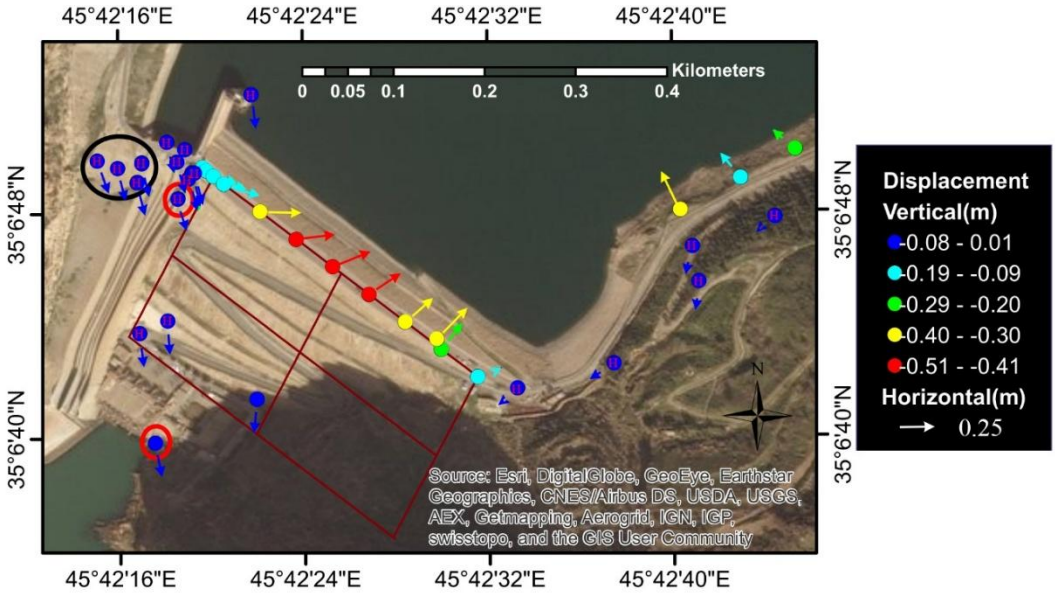

Figure 5.9 The horizontal (indicated by arrows) and vertical (indicated by circles) displacements of the monitoring pillars on Darbandikhan dam measured by GPS and levelling. The source of the background image is from (Esri, DigitalGlobe 2018). Note that (i) the horizontal displacements are referenced to ITRF08, and (ii) the pillars labelled with letter H were measured with GPS only.

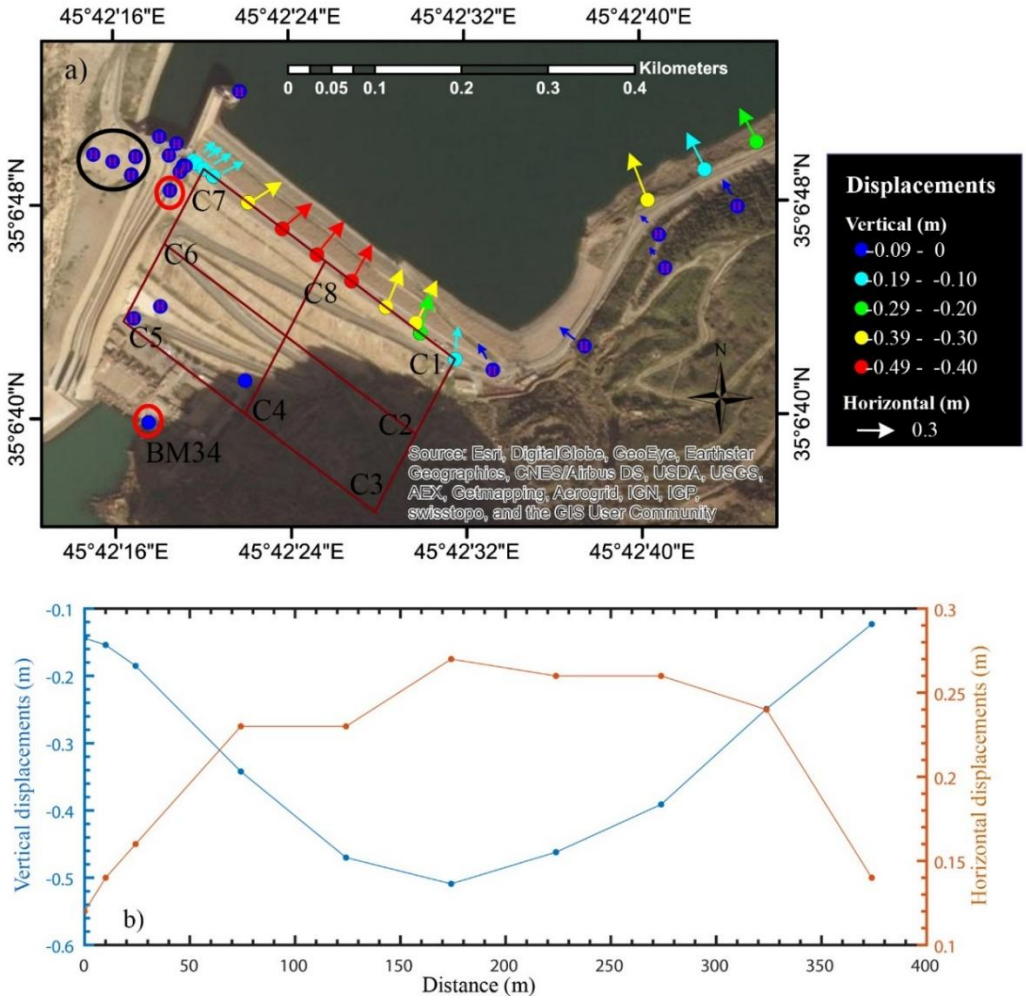

Figure 5.10 The relative vertical and horizontal co-seismic displacements inferred from levelling and GPS measurements collected in March and November 2017. The source of the background image from Esri) (a) arrows indicate the direction and magnitude of the horizontal displacements, and different colours of circles represent different magnitudes of the vertical displacements. The red lines labelled with C1–C8 refer to the displacement cross-sections in Figure 5.9. (b) The cross-section of C7–C1 for both the vertical and horizontal displacements.

The relative vertical displacement measured by the levelling is shown as coloured scale circles in Figure 5.7a, and depicted as a blue vertical profile in Figure 5.7b. The subsidence of the central part of the dam is more than 0.50 m. The vertical displacements of the points on the left and right abutments range from 0.15 m to 0.45 m.

5.4 Discussion

The LOS mean velocity maps in Figure 5.5, which were derived from the InSAR time series, show different patterns of settlement on the left and right parts of the dam. It is understood that the water level in the reservoir was lowered immediately after the earthquake, which could be the reason why there was no water seepage crossing the dam body at that stage. The emergence of cracks on the downstream side slope can be more dangerous than those upstream or on the crest. No crack has yet been observed on the downstream slope of the Darbandikhan dam, but

minor cracks could be hiding beneath the boulder-covered face of the slope due to the difficulty of observing cracks in such a surface.

It is clear in Figure 5.7 that different parts of the dam displaced with different magnitudes in both the vertical and horizontal directions, although the maximum displacement is focussed in the centre. As suggested by Newmark (1965) and Herndon (1990), such behaviours are expected for Earth fill dams during an earthquake. Shaking the embankment of the dam results in the non-uniform displacement of different parts of the embankment, depending on the acceleration. The direction of the shaking may impact the magnitude of the displacement, while the movement must be along the slope aspect in spite of the direction of the shaking, because of the gravity. In addition, the slope in the centre of the dam is expected to be longer than the left and right sides, suggesting a V section of the bedrock along the dam axis. This suggestion is evidenced by the gallery design that was constructed along the dam axis following the bedrock and leaving 75 m of the dam section without any gallery (Cordell, 2006). We expect that this section was left without the gallery because the bedrock along the river section is too steep, which may hinder the construction of the gallery in this section. Therefore, the most affected part of the dam is the crest, and maximum deformation can be observed close to the dam centre when the embankment height and the slope length are maximum. This behaviour is evidenced by several cracks that appeared on the left and right abutment of the Darbandikhan dam after the earthquake.

According to (Cordell, 2006), the dam's surrounding area exhibited several landslide events in the past. The GPS displacement vectors above the reservoir to the east of the dam show consistent downslope local movements. Thus, continuous monitoring of the area is essential, especially given that the region exhibited several minor aftershock events. Higher-resolution radar images (e.g., TerraSAR-X and COSMO-SkyMed) are desirable for monitoring the upstream dam slope, which is expected to move more than the downstream slope, according to the GPS and levelling data.

Figure 5.11 shows six displacement cross-sections derived from the SBAS InSAR time series between November 2017 and March 2018. The location of each cross-section is depicted in Figure 5.9a. Figure 5.11a–c are cross-sections that are parallel to the dam axis, arranged from the top to the toe of the dam, respectively. As inferred from the GPS and levelling, the topmost section shows the greatest displacement. Figure 5.11d–f show the displacement on three cross-sections along the downstream slope that are arranged from the west to east abutment,

respectively. Figure 5.11e is along the centreline of the slope, and similarly shows the greatest displacement at the dam crest.

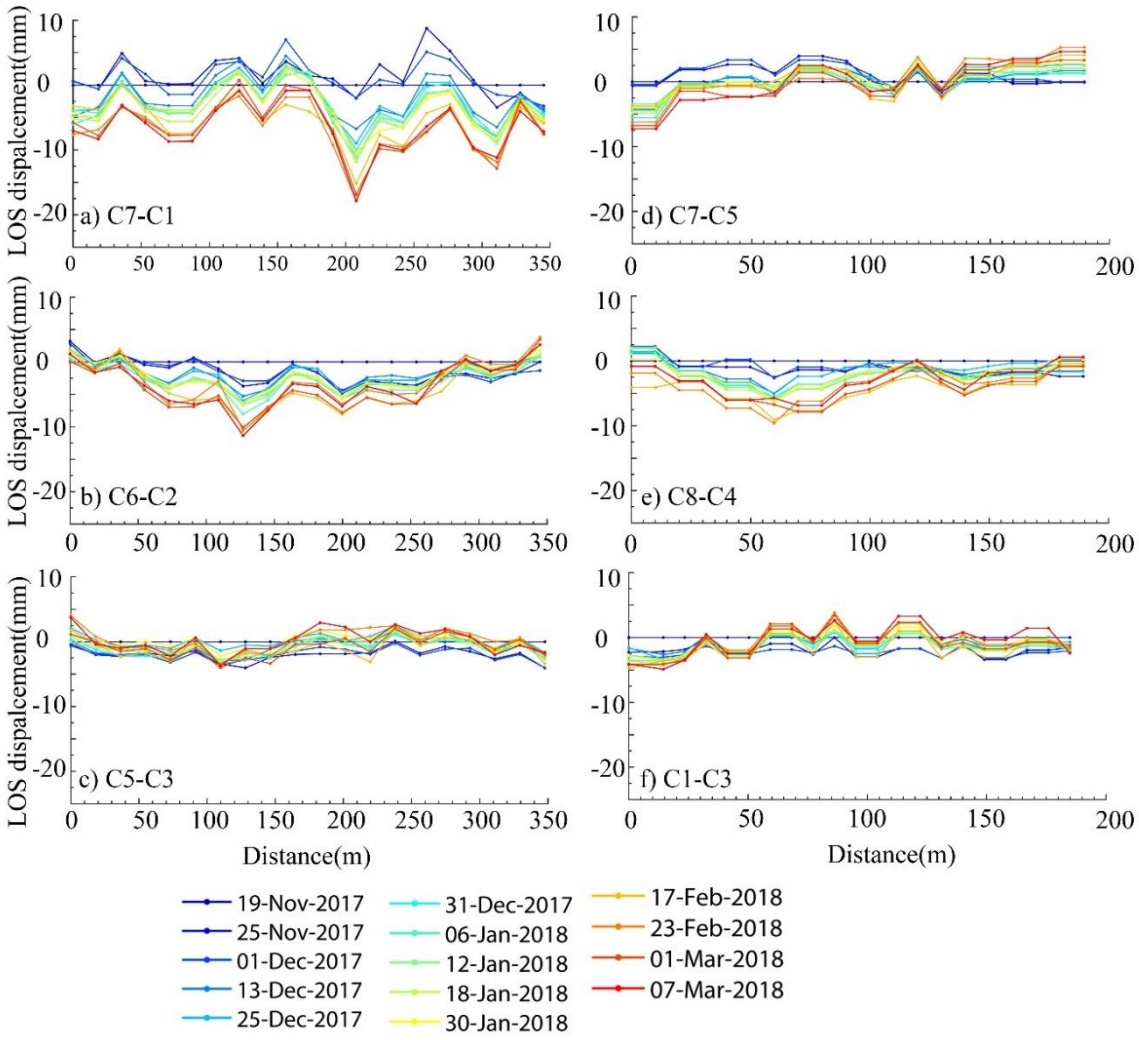

Figure 5.11 Cross-sections of InSAR-derived LOS displacement time series during the period from November 2017 to March 2018. (a) C1–C7, (b) C6–C2, (c) C5–C3, (d) C7–C5, (e) C8–C4, and (f) C1–C2. Note (i) negative values indicate that the surface moved away from the satellite radar; (ii) the location of each cross-section is shown in Figure 5.7a.

5.5 Conclusions

In this chapter, the impact of the Mw 7.3 Sarpol-e Zahab earthquake on the deformation of the Darbandikhan dam in northeast (NE) Iraq was demonstrated. Three geodetic techniques were used to investigate the dam movements before, after, and during the earthquake. Due to the steep gradients of the co-seismic displacements, GPS and levelling measurements were utilised to observe the distortion of the dam body caused by the earthquake, suggesting movements of up to 270 mm in the horizontal direction and 500 mm in the vertical direction. We discussed the limitations of using InSAR techniques for monitoring sloping surfaces, and the spatial and temporal resolution required to recover large-gradient displacements. The rate of the dam displacement before and after the earthquake was investigated using InSAR time series analysis

with 68 Sentinel-1 images collected between October 2014 and March 2018. Our results suggest that the dam was relatively stable before the event, with a maximum LOS velocity of 4 mm/year, but after the event, the crest of the dam was still creeping at a rate of up to 70 mm/year until at least March 2018. These results suggest that spaceborne InSAR monitoring of the post-seismic dam deformation is useful to inform maintenance plans, but that episodic terrestrial surveys remain essential in case of large-gradient deformation during future earthquakes.

Chapter 6. Conclusions and recommendations

6.1 Conclusions of the research

Over the last few decades, Interferometric Synthetic Aperture Radar (InSAR) has been employed to map deformation and topography of the Earth's surface. The main goal of this thesis is to investigate the potential of using InSAR for dam deformation monitoring. This study was carried out on two major dams in Iraq. Mosul dam has been classified as one of the most dangerous dams in the world and this thesis has combined multi-platform SAR data with 25-years of levelling for the first time to investigate its stability. This data was used to examine the stability of the dam and to validate the InSAR results. In addition, GPS, levelling and Sentinel-1 data have been integrated for the first time to investigate the stability of the embankment of Darbandikhan dam after the 7.3 Mw Sarbol-e Zahab earthquake. The main conclusion that can be drawn is that InSAR can be used for monitoring the stability of dams, although some factors should be kept in mind such as the dam's orientation, the temporal and spatial resolution of the images and the gradient and velocity of the displacement on the dam surface. According to the settlement index the behaviour of the Mosul dam is not concerning however a remedial work and monitoring should continue due to the spatial and temporal variation of movement over the dam surface and gallery. In terms of the evaluation of the stability of Darbandikhan dam, the results showed that the dam embankment was not stable at least for three months after the earthquake.

The main contributions of this thesis are as follows:

1. The stability of Mosul dam has been assessed for the first time through the integration of 25-year in-situ data and 14-year radar observations.
2. A collection of SAR data from four platforms was used to estimate the velocity of the Mosul dam's displacement, with the validation of this estimation conducted using the levelling data collected between 2005 and 2017. This validation has been carried out for the first time for this dam and no previous study has used such a large number of datasets to validate InSAR results.
3. The separation of benign and critical movement using levelling data over the Mosul dam has been carried out for the first time. This procedure was used to distinguish between benign settlements and critical processes such as foundation movement. The results from this procedure are promising and the same procedure with InSAR could be used to detect foundation settlements from space.

4. An integrated analysis using GPS, levelling and Sentinel-1 data has been used for the first time to assess the behaviour of the Darbandikhan dam's embankment after the 2017 7.3 Mw Sarpol-e Zahab earthquake.
5. A procedure has been developed to estimate horizontal and vertical displacement using SAR data from two or more tracks, assuming the direction of the horizontal movement towards the downstream direction.

The conclusions of this thesis described below are linked to the five research questions presented in Chapter 1, followed by a summary of the main contributions of this thesis.

6.1.1 InSAR for dam deformation monitoring

Research Question 1: To what extent can InSAR be used to monitor an earthfill dam's deformation? How can vertical and horizontal displacement be determined using two or more SAR tracks? How accurate is the use of InSAR to measure dam deformation?

In Chapter 4, multi-platform SAR data collected between 2003 and 2017 were analysed to investigate the Mosul dam displacements during this period. All interferometry processing was carried out using GAMMA, whereas the SBAS timeseries analysis was performed with the in-house software TS+AEM package (Li *et al.*, 2009). Data from six tracks and four platforms were utilized for this purpose and the results show a maximum displacement velocity of 10 mm/year between 2003 and 2010, whereas for the period between 2014 and 2017 the datasets from CSK, TSX and Sentinel-1 shows displacement velocity of 7-10 mm/year along the LOS. This range of velocity arise from the different imaging geometries and spatial resolutions used. However, the TSX data show a more rapid displacement velocity after 2014 due to the suspension of the grouting work in August 2014. This acceleration in the displacement velocity is not clearly shown in the other datasets due to insufficient spatial resolution and imaging geometry.

The vertical and horizontal displacement components were estimated using a 2D model. This was conducted using two tracks from the Envisat data collected between 2003 and 2010 assuming no movement along the dam axis. In contrast, two tracks from Sentinel-1 and one track from CSK were used to estimate vertical and horizontal movements during 2014-2017. The velocity maps show no significant horizontal movement while the maximum vertical displacement velocity ranges between 9-11 mm/year.

In section 4.4.5 a comparison was carried out of values of displacement velocity from the analysis of InSAR and levelling data. The vertical displacement velocity estimated from InSAR was compared to the that from levelling data. The comparison shows an RMSE of 1.7 mm/year and a correlation of 0.93 between 2003 and 2010, whereas an RMSE of 0.88 mm/year and correlation of 0.95 between 2014 and 2017. The high correlation between the two techniques is promising for the use of InSAR as an alternative or supporting technique for dam monitoring. However, some localised subsiding area on the eastern part of the dam embankment, were not shown in the InSAR deformation maps.

To examine the agreement between InSAR and levelling timeseries for each dataset, the levelling timeseries was projected into the LOS direction. The RMS between levelling and InSAR was computed for each dataset. Envisat data showed large RMS that reaches 20 mm in areas with high displacement gradient. For other areas with lower displacement gradient the RMS doesn't exceeds 8mm. The RMS between TSX and CSK from one side and the levelling data from the other side is less than 1mm, whereas the RMS between Sentinel-1 and Levelling is 1-2 mm.

The good agreement between InSAR and levelling timeseries confirms the effectiveness of InSAR for monitoring embankment dam.

6.1.2 The stability of the Mosul dam using levelling data between 1989 and 2017

> *Research Question 2: How has the deformation of the Mosul dam developed over the dam surface and foundation. Is there any heterogeneity in the foundation displacements?*

A brief history of Mosul dam and a summary of construction information have been presented in Chapter 3. The problematic geology of the dam's foundation was discussed in section 3.3.2. It was shown that the presence of gypsum rocks in the dam foundation is critical for dam safety. The continuous subsidence of the dam crest and foundation was discussed in sections 4.4.1 and 4.4.2 respectively. For the period between 1989 and 2017, the maximum subsidence in the dam crest was 610 mm whereas it was 420 and 530 mm in the upstream and downstream slopes for the same period. To compare the behaviour of Mosul dam with other worldwide dams, the settlement index was determined for the dam crest. The results show that the settlement index didn't cross the critical value. Also, the dam movement pattern shows a spatial and temporal anomaly on the dam crest and slopes which is considered as indication of the dam safety issue. Thus, careful monitoring of the settlement and water level fluctuation should continue.

The stability of the dam foundation was assessed using levelling data from 150 benchmarks installed along the dam gallery. The settlement of the dam galley was analysed during the period between 2005 and 2017. This analysis shows continuous subsidence around the three stations 0+413, 0+959 and 1+339 on the gallery. The localised settlement of the dam foundation can loosen the compacted layers of the embankment which are closer to the crest and, accordingly, fractures on the puddle core can develop due to fluctuations in the water level leading to a possible dam failure.

6.1.3 The behaviour of the Mosul dam after the cessation of grouting in August 2014

Research Question 3: How has the Mosul dam behaved before and after the suspension of grouting work in August 2014?

In section 4.4.2 the displacement of three stations of the dam foundation was discussed. These stations show an acceleration of the displacement after 2009. For the period between 2011 and 2013 the foundation was relatively stable, but after 2014 the displacement accelerated again. The halting of the grouting work after 2014 is very likely the reason for this acceleration. Thus, remedial work is crucial to keep the foundation stable.

6.1.4 Separating the deformation of the embankment from foundation subsidence

Research Question 4. How can different components of dam displacement be distinguished in order to determine the critical ones?

Deformation from a benign process can interfere with other critical deformation types on the dam surface and prevent the detection of such critical deformation. In section 6.1.2, a procedure to separate benign deformation from critical movement over Mosul dam is presented. The displacements of points on the gallery and their upper points on the crest were used to model the coefficient of secondary consolidation $C\alpha$, which was found to be 0.45 and that is in agreement with the expected values for clayey soils (Charles, 1986). This coefficient was then used to predict the vertical displacement of the crest and the predicted value were then subtracted from the observed displacement on the crest. This procedure is used to detect the problematic areas which on the foundations using observation collected on the dam surface. This will contribute to focus the grouting work on areas in which the foundation is inaccessible for investigations. The successful application of distinguishing between secondary consolidation and other critical processes is encouraging for the application of this procedure to InSAR technique and this is one of the areas of future work arising from the findings of this thesis.

6.1.5 Utilizing InSAR and conventional geodetic approaches to investigate the Darbandikhan displacement after the 2017 Mw 7.3 Sarpol-e Zahab earthquake

Research Question 5: How can terrestrial observations be integrated with SAR data to monitor rapid displacements in earthfill dams? How has the Darbandikhan dam behaved after the 7.3Mw Sarpol-e Zahab earthquake?

In addition to internal erosion and water seepage in dams posing a safety concerns, seismic issues are also problematic in cases of dams located in seismically active areas. Monitoring dams during and after seismic events is important in evaluating dam performance. InSAR can be an effective tool in the evaluation of dam behaviour before and after earthquakes. The 7.3 Mw Sarpol-e Zahab earthquake on the border between Iraq and Iran seriously affected the Darbandikhan dam. In chapter 5, an integration of three independent datasets was used to evaluate the dam stability after this earthquake. The large co-seismic displacement of the embankment prevented an estimation of co-seismic movement. Vertical displacement from levelling and horizontal displacement from GPS data were used to simulate the co-seismic movement and to link the two InSAR timeseries, one before the earthquake and the other after it. The two timeseries were generated from Sentinel-1 data collected between 2014 and 2018. To estimate the relative movement of the embankment with respect to the area surrounding the dam, the general co-seismic movement of the area was estimated from GPS observations for benchmarks located outside the dam embankment and this movement was subtracted from the movement of the dam embankment. The results show that the dam was quite stable before the earthquake but because of the severe shaking, the embankment was no longer stable for at least three months after the earthquake. The maximum displacement velocity after the earthquake was 17 mm/year along the LOS. Although data from Sentenle-1 with moderate spatial resolution was used, this study confirms the possibility of using InSAR to evaluate the instability of dams after earthquakes.

6.2 Further discussion of the limitations of InSAR for dam stability monitoring

It has been demonstrated that InSAR is a powerful and effective tool for dam deformation monitoring in this thesis, however users should keep in mind the following limitations of InSAR while employing it for dam stability monitoring: (i) the Dam-vs-SAR geometry (including the radar azimuth and incidence angle, dam aspect and slope), and (ii) the dectable maximum displacement gradient of InSAR and its relationship with the wavelength and pixel size of SAR imagery. For example, the compression factor, which is the ratio of slant to ground range distance, over the dam slope can impact on performance in the use of InSAR for the detection

of deformation. The magnitude of the compression factor, which is discussed in detail in Chapter 5, depends on the incidence angle, the direction of the platform movement, the spatial resolution of the SAR image and the orientation and slope of the dam. The following paragraphs introduce a briefly discussion of the relationships between these factors.

The relationship between the dam's aspect orientation and the compression factor over a dam having an embankment slope of 23.5˚ and observed with ascending images having an incidence angle of 45˚ is shown in Figure 6.1a. It can be seen that the best dam orientation that mitigates the foreshortening factor would lie between 45˚ and 180˚. In contrast, a dam slope having an azimuth orientation between 210˚ and 300˚ will be strongly affected by foreshortening. Figure 6.1b shows the relationship between the compression factor and the dam orientation when ascending images are used. It can be seen that the relationship is reversed in contrast to that in Figure 6.1a. This effect of the dam orientation can be noticed in the high RMS between the leveling and the ascending Envisat data (see Figure 4.19).

Furthermore, the horizontal creep of the dam may be under estimated if its direction is parallel to the satellite orbit. However, data from geostationary Earth Orbit Synthetic Aperture Radar (GEOSAR) platforms or airborne SAR system can overcome this limitation because of the possibility to direct the radar beam to different azimuths. One more difficulty of using InSAR in monitoring dams is that the arch shape of concrete dams could be challenging due to their complex structure. The arc shape of a dam may result in different levels of sensitivity to the deformation and also data with high spatial resolution may be required because the crown of arch dams is usually smaller than that of earthfill dam crest.

The relationship between the incidence angle of descending images from a platform heading (γ) with azimuth of -167˚, and the compression factor R, for a dam having an aspect orientation (α) of 195˚ and embankment slope (β) of 23.5˚ is illustrated in Figure 6.1c. It can be seen from this figure that large incidence angles lead to high compression factors and accordingly less distortion of the dam slope. Thus, if there is an option to select between two types of SAR datasets which have different incidence angles, it would be better to choose one with the largest incidence angle or at least choosing images in which the dam site is located in the far range of the image. For example, Darbandikhan dam is observed from four tracks of Sentinel-1 but it is located in the far range of the descending track 6. Therefore, only this track was selected to investigate the stability of the dam (see Figure 5.1). From Figure 6.1a-c, it is obvious that the specifications of radar images and the dam details should be investigated prior to conducting any monitoring using the InSAR technique.

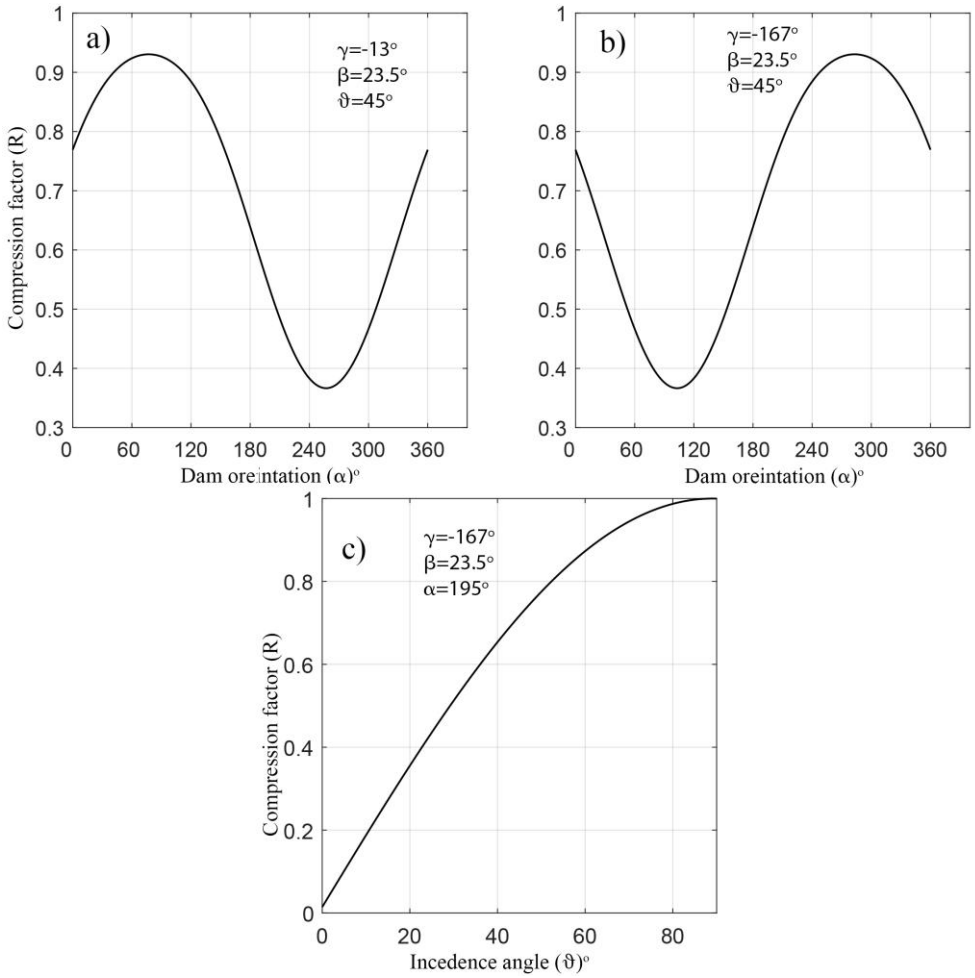

Figure 6.1. Considerations in selecting SAR data for dam monitoring: a-b) compression factor R on dam slope (β) of 23.5˚ when the incidence angle (ϑ) is 45˚ for both ascending (γ=-13) and descending (γ=-167) images respectively, plotted after Cigna et al. (2014); c) relationship between incidence angle and compression factor on descending images collected over a dam having slope of 23.5˚ and aspect oreintation (α) of 195˚.

One other important factor that should be considered is the temporal resolution of the SAR data. Interferograms with long temporal baseline separation would generally be preferable because they have a large signal-to-noise ratio (SNR). However, the temporal decorrelation in such interferograms can be problematic. Furthermore, if the dam exhibits localised deformation in which the displacement gradient is high, phase discontinuities could result in low phase coherence in the deformation area. Accordingly, in the presence of temporal decorrelation, especially in data from short wavelength radars such as x-band, this phase discontinuity can be inappropriately filtered during the spatial filtering that is performed prior to phase unwrapping. Therefore, the deformation signal may be underestimated particularly in those interferograms having a long temporal baseline. The gradient of fringe is proportional to radar wavelength. Therefore, when a deformed area observed with X-, C-, and L-band images having identical pixel size, the fringe gradient in the X-band images is denser than C- and L-band radar assuming identical pixel size.

In order to maximize the capability of InSAR for dam deformation monitoring the above-mentioned factors should be examined carefully.

6.3 Recommendations for future research

One of the major contributions of this work is to have demonstrated the ability to investigate the historical instability of large-scale dams using spaceborne SAR data. A further important point is that, with the freely available SAR data like those from Sentinel-1 this research has paved the way for the development of an automated dam monitoring web-based system for large dams at a global scale. This can contribute to mitigation of effort and cost devoted to monitoring dams by using conventional instruments. Such an outstanding service could be an effective tool for the early detection of the structural malfunctions in dams and to povide forcasts of catastrophic events.

The high temporal and spatial resolution of SAR data enable very accurate deformation maps to be generated rapidly in contrast to conventional monitoring data. Correlation analysis can be performed between displacement time series and water level (or other environment factors) to determine the triggering factor(s). Of course, this will help dam operators to control fluctuations in water levels so as to minimise the impacts on the dam structure. For newly constructed dams, the high temporal and spatial resolution deformation maps may help in effort to redistribute and/or densify the existing geodetic monitoring network according to the deformation pattern on the dam surface. Furthermore, a network of corner reflectors can be installed in deformed areas and their spatial distribution determined according to the results of this study. Also further work required to investigate the feasibility of using InSAR to identify horizontal movement and in monitoring other types and scales of dams, espicialy those with concrete structures, using higher resolution SAR data.

The following further research is recommended concerning the employment of InSAR for the monitoring of dams.

1) Exploiting further unwrapping algorithms to overcome the problem of phase discontinuity for rapid subsiding areas. One of the interesting research here is the development of 2D or 3D unwrapping algorithm following pixels with minimum foreshortening factor.
2) Establishing a web based service to monitor embankment dams using Sentinel-1 data.
3) Separating benign and critical movement of dams using InSAR time series. This can be carried out by using the model in Equation (4.8) in the SBAS timeseries instead of the linear model.

4) Using high spatial and temporal resolution SAR data for monitoring earthfill and concret dams to overcome the problems of high dispalcement gradients.

References

Al-Ansari, N., Adamo, N., Issa, I.E., Sissakian, V. and Knutsson, S. (2015) 'Mystery of Mosul dam the most dangerous dam in the world: karstification and sinkholes', *Journal of Earth Sciences and Geotechnical Engineering*, 5(3), pp. 33-45.

Al-Ansari, N. and Knutsson, S. (2011) 'Toward prudent management of water resources in Iraq', *Journal of Advanced Science and Engineering Research*, 1(1), pp. 53-67.

Al-Ansari, N.A. (2013) 'Management of water resources in iraq: Perspectives and prognoses', *Engineering*, 05(08), pp. 667-684.

Al-Saigh, N.H. and Al-Dabbagh, T.H. (2011) 'Ground stability assessment using geophysics and field observation techniques', *Environmental Earth Sciences*, 66(6), pp. 1597-1601.

Alabayachi, S. (2015) *Mosul dam report*. Iraq, Baghdad: Ministry of water resources resources, M.o.w. [Online]. Available at: http://www.alsabaah.iq/ArticleShow.aspx?ID=110749.

Alex, H.M.N.G., Linlin, G.E., Zhang, K., Chang, H.C., Li, X., Rizos, C. and Omura, M. (2011) 'Deformation mapping in three dimensions for underground mining using InSAR - Southern highland coalfield in New South Wales, Australia', *International Journal of Remote Sensing*, 32(22), pp. 7227-7256.

Almog, E., Kelham, P. and King, R. (2011) *Modes of dam failure and monitoring and measuring techniques* (978-1-84911-230-7). Bristol, United Kingdom: Environment Agency and DEFRA. [Online]. Available at: https://assets.publishing.service.gov.uk/government/uploads/system/uploads/attachment_data/file/290819/scho0811buaw-e-e.pdf (Accessed: 27-09-2018).

Alsinawi, S. and Ghalib, H. (1975) 'Historical seismicity of Iraq', *Bulletin of the Seismological Society of America* 65(5), pp. 541-547.

Anastasiadis, A., Klimis, N., Makra, K. and Margaris, B. (2004) 'On seismic behavior of a 130m high rockfill dam: An integrated approach', *13th World Conference on Earthquake Engineering*. Vancouver, B.C., Canada.

Anghel, A., Vasile, G., Boudon, R., d'Urso, G., Girard, A., Boldo, D. and Bost, V. (2016) 'Combining spaceborne SAR images with 3D point clouds for infrastructure monitoring applications', *ISPRS Journal of Photogrammetry and Remote Sensing*, 111, pp. 45-61.

Annunziato, A., Andredakis, I. and Probst, P. (2016) *Impact of Flood by a Possible Failure of the Mosul Dam*. Brussels, Belgium: Joint Research Centre Commission, E. [Online]. Available at: http://publications.jrc.ec.europa.eu/repository/bitstream/JRC101555/lbna27923enn.pdf (Accessed: 27-09-2018).

Arjona, A., Santoyo, M.Á., Fernández Torres, J., Monells Miralles, D., Prieto, J.F., Pallero, J., Prieto, E., Seco, A., Luzón, F. and Mallorquí Franquet, J.J. (2010) 'On the applicability of an advanced DInSAR technique near Itoiz and Yesa reservoirs, Navarra, Spain', *Proceedings of the workshop Fringe 2009*. Frascati, Italy, 30 November-4 December 2009. European Space Agency Publications Division. Available at: http://hdl.handle.net/10261/33880 (Accessed: 15-09-2018).

Auld, H., Maclver, D., Klaassen, J., Comer, N. and Tugwood, B. (2006) 'Planning for Atmospheric Hazards and Disaster Management Under Changing Climate Conditions', *2006 IEEE EIC Climate Change Conference*. Ottawa, Canada. IEEE.

Avallone, A., Cirella, A., Cheloni, D., Tolomei, C., Theodoulidis, N., Piatanesi, A., Briole, P. and Ganas, A. (2017) 'Near-source high-rate GPS, strong motion and InSAR observations to image the 2015 Lefkada (Greece) Earthquake rupture history', *Scientific Reports*, 7(1), p. 10358.

Baade, J. and Schmullius, C. (2016) 'TanDEM-X IDEM precision and accuracy assessment based on a large assembly of differential GNSS measurements in Kruger National Park, South Africa', *ISPRS Journal of Photogrammetry and Remote Sensing*, 119, pp. 496-508.
Bamler, R. (1992) 'A comparison of range-Doppler and wavenumber domain SAR focusing algorithms', *IEEE Transactions on Geoscience and Remote Sensing*, 30(4), pp. 706-713.
Bamler, R. and Hartl, P. (1998) 'Synthetic aperture radar interferometry', *Inverse Problems*, 14(4), pp. R1-R54.
Baran, I., Stewart, M.P., Kampes, B.M., Perski, Z. and Lilly, P. (2003) 'A modification to the Goldstein radar interferogram filter', *IEEE Transactions on Geoscience and Remote Sensing*, 41(9), pp. 2114-2118.
BBC News Asia (2018) *Laos dam collapse: race to rescue flooded villagers* [News]. Available at: https://www.bbc.co.uk/news/world-asia-44947185.
BBC News Middle East (2017) 'Iran-Iraq earthquake: Hundreds killed as border region hit', *BBC News Middle East*edn). [Online] Available at: http://www.bbc.co.uk/news/world-middle-east-41963373 (Accessed: 12/07/2018).
Beauducel, F., Briole, P. and Froger, J.-L. (2000) 'Volcano-wide fringes in ERS synthetic aperture radar interferograms of Etna (1992–1998): Deformation or tropospheric effect?', *Journal of Geophysical Research: Solid Earth*, 105(B7), pp. 16391-16402.
Berardino, P., Fornaro, G., Lanari, R. and Sansosti, E. (2002) 'A new algorithm for surface deformation monitoring based on small baseline differential SAR interferograms', *IEEE Transactions on Geoscience and Remote Sensing*, 40(11), pp. 2375-2383.
Berga, L. (1998) *Dam Safety*. Barcelona, Spain: Rotterdam: Balkema.
Bills, B.G. and Ferrari, A.J. (1977) 'A harmonic analysis of lunar topography', *Icarus*, 31(2), pp. 244-259.
Blanco-Sánchez, P., Mallorquí, J.J., Duque, S. and Monells, D. (2008) 'The coherent pixels technique (CPT): an advanced DInSAR technique for nonlinear deformation monitoring', *Pure and Applied Geophysics*, 165(6), pp. 1167-1193.
Blom, R., Fielding, E., Gabriel, A. and Goldstein, R. (1999) 'Radar interferometry for monitoring of oil fields and dams: Lost Hills, California and Aswan, Egypt', *National Geological Society of America Meeting*. Denver, United States, 1999-10-25. Pasadena, CA, United States: Jet Propulsion Lab., California Inst. of Tech. Available at: http://hdl.handle.net/2014/17775 (Accessed: 27-09-2018).
Bowen, S.W. (2007) *Relief and Reconstruction Funded Work at Mosul Dam* (SIGIR PA-07-105). Reconstruction, O.o.t.S.I.G.f.I. [Online]. Available at: http://cybercemetery.unt.edu/archive/sigir/20131001121159/http:/www.sigir.mil/files/assessments/PA-07-105.pdf) (Accessed: 04-07-2016).
Bozzano, F., Cipriani, I., Mazzanti, P. and Prestininzi, A. (2011) 'Displacement patterns of a landslide affected by human activities: insights from ground-based InSAR monitoring', *Natural Hazards*, 59(3), pp. 1377-1396.
Bozzano, F., Esposito, C., Franchi, S., Mazzanti, P., Perissin, D., Rocca, A. and Romano, E. (2015) 'Analysis of a Subsidence Process by Integrating Geological and Hydrogeological Modelling with Satellite InSAR Data', in *Engineering Geology for Society and Territory-Volume 5*. Switzerland: Springer, pp. 155-159.
British Dam Society (2017) 'The British Dam Society is an Associated Society of the Institution of Civil Engineers', *British DAm Society*. Available at: http://www.britishdams.org/ (Accessed: 6 December 2017).
Bürgmann, R., Rosen, P.A. and Fielding, E.J. (2000) 'Synthetic Aperture Radar Interferometry to measure Earth's surface topography and its deformation', *Annual Review of Earth and Planetary Sciences*, 28(1), pp. 169-209.
Charles, J. (1986) 'The significance of problems and remedial works at British earth dams', *Proceedings of BNCOLD/IWES Conference on Reservoirs*. Institution of Civil Engineers London, pp. 123-141.

Chen, C.W. and Zebker, H.A. (2000) 'Network approaches to two-dimensional phase unwrapping: intractability and two new algorithms', *Journal of the Optical Society of America A*, 17(3), p. 401.

Chen, C.W. and Zebker, H.A. (2001) 'Two-dimensional phase unwrapping with use of statistical models for cost functions in nonlinear optimization', *Journal of the Optical Society of America A, Optics Image, Science and Vision*, 18(2), pp. 338-351.

Chen, M., Tomás, R., Li, Z., Motagh, M., Li, T., Hu, L., Gong, H., Li, X., Yu, J. and Gong, X. (2016) 'Imaging Land Subsidence Induced by Groundwater Extraction in Beijing (China) Using Satellite Radar Interferometry', *Remote Sensing*, 8(6), p. 468.

Cigna, F., Bateson, L.B., Jordan, C.J. and Dashwood, C. (2014) 'Simulating SAR geometric distortions and predicting Persistent Scatterer densities for ERS-1/2 and ENVISAT C-band SAR and InSAR applications: nationwide feasibility assessment to monitor the landmass of Great Britain with SAR imagery', *Remote Sensing of Environment*, 152, pp. 441-466.

Clements, R. (1983) 'Post-Construction Deformation Of Rockfill Dams', *Jurnal of geotechnical engineering*, 110.

Coffman, R.A. (2009) *Processing of synthetic aperture radar data as applied to the characterization of localized deformation features*. Ph.D (unpubl.) thesis. University of Missouri-Columbia.

Cordell, M.C. (2006) *Dokan and Derbendikhan Dam Inspections*. Malvern East, Australia: World Bank., SMEC International Pty. Ltd. [Online]. Available at: http://documents.worldbank.org/curated/en/846331468044054012/E15370Dokan0an1am0Inspection0Report.doc.

Costantini, M. (1998) 'A novel phase unwrapping method based on network programming', *IEEE Transactions on Geoscience and Remote Sensing*, 36(3), pp. 813-821.

Crosetto, M. (2002) 'Subsidence monitoring using SAR interferometry: reduction of the atmospheric effects using stochastic filtering', *Geophysical Research Letters*, 29(9).

Cusack, R. and Papadakis, N. (2002) 'New robust 3-D phase unwrapping algorithms: application to magnetic field mapping and undistorting echoplanar images', *NeuroImage*, 16(3), pp. 754-764.

Dai, F.C., Lee, C.F., Deng, J.H. and Tham, L.G. (2005) 'The 1786 earthquake-triggered landslide dam and subsequent dam-break flood on the Dadu River, southwestern China', *Geomorphology*, 65(3-4), pp. 205-221.

Dai, K., Li, Z., Tomás, R., Liu, G., Yu, B., Wang, X., Cheng, H., Chen, J. and Stockamp, J. (2016) 'Monitoring activity at the Daguangbao mega-landslide (China) using Sentinel-1 TOPS time series interferometry', *Remote Sensing of Environment*, 186, pp. 501-513.

Dai, K., Liu, G., Li, Z., Li, T., Yu, B., Wang, X. and Singleton, A. (2015) 'Extracting vertical displacement rates in Shanghai (China) with multi-platform SAR images', *Remote Sensing*, 7(8), p. 9542.

Darvishi, M., Schlögel, R., Bruzzone, L. and Cuozzo, G. (2018) 'Integration of PSI, MAI, and intensity-based sub-pixel offset tracking results for landslide monitoring with x-band corner reflectors—Italian Alps (corvara)', *Remote Sensing*, 10(3), p. 409.

De Zan, F. and Guarnieri, A.M. (2006) 'TOPSAR: Terrain observation by progressive scans', *IEEE Transactions on Geoscience and Remote Sensing*, 44(9), pp. 2352-2360.

Deledalle, C.A., Denis, L. and Tupin, F. (2011) 'NL-InSAR: Nonlocal interferogram estimation', *IEEE Transactions on Geoscience and Remote Sensing*, 49(4), pp. 1441-1452.

Di Martire, D., Iglesias, R., Monells, D., Centolanza, G., Sica, S., Ramondini, M., Pagano, L., Mallorquí, J.J. and Calcaterra, D. (2014) 'Comparison between differential SAR interferometry and ground measurements data in the displacement monitoring of the earth-dam of Conza della Campania (Italy)', *Remote Sensing of Environment*, 148, pp. 58-69.

Di Traglia, F., Intrieri, E., Nolesini, T., Bardi, F., Del Ventisette, C., Ferrigno, F., Frangioni, S., Frodella, W., Gigli, G., Lotti, A., Stefanelli, C.T., Tanteri, L., Leva, D. and Casagli, N. (2014) 'The ground-based InSAR monitoring system at Stromboli volcano: linking changes in displacement rate and intensity of persistent volcanic activity', *Bulletin of Volcanology*, 76(2).

Doin, M.P., Lasserre, C., Peltzer, G., Cavalié, O. and Doubre, C. (2009) 'Corrections of stratified tropospheric delays in SAR interferometry: validation with global atmospheric models', *Journal of Applied Geophysics*, 69(1), pp. 35-50.

El-Gharbawi, T. and Tamura, M. (2014) 'Measuring deformations using SAR interferometry and GPS observables with geodetic accuracy: application to Tokyo, Japan', *ISPRS Journal of Photogrammetry and Remote Sensing*, 88, pp. 156-165.

Emadali, L., Motagh, M. and Haghshenas Haghighi, M. (2017) 'Characterizing post-construction settlement of the Masjed-Soleyman embankment dam, Southwest Iran, using TerraSAR-X SpotLight radar imagery', *Engineering Structures*, 143, pp. 261-273.

Emardson, T.R. (2003) 'Neutral atmospheric delay in interferometric synthetic aperture radar applications: Statistical description and mitigation', *Journal of Geophysical Research*, 108(B5).

Esri *DigitalGlobe [basemap]*, Scale Not Given. *World Imagery* [Online] Available at: http://www.arcgis.com/home/webmap/viewer.html?useExisting=1&layers=10df2279f9684e4a9f6a7f08febac2a9 (Accessed: 12-07-2017).

Ezz-Aldeen, M., Al-Ansari, N. and Knutsson, S. (2013) 'Application of SWAT model to estimate the sediment load from the left bank of Mosul Dam', *Journal of Advanced Science and Engineering Research*, 3(1), pp. 47-61.

Farr, T.G., Rosen, P.A., Caro, E., Crippen, R., Duren, R., Hensley, S., Kobrick, M., Paller, M., Rodriguez, E., Roth, L., Seal, D., Shaffer, S., Shimada, J., Umland, J., Werner, M., Oskin, M., Burbank, D. and Alsdorf, D. (2007) 'The shuttle radar topography mission', *Reviews of Geophysics*, 45(2), pp. n/a-n/a.

Fattahi, H. and Amelung, F. (2013) 'DEM error correction in InSAR time series', *IEEE Transactions on Geoscience and Remote Sensing*, 51(7), pp. 4249-4259.

Ferretti, A. (2014) *Satellite InSAR Data. Reservoir Monitoring from Space*. Milan, Italy: The European Association of Geoscientists and Engineers.

Ferretti, A., Fumagalli, A., Novali, F., Prati, C., Rocca, F. and Rucci, A. (2011) 'A new algorithm for processing interferometric data-stacks: SqueeSAR', *IEEE Transactions on Geoscience and Remote Sensing*, 49(9), pp. 3460-3470.

Ferretti, A., Monti-Guarnieri, A., Prati, C., Rocca, F. and Massonet, D. (2007) *InSAR Principles: Guidelines for SAR Interferometry Processing and Interpretation*. Noordwijk, The Netherlands: ESA Publications.

Ferretti, A., Monti Guarnieri, A., Prati, C. and Rocca, F. (1997a) 'Multi baseline interferometric techniques and applications', *European Space Agency, (Special Publication) ESA SP*, (406), pp. 243-252.

Ferretti, A., Prati, C. and Rocca, F. (2000) 'Nonlinear subsidence rate estimation using permanent scatterers in differential SAR interferometry', *IEEE Transactions on Geoscience and Remote Sensing*, 38(5), pp. 2202-2212.

Ferretti, A., Prati, C. and Rocca, F. (2001) 'Permanent scatterers in SAR interferometry', *IEEE Transactions on Geoscience and Remote Sensing*, 39(1), pp. 8-20.

Ferretti, A., Prati, C., Rocca, F., Casagli, N., Farina, P. and Young, B. (2005) 'Permanent Scatterers technology: a powerful state of the art tool for historic and future monitoring of landslides and other terrain instability phenomena', *Proceeding of 2005 International Conference on Landslide Risk Management.* . Balkema, Vancouver, Canada.

Ferretti, A., Prati, C., Rocca, F. and Monti Guarnieri, A. (1997b) 'Multibaseline SAR interferometry for automatic DEM reconstruction (DEM)', *3rd ERS Symposium on Space*

at the service of our Environment. Florence, Italy, September 1997. European Space Agency, p. 1809.
Fialko, Y., Simons, M. and Agnew, D. (2001) 'The complete (3-D) surface displacement field in the epicentral area of the 1999 Mw7. 1 Hector Mine earthquake, California, from space geodetic observations', *Geophysical Research Letters*, 28(16), pp. 3063-3066.
Ford, D.C. (1988) 'Landform Development Karst', in *The geology of North America*. The Geological society of America.
Franceschetti, G. and Lanari, R. (1999) *Synthetic Aperture Radar Processing*. Washington, D.C, USA: CRC press.
Fringe (2017) *FRINGE2017_Sorted_Recommendations*. Available at: http://fringe.esa.int/ (Accessed: 06/11/2018).
Fujiwara, S., Yarai, H., Ozawa, S., Tobita, M., Murakami, M., Nakagawa, H., Nitta, K., Rosen, P.A. and Werner, C.L. (1998) 'Surface displacement of the March 26, 1997 Kagoshima-Ken-Hokuseibu earthquake in Japan from synthetic aperture radar interferometry', *Geophysical Research Letters*, 25(24), pp. 4541-4544.
Gabriel, A.K. and Goldstein, R.M. (1988) 'Cover Radar interferogram made from two passes of SIR-B over the Rocky Mountains in British Columbia, Canada', *International Journal of Remote Sensing*, 9(5), pp. 835-835.
Gabriel, A.K., Goldstein, R.M. and Zebker, H.A. (1989) 'Mapping small elevation changes over large areas: Differential radar interferometry', *Journal of Geophysical Research: Solid Earth*, 94(B7), pp. 9183-9191.
Ganas, A., Kourkouli, P., Briole, P., Moshou, A., Elias, P. and Parcharidis, I. (2018) 'Coseismic displacements from moderate-size earthquakes mapped by Sentinel-1 differential interferometry: the case of February 2017 Gulpinar earthquake sequence (Biga Peninsula, Turkey)', *Remote Sensing*, 10(7), p. 1089.
Gatelli, F., Guamieri, A.M., Parizzi, F., Pasquali, P., Prati, C. and Rocca, F. (1994a) 'The wavenumber shift in SAR interferometry', *IEEE Transactions on Geoscience and Remote Sensing*, 32(4), pp. 855-865.
Gatelli, F., Monti Guamieri, A., Parizzi, F., Pasquali, P., Prati, C. and Rocca, F. (1994b) 'The wavenumber shift in SAR interferometry', *IEEE Transactions on Geoscience and Remote Sensing*, 32(4), pp. 855-865.
Gelautz, M., Frick, H., Raggam, J., Burgstaller, J. and Leberl, F. (1998) 'SAR image simulation and analysis of Alpine terrain', *ISPRS Journal of Photogrammetry and Remote Sensing*, 53(1), pp. 17-38.
Gens, R. and Van Genderen, J.L. (2007) 'SAR interferometry: issues, techniques, applications', *International Journal of Remote Sensing*, 17(10), pp. 1803-1835.
Ghiglia, D.C. and Pritt, M.D. (1998) *Two-Dimensional Phase Unwrapping: Theory, Algorithms, and Software*. New York: Wiley.
Goldstein, R. (1995) 'Atmospheric limitations to repeat-track radar interferometry', *Geophysical Research Letters*, 22(18), pp. 2517-2520.
Goldstein, R., Zebker, H. and Werner, C. (1988) 'Satellite radar interferometry: two-dimensional phase unwrapping', *Radio Science*, 23(4), pp. 713-720.
Goldstein, R.M. and Werner, C.L. (1998) 'Radar interferogram filtering for geophysical applications', *Geophysical Research Letters*, 25(21), pp. 4035-4038.
Gourmelen, N., Amelung, F. and Lanari, R. (2010) 'Interferometric synthetic aperture radar–GPS integration: interseismic strain accumulation across the Hunter Mountain fault in the eastern California shear zone', *Journal of Geophysical Research*, 115(B9).
Graham, L.C. (1974) 'Synthetic interferometer radar for topographic mapping', *Proceedings of the IEEE*, 62(6), pp. 763-768.
Grenerczy, G. and Wegmüller, U. (2011) 'Persistent scatterer interferometry analysis of the embankment failure of a red mud reservoir using ENVISAT ASAR data', *Natural Hazards*, 59(2), p. 1047.

Gutiérrez, F., Desir, G. and Gutiérrez, M. (2003) 'Causes of the catastrophic failure of an earth dam built on gypsiferous alluvium and dispersive clays (Altorricón, Huesca Province, NE Spain)', *Environmental Geology*, 43(7), pp. 842-851.

Hammond, W., Lib, Z., Plaga, H., Kreemera, C. and Blewitta, G. (2010) 'Integrated INSAR and GPS studies of crustal deformation in the Western Great Basin, Western United States', *International Archives of the Photogrammetry, Remote Sensing and Spatial Information Science*, 38(Part 8), pp. 39-43.

Hanssen, R.F. (1998) *Atmospheric Heterogeneities In ERS Tandem SAR Interferometry*. Delft, The Netherlands: Delft University Press.

Hanssen, R.F. (2001) *Radar Interferometry: Data Interpretation and Error Analysis*. Boston: MA: Kluwer Academic.

Hanssen, R.F. and van Leijen, F.J. (2008) 'Monitoring water defense structures using radar interferometry', *2008 IEEE Radar Conference*. Rome, Italy. Rome, Italy: IEEE, pp. 1-4. Available at: https://ieeexplore.ieee.org/document/4720874 (Accessed: 27-09-2018).

Hassan, R., Al-Ansari, N., Ali, A.A., Ali, S.S. and Knutsson, S. (2017) 'Bathymetry and siltation rate for Dokan Reservoir, Iraq', *Lakes and Reservoirs: Research and Management*, 22(2), pp. 179-189.

Herndon, r.l. (1990) *Settlement analysis*. Washington, DC 20314-1000: U.S. Army Corps of Engineers.

Honda, K., Nakanishi, T., Haraguchi, M., Mushiake, N., Iwasaki, T., Satoh, H., Kobori, T. and Yamaguchi, Y. (2012) 'Application of exterior deformation monitoring of dams by DInSAR analysis using ALOS PALSAR', *2012 IEEE International Geoscience and Remote Sensing Symposium*. Munich, Germany, 22-27 July 2012. IEEE, pp. 6649-6652. Available at: https://ieeexplore.ieee.org/document/6352074 (Accessed: 28-09-2018).

Hooper, A., Bekaert, D., Spaans, K. and Arikan, M. (2012) 'Recent advances in SAR interferometry time series analysis for measuring crustal deformation', *Tectonophysics*, 514-517, pp. 1-13.

Hooper, A., Segall, P. and Zebker, H. (2007) 'Persistent scatterer interferometric synthetic aperture radar for crustal deformation analysis, with application to Volcán Alcedo, Galápagos', *Journal of Geophysical Research: Solid Earth*, 112(7).

Hooper, A., Zebker, H., Segall, P. and Kampes, B. (2004) 'A new method for measuring deformation on volcanoes and other natural terrains using InSAR persistent scatterers', *Geophysical Research Letters*, 31(23), pp. 1-5.

Hooper, A. and Zebker, H.A. (2007) 'Phase unwrapping in three dimensions with application to InSAR time series', *Journal of the Optical Society of America A*, 24(9), pp. 2737-2747.

Hooper, A.J. (2008) 'A multi-temporal InSAR method incorporating both persistent scatterer and small baseline approaches', *Geophysical Research Letters*, 35(16).

Hunter, G. and Fell, R. (2003) *The deformation behaviour of embankment dams*. University of New South Wales, School of Civil and Environmental Engineering.

Huntley, J.M. (2001) 'Three-dimensional noise-immune phase unwrapping algorithm', *Applied Optics*, 40(23), p. 3901.

ICOLD (2005) *Dam foundations. Geologic considerations. Investigation methods.Treatment. Monitoring*. ICOLD, Paris: International Commission on Large Dams.

Issa, I.E. (2013) 'Changes in bed morphology of Mosul dam reservoir', *Journal of Advanced Science and Engineering Research*, 3, pp. 86-95.

Issa, I.E., Al-Ansari, N. and Knutsson, S. (2013) 'Sedimentation and new operational curves for Mosul Dam, Iraq', *Hydrological Sciences Journal*, 58(7), pp. 1456-1466.

Jansen, R.B. (1983) *Dams and Public Safety (a Water Resources Technical Publication)*. United States Government Printing Office: U.S. Department of the Interior, Bureau of Reclamation Interior, U.S.D.

Jansen, R.B., Parrett, N.F. and Ingram, D.E. (1995) *Safety evaluation of existing dams*. Denever, Colorado: United Department of the Interior Bureau of Reclamation.

Jaradat, A.A. (2002) *Agriculture in Iraq: Resources, Potentials, Constraints, and Research Needs and Priorities*. Washington, D. C., USA: Agriculture, D.o.S.M.E.W.G.o. [Online]. Available at: https://www.ars.usda.gov/ARSUserFiles/50600000/Products-Reprints/2002/1107.pdf.

Jassim, S.Z., Jibril, A.S. and Numan, N.M.S. (1997) 'Gypsum karstification in the Middle Miocene Fatha Formation, Mosul area, northern Iraq', *Geomorphology*, 18(2), pp. 137-149.

Jassim, S.Z., Raiswell, R. and Bottrell, S.H. (1999) 'Genesis of the Middle Miocene stratabound sulphur deposits of northern Iraq', *Journal of the Geological Society*, 156(1), pp. 25-39.

Johnston, T., Millmore, J., Charles, J. and Tedd, P. (1990) *An Engineering Guide to the Safety of Embankment Dams in the United Kingdom*. Watford, UK: Building Research.

Jordan, R. (1980) 'The Seasat-A synthetic aperture radar system', *IEEE Journal of Oceanic Engineering*, 5(2), pp. 154-164.

Kalkan, Y., Potts, L.V. and Bilgi, S. (2016) 'Assessment of Vertical Deformation of the Ataturk Dam Using Geodetic Observations', *Journal of Surveying Engineering*, 142(2), p. 04015011.

Kelley, J.R., Wakeley, L.D., Broadfoot, S.W., Pearson, M.L., McGrath, C.A., McGill, T.E., Jorgeson, J.D. and Talbot, C.A. (2007) *Geologic Setting of Mosul Dam and Its Engineering Implications*. Bloomington, USA: U.S. Army Engineer Research and Development Center. [Online]. Available at: https://www.globalsecurity.org/military/library/report/2007/tr07-10.pdf (Accessed: 14-06-2016).

Khakim, M.Y.N., Tsuji, T. and Matsuoka, T. (2013) 'Detection of localized surface uplift by differential SAR interferometry at the Hangingstone Oil Sand Field, Alberta, Canada', *IEEE Journal of Selected Topics in Applied Earth Observations and Remote Sensing*, 6(6), pp. 2344-2354.

King, M.D. (2016) 'The Weaponization of Water in Syria and Iraq', *The Washington Quarterly*, 38(4), pp. 153-169.

Krieger, G., Moreira, A., Fiedler, H., Hajnsek, I., Werner, M., Younis, M. and Zink, M. (2007) 'TanDEM-X: A satellite formation for high-resolution SAR interferometry', *IEEE Transactions on Geoscience and Remote Sensing*, 45(11), pp. 3317-3341.

Lanari, R., Casu, F., Manzo, M., Zeni, G., Berardino, P., Manunta, M. and Pepe, A. (2007) 'An overview of the Small BAseline Subset algorithm: a DInSAR technique for surface deformation analysis', *Pure and Applied Geophysics*, 164(4), pp. 637-661.

Lanari, R., Lundgren, P., Manzo, M. and Casu, F. (2004a) 'Satellite radar interferometry time series analysis of surface deformation for Los Angeles, California', *Geophysical Research Letters*, 31(23), pp. n/a-n/a.

Lanari, R., Mora, O., Manunta, M., Mallorqui, J.J., Berardino, P. and Sansosti, E. (2004b) 'A small-baseline approach for investigating deformations on full-resolution differential SAR interferograms', *IEEE Transactions on Geoscience and Remote Sensing*, 42(7), pp. 1377-1386.

Larsen, Y., Engen, G., Lauknes, T.R., Malnes, E. and Høgda, K.A. (2005) 'A Generic Differential Interferometric SAR Processing system, With Applications To Land Subsidence and Snow-Water Equivalent Retrieval', *Fringe 2005 Workshop*. Frascati, Italy, 28 November -2 December 2005. European Space Agency. Available at: http://earth.esa.int/cgi-bin/conffringe7785.html?abstract=427.

Lazecky, M., Perissin, D., Lei, L., Qin, Y. and Scaioni, M. (2013) 'Plover Cove dam monitoring with spaceborne InSAR technique in Hong Kong', *The 2nd Joint International Symposium on Deformation Monitoring*. Nottingham, United Kingdom, 9-10 September 2013. Nottingham, United Kingdom: FIG, pp. 9-11. Available at: http://www.academia.edu/5092206/Plover_Cove_Dam_Monitoring_with_Spaceborne_InSAR_Technique_in_Hong_Kong.

Lazecký, M., Perissin, D., Zhiying, W., Ling, L. and Yuxiao, Q. (2015) 'Observing dam's movements with spaceborne sar interferometry', in *Engineering Geology for Society and Territory - Volume 5: Urban Geology, Sustainable Planning and Landscape Exploitation*. Switzerland 2015: Springer International Publishing, pp. 131-136.

Levanon, N. (1988) *Radar Principles*. New York, Wiley-Interscience: Wiley.

Li, F.-K., Croft, C. and Held, D.N. (1983) 'Comparison of several techniques to obtain Multiple-Look SAR imagery', *IEEE Transactions on Geoscience and Remote Sensing*, GE-21(3), pp. 370-375.

Li, F.K. and Goldstein, R.M. (1990) 'Studies of multibaseline spaceborne interferometric synthetic aperture radars', *IEEE Transactions on Geoscience and Remote Sensing*, 28(1), pp. 88-97.

Li, Z.-w., Ding, X.-l., Zhu, J.-j. and Zou, Z.-r. (2005) 'Quantitative study of atmospheric effects in spaceborne InSAR measurements', *Journal of Central South University of Technology*, 12(4), pp. 494-498.

Li, Z. (2003) 'Comparison of precipitable water vapor derived from radiosonde, GPS, and Moderate-Resolution Imaging Spectroradiometer measurements', *Journal of Geophysical Research*, 108(D20).

Li, Z. (2005a) *Correction of atmospheric water vapour effects on repeat-pass SAR interferometry using GPS, MODIS and MERIS data*. University of London.

Li, Z. (2005b) 'Interferometric synthetic aperture radar (InSAR) atmospheric correction: GPS, Moderate Resolution Imaging Spectroradiometer (MODIS), and InSAR integration', *Journal of Geophysical Research*, 110(B3).

Li, Z., Fielding, E.J., Cross, P. and Muller, J.-P. (2006a) 'Interferometric synthetic aperture radar atmospheric correction: GPS topography-dependent turbulence model', *Journal of Geophysical Research: Solid Earth*, 111(B2).

Li, Z., Fielding, E.J., Cross, P. and Muller, J.P. (2006b) 'Interferometric synthetic aperture radar atmospheric correction: Medium Resolution Imaging Spectrometer and Advanced Synthetic Aperture Radar integration', *Geophysical Research Letters*, 33(6).

Li, Z., Yu, C., Chen, J. and Penna, N.T. (2018) 'Temporal correlation of atmospheric delay and its mitigation in InSAR time series' *EGU General Assembly 2018*. 2018. Veinna, Austria. Available at: https://meetingorganizer.copernicus.org/EGU2018/EGU2018-14158.pdf.

Li, Z.H., Fielding, E.J. and Cross, P. (2009) 'Integration of InSAR Time-Series analysis and water-vapor correction for mapping postseismic motion after the 2003 Bam (Iran) earthquake', *IEEE Transactions on Geoscience and Remote Sensing*, 47(9), pp. 3220-3230.

Li, Z.W., Ding, X.L., Huang, C., Wadge, G. and Zheng, D.W. (2006c) 'Modeling of atmospheric effects on InSAR measurements by incorporating terrain elevation information', *Journal of Atmospheric and Solar-Terrestrial Physics*, 68(11), pp. 1189-1194.

Li, Z.W., Ding, X.L., Huang, C., Zhu, J.J. and Chen, Y.L. (2008) 'Improved filtering parameter determination for the Goldstein radar interferogram filter', *ISPRS Journal of Photogrammetry and Remote Sensing*, 63(6), pp. 621-634.

Li, Z.W., Yang, Z.F., Zhu, J.J., Hu, J., Wang, Y.J., Li, P.X. and Chen, G.L. (2015) 'Retrieving three-dimensional displacement fields of mining areas from a single InSAR pair', *Journal of Geodesy*, 89(1), pp. 17-32.

Liao, M., Wang, T., Lu, L., Zhou, W. and Li, D. (2007) 'Reconstruction of DEMs From ERS-1/2 Tandem Data in Mountainous Area Facilitated by SRTM Data', *IEEE Transactions on Geoscience and Remote Sensing*, 45(7), pp. 2325-2335.

Liu, P., Li, Q., Li, Z., Hoey, T., Liu, Y. and Wang, C. (2015) 'Land Subsidence over Oilfields in the Yellow River Delta', *Remote Sensing*, 7(2), pp. 1540-1564.

Loffeld, O., Nies, H., Knedlik, S. and Yu, W. (2008) 'Phase unwrapping for SAR interferometry: A Data Fusion Approach by Kalman Filtering', *IEEE Transactions on Geoscience and Remote Sensing*, 46(1), pp. 47-58.

Lu, Z. and Dzurisin, D. (2014) *InSAR Imaging of Aleutian Volcanoes*. Chichester, UK: Springer.

Marinkovic, P.L., Y (2013) 'Consequences of long-term ASAR local oscillator frequency decay - an empirical study of 10 years of data '. Norut, Norwa: Northern Research Institute. Available at: https://norut.no/en/publications/consequences-long-term-asar-local-oscillator-frequency-decay-empirical-study-10-years.

Massonnet, D. and Feigl, K. (1998a) 'Radar interferometry and its application to changes in the earth's surface', *Reviews of Geophysics*, 36(4), pp. 441-500.

Massonnet, D., Feigl, K., Rossi, M. and Adragna, F. (1994) 'Radar interferometric mapping of deformation in the year after the Landers earthquake', *Nature*, 369(6477), pp. 227-230.

Massonnet, D. and Feigl, K.L. (1995) 'Discrimination of geophysical phenomena in satellite radar interferograms', *Geophysical research letters*, 22(12), pp. 1537-1540.

Massonnet, D. and Feigl, K.L. (1998b) 'Radar interferometry and its application to changes in the Earth's surface'.

Michoud, C., Baumann, V., Lauknes, T.R., Penna, I., Derron, M.-H. and Jaboyedoff, M. (2016) 'Large slope deformations detection and monitoring along shores of the Potrerillos dam reservoir, Argentina, based on a small-baseline InSAR approach', *Landslides*, 13(3), pp. 451-465.

Milillo, P., Bürgmann, R., Lundgren, P., Salzer, J., Perissin, D., Fielding, E., Biondi, F. and Milillo, G. (2016a) 'Space geodetic monitoring of engineered structures: the ongoing destabilization of the Mosul dam, Iraq', *Scientific Reports*, 6, p. 37408.

Milillo, P., Perissin, D., Salzer, J.T., Lundgren, P., Lacava, G., Milillo, G. and Serio, C. (2016b) 'Monitoring dam structural health from space: insights from novel InSAR techniques and multi-parametric modeling applied to the Pertusillo dam Basilicata, Italy', *International Journal of Applied Earth Observation and Geoinformation*, 52, pp. 221-229.

Milillo, P., Porcu, M.C., Lundgren, P., Soccodato, F., Salzer, J., Fielding, E., Burgmann, R., Milillo, G., Perissin, D. and Biondi, F. (2017) 'The ongoing destabilization of the Mosul dam as observed by synthetic aperture radar interferometry', *2017 IEEE International Geoscience and Remote Sensing Symposium (IGARSS)*. Fort Worth, TX, USA. Fort Worth, TX, USA: IEEE, pp. 6279-6282. Available at: https://ieeexplore.ieee.org/document/8128442 (Accessed: 27-09-2018).

Mora, O., Lanari, R., Mallorquí, J., Berardino, P. and Sansosti, E. (2002) 'A new algorithm for monitoring localized deformation phenomena based on small baseline differential SAR interferograms', *IEEE International Geoscience and Remote Sensing Symposium*. Toronto, Ontario, Canada. IEEE, pp. 1237-1239.

Mora, O., Mallorqui, J.J. and Broquetas, A. (2003) 'Linear and nonlinear terrain deformation maps from a reduced set of interferometric sar images', *IEEE Transactions on Geoscience and Remote Sensing*, 41(10), pp. 2243-2253.

Motagh, M., Schurr, B., Anderssohn, J., Cailleau, B., Walter, T.R., Wang, R. and Villotte, J.-P. (2010) 'Subduction earthquake deformation associated with 14 November 2007, Mw 7.8 Tocopilla earthquake in Chile: Results from InSAR and aftershocks', *Tectonophysics*, 490(1-2), pp. 60-68.

Motagh, M., Shamshiri, R., Haghshenas Haghighi, M., Wetzel, H.-U., Akbari, B., Nahavandchi, H., Roessner, S. and Arabi, S. (2017) 'Quantifying groundwater exploitation induced subsidence in the Rafsanjan plain, southeastern Iran, using InSAR time-series and in situ measurements', *Engineering Geology*, 218, pp. 134-151.

Motagh, M., Walter, T.R., Sharifi, M.A., Fielding, E., Schenk, A., Anderssohn, J. and Zschau, J. (2008) 'Land subsidence in Iran caused by widespread water reservoir overexploitation', *Geophysical Research Letters*, 35(16).

Motagh, M., Wetzel, H.-U., Roessner, S. and Kaufmann, H. (2013) 'A TerraSAR-X InSAR study of landslides in southern Kyrgyzstan, Central Asia', *Remote Sensing Letters*, 4(7), pp. 657-666.

Neelmeijer, J., Motagh, M. and Bookhagen, B. (2017) 'High-resolution digital elevation models from single-pass TanDEM-X interferometry over mountainous regions: a case study of Inylchek Glacier, Central Asia', *ISPRS Journal of Photogrammetry and Remote Sensing*, 130(Supplement C), pp. 108-121.

Newmark, N.M. (1965) 'Effects of earthquakes on dams and embankments', *Géotechnique*, 15(2), pp. 139-160.

Onn, F. and Zebker, H. (2006) 'Correction for interferometric synthetic aperture radar atmospheric phase artifacts using time series of zenith wet delay observations from a GPS network', *Journal of Geophysical Research: Solid Earth (1978–2012)*, 111(B9).

Oppenheim, A.V., Willsky, A.S. and Young, I.T. (1983) *Signals and Systems*. London, UK: Prentice-Hall International.

Oscar, D. and ASCE, M. (1987) 'Post-Construction Deformation of Rockfill Dams', *Journal of Geotechnical Engineering*, Vol. 113(Issue 1 (January 1987)).

Patri, C. and Rocca, F. (1992) 'Range resolution enhancement with multiple sar surveys combination', *92 International Geoscience and Remote Sensing Symposium*. Houston, TX, USA, 26-29 May 1992. IEEE, pp. 1576-1578. Available at: http://ieeexplore.ieee.org/ielx2/1014/12511/00578637.pdf?tp=&arnumber=578637&isnumber=12511.

Perissin, D. and Ferretti, A. (2007) 'Urban-Target Recognition by Means of Repeated Spaceborne SAR Images', *IEEE Transactions on Geoscience and Remote Sensing*, 45(12), pp. 4043-4058.

Perissin, D., Wang, Z. and Teng, W. (2011) 'The SARPROZ InSAR tool for urban subsidence/manmade structure stability monitoring in

China', *Proceedings of 34th International Symposium for Remote Sensing of the Environment (ISRSE)*. Sydney, Australia, January, 2011.

Polcari, M., Palano, M., Fernández, J., Samsonov, S.V., Stramondo, S. and Zerbini, S. (2017) '3D displacement field retrieved by integrating Sentinel-1 InSAR and GPS data: the 2014 South Napa earthquake', *European Journal of Remote Sensing*, 49(1), pp. 1-13.

Prati, C., Rocca, F., Guarnieri, A.M. and Pasquali, P. (1994) *Report on ERS-1 SAR interferometric techniques and applications*. Agency, E.S.

Raventós, J. and Marcos, F. (2017) 'The use of InSAR data to monitor slope stability of dams and water reservoirs', *The Annual Meeting of International Commission on Large Dams*. Prague, Czech Republic, July 3–7, 2017. Paris - France: International Commission on Large Dams. Available at: https://site.tre-altamira.com/wp-content/uploads/2017_ICOLD-_InSAR-data_slope-stability_dams-water-reservoirs.pdf (Accessed: 27-09-2018).

Reigber, A. (2001) *Synthetic Aperture Radar: Basic Concepts and Image Formation*. Available at: http://epsilon.nought.de/ (Accessed: 25/05/2018).

Remy, D., Bonvalot, S., Briole, P. and Murakami, M. (2003) 'Accurate measurements of tropospheric effects in volcanic areas from SAR interferometry data: application to Sakurajima volcano (Japan)', *Earth and Planetary Science Letters*, 213(3-4), pp. 299-310.

Richards, J.A. (2009) *Remote Sensing with Imaging Radar*. Springer.

Richards, M.A. (2007) 'A beginner's guide to interferometric SAR concepts and signal processing', *Aerospace and Electronic Systems Magazine*, 22(9), pp. 5-29.

Rocca, F., Prati, C. and Ferretti, A. (1997) 'An overview of ERS-SAR interferometry', *3rd ERS Symposium 'Space at the Service of our Environment*. Florence, Italy, 14-21 March 1997. European Space Agency.

Rodriguez, E. and Martin, J. (1992) 'Theory and design of interferometric synthetic aperture radars', *IEE Proceedings F - Radar and Signal Processing*, 139(2), pp. 147-159.

Rogers, J.D. (1995) 'A Man, A Dam and A Disaster: Mulholland and the St. Francis Dam', *Southern California Quarterly*, 77(1/2), pp. 1-109.

Rosen, P.A., Hensley, S., Zebker, H.A., Webb, F.H. and Fielding, E.J. (1996) 'Surface deformation and coherence measurements of Kilauea Volcano, Hawaii, from SIR-C radar interferometry', *Journal of Geophysical Research*, 101, pp. 23,109-23,125.

Rossi, C. and Gernhardt, S. (2013) 'Urban DEM generation, analysis and enhancements using TanDEM-X', *ISPRS Journal of Photogrammetry and Remote Sensing*, 85, pp. 120-131.

Sadeghi, S. and Yassaghi, A. (2016) 'Spatial evolution of Zagros collision zone in Kurdistan, NW Iran: constraints on Arabia-Eurasia oblique convergence', *Solid Earth*, 7(2), pp. 659-672.

Salfity, M.F., Ruiz, P.D., Huntley, J.M., Graves, M.J., Cusack, R. and Beauregard, D.A. (2006) 'Branch cut surface placement for unwrapping of undersampled three-dimensional phase data: application to magnetic resonance imaging arterial flow mapping', *Applied Optics*, 45(12), p. 2711.

Salih, N.B. (2013) *Stability of dams constructed on problematic substrates*. Ph.D (unpubl.) thesis. Brunel University.

Sandwell, D.T. and Price, E.J. (1998) 'Phase gradient approach to stacking interferograms', *Journal of Geophysical Research: Solid Earth (1978–2012)*, 103(B12), pp. 30183-30204.

Scheiber, R. and Moreira, A. (2000) 'Coregistration of interferometric SAR images using spectral diversity', *IEEE Transactions on Geoscience and Remote Sensing*, 38(5 I), pp. 2179-2191.

SCS (2017) *Geodetic monitoring of the Mosul dam*. Precise levelling. State comission of Survey(Iraq). Unpublished work.

Seco, e.P. and Pedro, S. (2010) 'Understanding seismic embankment dam behavior through case histories', *International Conferences on Recent Advances in Geotechnical Earthquake Engineering and Soil Dynamics*. Missouri University of Science and Technology, May 28-29th. Missouri University of Science and Technology: Scholars' Mine.

Serff, N., SEED, H.B., MAKDISI, F.I. and CHANG, c.-Y. (1976) *Earthquake-induced deformations of earth dams* (EERC 76-4) (EERC 76-4). California: College of engineering; University of Claifornia National Technical Information Service, U.S.D.o.C.

Shamout, M.N. and Lahn, G. (2015) *The Euphrates in Crisis Channels of Cooperation for a Threatened River*. UK, London: Chatham House, the Royal Institute of International Affairs. [Online]. Available at: https://www.chathamhouse.org/publication/euphrates-crisis-channels-cooperation-threatened-river.

Singleton, A., Li, Z., Hoey, T. and Muller, J.P. (2014) 'Evaluating sub-pixel offset techniques as an alternative to D-InSAR for monitoring episodic landslide movements in vegetated terrain', *Remote Sensing of Environment*, 147, pp. 133-144.

Sissakian, V.K., Al-Ansari, N. and Knutsson, S. (2014) 'Karstification effect on the stability of mosul dam and its assessment, north Iraq', *Engineering*, 06(02), pp. 84-92.

Small, D. (1998) *Generation of digital elevation models through spaceborne SAR interferometry*. Zurich, Switzerland Generation of digital elevation models through spaceborne SAR interferometry.

Sousa, J.J., Hlaváčová, I., Bakoň, M., Lazecký, M., Patrício, G., Guimarães, P., Ruiz, A.M., Bastos, L., Sousa, A. and Bento, R. (2014) 'Potential of multi-temporal InSAR techniques for bridges and dams monitoring', *Procedia Technology*, 16, pp. 834-841.

Sowers, G.F. (1965) 'Compressibility of broken rock and the settlement of rockfills', *Proceedings of the 6th International Conference on Soil Mechanics and Foundation Engineering*. Montreal, Canada, 1965. Montreal, Canada, pp. 561-565. Available at: https://ci.nii.ac.jp/naid/10003099822/en/.

Sowter, A. (2003) 'Phase ambiguity determination for the positioning of interferometric SAR data', *Photogrammetric Record*, 18(104), pp. 308-324.

Spaans, K. and Hooper, A. (2016) 'InSAR processing for volcano monitoring and other near-real time applications', *Journal of Geophysical Research: Solid Earth*, 121(4), pp. 2947-2960.

Stansfield, G. (2001) *An Analysis And Assessment Of The Development And Operation Of The Political System*. UNIVERSITY OF DURHAM [Online]. Available at: http://etheses.dur.ac.uk/1205/.

Strozzi, T., Wegmuller, U., Werner, C. and Wiesmann, A. (2000) 'Measurement of slow uniform surface displacement with mm/year accuracy', *IGARSS 2000. IEEE 2000 International Geoscience and Remote Sensing Symposium. Taking the Pulse of the Planet: The Role of Remote Sensing in Managing the Environment. Proceedings (Cat. No.00CH37120)*. Honolulu, HI, USA, 24-28 July 2000. IEEE, pp. 2239-2241. Available at: http://ieeexplore.ieee.org/ielx5/6913/18620/00858368.pdf?tp=&arnumber=858368&isnumber=18620.

Tarchi, D., Rudolf, H., Luzi, G., Chiarantini, L., Coppo, P. and Sieber, A. (1999) 'SAR interferometry for structural changes detection: a demonstration test on a dam', *International Geoscience and Remote Sensing Symposium*. Hamburg, Germany, 28 June-2 July 1999. Hamburg, Germany: IEEE, pp. 1522-1524. Available at: https://ieeexplore.ieee.org/document/772006 (Accessed: 27-09-2018).

Taşçi, L. (2008) 'Dam deformation measurements with GPS', *Geodesy and Cartography*, 34(4), pp. 116-121.

Thanoon, H.A. (1990) 'Geomorphology and instability of slops along the eastern bank of regulating lake at Mosul dam', *Conf. of Mosul Dam Research Centre*. 18-20th of March 1990. Mosul University: Mosul-Iraq.

Tofiq, F.A. and Guven, A. (2014) 'Prediction of design flood discharge by statistical downscaling and general circulation models', *Journal of Hydrology*, 517, pp. 1145-1153.

Tofiq, F.A. and Guven, A. (2015) 'Potential changes in inflow design flood under future climate projections for Darbandikhan Dam', *Journal of Hydrology*, 528, pp. 45-51.

Tomás, R. (2018) Possible deformation scenarios in earthfill dams (personal comunication).

Tomás, R., Cano, M., García-Barba, J., Vicente, F., Herrera, G., Lopez-Sanchez, J.M. and Mallorquí, J. (2013) 'Monitoring an earthfill dam using differential SAR interferometry: La Pedrera dam, Alicante, Spain', *Engineering Geology*, 157, pp. 21-32.

Tomás, R., Li, Z., Liu, P., Singleton, A., Hoey, T. and Cheng, X. (2014) 'Spatiotemporal characteristics of the Huangtupo landslide in the Three Gorges region (China) constrained by radar interferometry', *Geophysical Journal International*, 197(1), pp. 213-232.

Trevi (2018) *Trevi signs the contract for the maintenance works of mosul dam*. Available at: http://www.trevispa.com/en/MosulDam/trevi-signs-the-contract-for-the-maintenance-works-of-mosul-dam (Accessed: January 2018).

U.S. Department of the Interior (2012) 'Embankment Design', in *Design Standards No. 13: Embankment Dams*. 10 edn. U.S. Department of the Interior Bureau of Reclamation, p. 53.

US Army Corps of Engineers (2002) *Engineering and Design Structural Deformation Surveying* (1110-2-1009). Washington, DC: Department of the army US Army Corps of Engineers [Online]. Available at: https://www.publications.usace.army.mil/portals/76/publications/engineermanuals/em_1110-2-1009.pdf.

Usai, S. (2000) 'An analysis of the interferometric characteristics of anthropogenic features', *IEEE Transactions on Geoscience and Remote Sensing*, 38(3), pp. 1491-1497.

Usai, S. and Klees, R. (1999) 'SAR interferometry on a very long time scale: a study of the interferometric characteristics of man-made features', *IEEE Transactions on Geoscience and Remote Sensing*, 37(4), pp. 2118 - 2123.

USGS (2017) *Interactive map*. [Online] Available at: https://earthquake.usgs.gov/earthquakes/eventpage/us2000bmcg#map (Accessed: 04/05/2018).
Utili, S. and Abd, A.H. (2016) 'On the stability of fissured slopes subject to seismic action', *International Journal for Numerical and Analytical Methods in Geomechanics*, 40(5), pp. 785-806.
Voege, M., Frauenfelder, R. and Larsen, Y. (2012) 'Displacement monitoring at Svartevatn dam with interferometric SAR', pp. 3895-3898.
Vöge, M., Larsen, Y. and Frauenfelder, R. (2011) *Monitoring dams and reservoir slopes with interferometric SAR*.
Wakeley, L.D., Kelley, J.R., Talbot, C.A., Pearson, M.L. and Broadfoot, S.W. (2007) *Geologic conceptual model of Mosul Dam* (TR-07-6). St. Louis, Missouri, USA: Center, U.S.A.E.R.a.D.
Wang, T., Perissin, D., Rocca, F. and Liao, M.-S. (2011) 'Three Gorges Dam stability monitoring with time-series InSAR image analysis', *Science China Earth Sciences*, 54(5), pp. 720-732.
Wang, Z., Li, Z. and Mills, J. (2018) 'A new approach to selecting coherent pixels for ground-based SAR deformation monitoring', *ISPRS Journal of Photogrammetry and Remote Sensing*, 144, pp. 412-422.
Wang, Z. and Perissin, D. (2012) 'Cosmo SkyMed AO projects - 3D reconstruction and stability monitoring of the Three Gorges Dam', *2012 IEEE International Geoscience and Remote Sensing Symposium*. Munich, Germany, 22-27 July 2012. IEEE, pp. 3831-3834. Available at: http://ieeexplore.ieee.org/document/6350577/?reload=true.
Wegmüller, U., Santoro, M., Werner, C., Strozzi, T., Wiesmann, A. and Lengert, W. (2009) 'DEM generation using ERS–ENVISAT interferometry', *Journal of Applied Geophysics*, 69(1), pp. 51-58.
Wegmüller, U. and Werner, C. (1997) 'Gamma SAR processor and interferometry software', *Proceeding of the 3rd ERS Scientific Symposium, .* Florence, Italy, 17-20 March 1997. European Space Agency. Available at: https://earth.esa.int/workshops/ers97/papers/wegmuller2/.
Wegmüller, U. and Werner, C. (2011) 'Gamma SAR processor and interferometry software', *Proceedings of the 3rd ERS symposium European space agency*. Florence, Italy, 1997. ESA.
Wegmüller, U., Werner, C., Strozzi, T., Wiesmann, A., Frey, O. and Santoro, M. (2015) 'Sentinel-1 support in the GAMMA software', *European Space Agency (Special Publication)*, SP-731.
Wiley, C. (1965) 'Pulsed Doppler Radar Methods and Apparatus'. Google Patents. Available at: https://www.google.com/patents/US3196436.
Williams, S., Bock, Y. and Fang, P. (1998) 'Integrated satellite interferometry: Tropospheric noise, GPS estimates and implications for interferometric synthetic aperture radar products', *Journal of Geophysical Research: Solid Earth (1978–2012)*, 103(B11), pp. 27051-27067.
Wright, T., Parsons, B. and Fielding, E. (2001) 'Measurement of interseismic strain accumulation across the North Anatolian Fault by satellite radar interferometry', *Geophysical Research Letters*, 28(10), pp. 2117-2120.
Wright, T.J., Parsons, B., England, P.C. and Fielding, E.J. (2004a) 'InSAR observations of low slip rates on the major faults of western Tibet', *Science*, 305(5681), pp. 236-239.
Wright, T.J., Parsons, B.E. and Lu, Z. (2004b) 'Toward mapping surface deformation in three dimensions using InSAR', *Geophysical Research Letters: Solid Earth*, 31(1).
Wu, H., Zhang, Y., Zhang, J. and Chen, X. (2010) 'Mapping deformation of man-made linear features using DInSAR technique', *ISPRS TC VII Symposium*. Vienna, Austria, July 5–7, 2010,. International Society for Photogrammetry and Remote Sensing, pp. 293-297.

Available at: https://www.scopus.com/inward/record.uri?eid=2-s2.0-84923876618&partnerID=40&md5=f99a1ca5cb2298c13318dd67ea92e34f (Accessed: 01-10-2018).

Yu, C., Li, Z. and Penna, N.T. (2018a) 'Interferometric synthetic aperture radar atmospheric correction using a GPS-based iterative tropospheric decomposition model', *Remote Sensing of Environment*, 204, pp. 109-121.

Yu, C., Li, Z., Penna, N.T. and Crippa, P. (2018b) 'Generic atmospheric correction online service for InSAR (GACOS)' *EGU General Assembly 2018*. 2018. Veinna, Austria. Available at: https://meetingorganizer.copernicus.org/EGU2018/EGU2018-14158.pdf.

Yu, C., Penna, N.T. and Li, Z. (2017) 'Generation of real-time mode high-resolution water vapor fields from GPS observations', *Journal of Geophysical Research: Atmospheres*, 122(3), pp. 2008-2025.

Zebker, H.A. and Lu, Y. (1998) 'Phase unwrapping algorithms for radar interferometry: residue-cut, least-squares, and synthesis algorithms', *Journal of the Optical Society of America A*, 15(3), pp. 586-598.

Zebker, H.A., Rosen, P.A. and Hensley, S. (1997) 'Atmospheric effects in interferometric synthetic aperture radar surface deformation and topographic maps', *Journal of Geophysical Research: Solid Earth*, 102(B4), pp. 7547-7563.

Zebker, H.A. and Villasenor, J. (1992) 'Decorrelation in interferometric radar echoes', *IEEE Transactions on Geoscience and Remote Sensing*, 30(5), pp. 950-959.

Zebker, H.A., Villasenor, J. and Madsen, S.N. (1992) 'Topographic mapping from ERS-1 and Seasat radar interferometry', *International Geoscience and Remote Sensing Symposium (IGARSS)*. Houston, TX, USA, 26-29 May 1992. IEEE, pp. 387-388. Available at: http://ieeexplore.ieee.org/ielx2/1014/12510/00576718.pdf?tp=&arnumber=576718&isnumber=12510.

Zhou, W., Li, S., Zhou, Z. and Chang, X. (2016) 'Remote sensing of deformation of a high concrete-faced rockfill dam using InSAR: a study of the Shuibuya Dam, China', *Remote Sensing*, 8(3), p. 255.

Zisk, S. (1972) 'A new, earth-based radar technique for the measurement of lunar topography', *Earth, Moon, and Planets*, 4(3), pp. 296-306.